Design and Optimisation of Passive Silicon Photonic Device for Wideband Communication System

Xiao Zhe

School of Electrical and Electronic Engineering

A thesis submitted to the Nanyang Technological University
in partial fulfillment of the requirement for the degree of
Doctor of Philosophy

2015

ACKNOWLEDGEMENTS

This thesis would not have been possible without the help of many generous people. I first wish to acknowledge my supervisor Professor Luan Feng of Nanyang Technological University and my supervisor Dr. Jason Liow Tsung-Yang of the Institute of Microelectronics, A*STAR for their invaluable encouragement and guidance. Each discussion with them always inspires me with good ideas during the journey of my Ph.D. study. I am also very grateful to Professor Shum Ping for his kind help and support for my research and experimental works at Network Technology Research Centre. The advices offered by Dr. Luo Xianshu and Dr. Lim Penghuei when I was working with them on the integrated filter project were of great values. I wish to thank Dr. Gu Bobo and Dr. Samson T. H. Silalahi who have worked with me on measurements. And I also appreciate the help from Dr. Zhang Jing, Dr. Wu Kan, Dr. Wong Jia Haur, Dr. Huy Quoc Lam, Yu Xiaojun and Liu Huanhuan. Discussion with each one of them was always inspiring. I would like to greatly appreciate Zhou Yanyan for her help to improve my research papers and this thesis. I would like to especially thank my bachelor supervisor Professor Huang Ming. His research initiated my interest in the research field of communication technologies and guided me to start the journey of research studies. Finally, I am grateful to the current and previous staff and student members of Network Technology Research Centre, OPTIMUS - Photonics Centre of Excellence and CNRS International NTU THALES Research Alliance.

TABLE OF CONTENTS

LIST OF FIGURES

LIST OF TABLES

ACRONYMS

A

ASE	Amplified Spontaneous Emission
ADC	Analog-to-digital Converter

C

CW	Continuous Wave
CMOS	Complementary Metal-Oxide-Semiconductor

B

BOX	Buried Oxide

D

DC	Direct-Current
DSC	Double Surface Corrugation
DBR	Distributed Bragg reflector
DUV	Deep Ultraviolet
DAC	Digital-to-analog Converter

E

EDFA	Erbium-Doped Fibre Amplifier
EOM	Electro-optic Modulator
EO	Electro-optical
EMI	Electromagnetic Interference

F

FEM	Finite Element Method
FIR	Finite Impulse Response
FDTD	Finite-Difference Time-Domain
FSR	Free Spectral Range
FTTH	Fiber To The Home

G

GD	Group Delay

L

LOCOS	LOCal Oxidation of Silicon

M

MWP	Microwave photonics
MZM	Mach-Zehnder Modulator
MZI	Mach-Zehnder Interferometer
MMI	Multimode Interference
MPF	Microwave Photonic Filter

N

NA	Numerical Aperture

O

OSA	Optical Spectrum Analyzer

P

PC	Polarization Controller
PD	Photodetector
PM	Polarization Maintaining
POI	Polarization Independent
PDL	Polarization Dependent Loss

Q

Q-factor	Quality Factor

R

RF	Radio Frequency
RIE	Reactive Ion Etching

S

SMF	Single-mode Fibre
SOA	Semiconductor Optical Amplifiers
SSA	Singular Spectrum Analyzer
SOI	Silicon on insulator
SSC	Spot Size Converters

T

TE	Transverse Electric
TM	Transverse Magnetic
TWPDA	Traveling-Wave Photodetector Array

V

VNA Vector Network Analyzer

VOA Variable Optical Attenuator

W

WDM Wavelength Division Multiplexing

SUMMARY

Silicon photonics, as one of the emerging technologies increasingly attracts a lot of research interests due to the mature CMOS compatible fabrication process and easy integration with microelectronics, etc. Compared with silicon electronics, light as the signal carrier has the potential advantages of high energy efficiency, large bandwidth, as well as low cross talk and heat elimination. However, unlike silicon electronics which has already allowed inexpensive access to the mature design and fabrication processes, tools and device libraries, silicon photonics is still a young technology and it is also required to build up a low cost and standardized design and fabrication mechanism. At current stage, one of the objectives in the community is to develop a set of practical design rules and reusable methodology for various functional photonic components, and then to integrate these photonic components further onto a miniature chip to achieve system level applications.

This thesis aims at proposing general and simplified design and optimisation methods for several critical passive photonic components including grating couplers, low loss silicon waveguides and delay lines as well as power splitters etc. In the investigation of grating coupler design, we pioneer the studies on bandwidth mechanism of planar waveguide grating couplers on silicon photonics and derive the bandwidth formula of planar waveguide grating couplers for general cases for the first time. Based on the formula, we further propose the guidelines on how to optimize the bandwidth of grating couplers. As for the coupling efficiency optimisation, we simplify the efficiency optimisation process into several separated steps for individual parameters to reduce the design complexity. We also propose novel design methods for grating couplers to achieve specific functionalities. For waveguide and delay line design, the

design procedures using hybrid waveguide schema are discussed for low loss delay line unit with desirable group delay. We design and experimentally demonstrate 50 picoseconds low loss delay line on 300 nm SOI platform. Low propagation loss of ~0.1 dB/cm is achieved on the straight rib waveguide. Taking into account both low loss and desirable delay, a complete design and characterization process for passive delay line is presented. For the studies on splitters, we demonstrate the most compact multimode interference (MMI) splitter up to date, the splitter footprint only takes $1.5 \times 1.8\ \mu m^2$ area, about one order smaller than the previously reported MMI splitters. Meanwhile, the splitter is polarization insensitive and the measured excess losses for TE and TM modes at telecommunication wavelength are as low as 0.11 dB and 0.18 dB, respectively. As compared to Y-junction splitters which will induce periodic fringes in the spectrum while they are linked with multimode waveguides, the proposed MMI splitter has fringe free spectral response in a wideband range. The design principle and optimisation processes to reduce footprint of MMI splitters while still maintaining low loss performance are discussed. The detailed discussions of design and optimisation methods for individual components and corresponding experimental demonstrations are presented in the separate Chapters.

Furthermore, these proposed photonic components are applied to a real project to achieve integrated microwave photonic filters with spectrum re-configurability. In this work, we demonstrate an integrated 16 tap finite impulse response (FIR) filter on silicon photonics platform. The spectral reconfigurablility of the FIR filter is achieved by varying the tap weights through intensity changes using the variable optical attenuators. The core function chip has a size of around 1 cm^2. The entire design schema, integration and measurement process are discussed accordingly. The design

and optimisation methods developed in this thesis could be useful for other projects those require photonics integration on silicon platform.

Chapter 1 INTRODUCTION

1.1 Background and motivation

Silicon photonics has received increasing interest owing to its potential for dense integration of photonic components using mature CMOS fabrication technologies. The most promising applications for silicon photonics are related to optical interconnects in CMOS integrated circuits, computing platform and optical communications, where the objective is to manufacture low-cost information processing components, making it possible to achieve very large scale integration. The potential area stands to impact a number of industries ranging from computing and communication to biomedicine etc.

There are two sets of problems that need to be addressed in order to integrate photonic devices on a highly developed silicon platform. One is design and optimisation of individual photonic components and the other is integration of various components for a specific functional system. In silicon electronics, inexpensive access to mature and standardized fabrication processes, tools and device libraries has already been made available. Design and fabrication of silicon electronic devices has been separated in production. However, no such mechanism exists in silicon photonics. Most groups independently develop their own silicon photonics elements. Such absence has proven to be a major hindrance to silicon photonics development. It is necessary to come up with practical design rules and reusable methodologies for silicon photonics devices.

As it stands, most of the current design methods for silicon photonic device are targeted at individual applications normally involving time-consuming multi-parameter scans. It is not easy to standardize and build a common specification

protocol. Thus, our study aims at proposing easy-to-use simplified design and optimisation methods for several critical passive functional components including grating couplers, low loss silicon waveguides and delay lines as well as power splitters.

For design of grating couplers, we proposed an approach to separate design and optimisation into several steps, and each step only involves one dimension parameter. We also systematically discuss the mechanism of coupling bandwidth of grating couplers. Besides, a novel method is proposed for design of polarization insensitive grating couplers and a separate schema is presented to solve the low coupling efficiency problem for grating couplers on low-contrast refractive index waveguides. For design of waveguides and delay lines, we apply the hybrid design schema to design low loss waveguides and delay lines on 300 nm silicon platform. For design of multimode interference (MMI) splitters, our major contribution is to make splitters with compact footprint. The method to design compact MMI splitters with polarization insensitive and low loss performance is proposed. The detailed discussions on each component are presented in later Chapters following the order of theoretical principle, design rules, the experimental demonstration and measurement analysis. Furthermore, these optimized components are applied to implement an integrated spectrum reconfigurable microwave photonic filter.

1.2 Research Scope

The scope of our research involves two main aspects:

I. The first aspect is to investigate the design and optimisation approaches for critical passive photonic components on silicon photonics platform.

For this part, the main objective is to propose efficient design and optimisation methods for photonic components including grating couplers, silicon waveguide and delay lines, as well as power splitters. Numerical simulation, theoretical analysis and experimental verification are carried out in the study. Here we not only calculate the performance of individual components using the computational software tools such as COMSOL[1], Lumerical[2], [3] but also discuss the operation mechanism from theoretical perspective so that the physical properties of each component can be explored and the design and optimisation approaches can be set up. All the proposed design and optimisation approaches take practical fabrication factors into account. Moreover, we provide a benchmark as comparison with state-of-the-art studies for several optimized components proposed in this dissertation.

II. By applying the optimisation principles and photonic components proposed in work part I, we proceed to integrate these components into a system implementation of spectrum reconfigurable finite impulse response filters.

For this part, we first theoretically investigate the working mechanism of FIR filter and make a feasible design schema on silicon photonics platform by combining the advantages of both fiber and on-chip sub-systems. In order to achieve spectral tunability spectrum, a set of variable optical attenuator (VOAs) is used to adjust the branch weights of the filter while a photodetector array is designed to collect the radio frequency (RF) signals at the end of the system. The whole system design and characterization are discussed and the obtained experiences from this work are summarized.

1.3 Major contributions of the thesis

Major contributions of the thesis are described below.

I. In this thesis, we pioneer the studies on bandwidth mechanism of planar waveguide grating couplers on silicon photonics platform. We are the first to point out that the grating dispersion, which was ignored in previous studies, has substantial effect on the grating bandwidth performance. Based on grating theory, we derive the bandwidth formula of planar waveguide grating couplers for general cases and analyze the effect of individual parameters of input fiber and gratings on coupler's bandwidth behavior. Based on the bandwidth formula, several practical design rules are proposed to increase grating bandwidth. Most of the previous works solely focus on optimizing the coupling efficiency, this work makes it clear on how to optimize the bandwidth of grating couplers.

II. We simplify the process of coupling efficiency optimisation for grating couplers and propose novel coupler designs to achieve specific functionalities. Conventionally, coupling efficiency optimisation of grating couplers involves multiple dimension parameters which can be categorized as the internal parameters (such as the grating height and etch depth) and the external parameters (such as the thickness of cladding layers). This results in a multi-parameter optimisation problem, which is usually considered as impractically time-consuming. In our work, we simplify the optimisation process of grating couplers by separating the optimisation in a sequence of independent steps. In addition, novel grating coupler design approaches are proposed such as using double surface corrugation gratings to control coupling modes and using a

separate grating design approach to increase the coupling efficiency of fiber to low refractive index (such as silicon nitride) waveguide excitation.

III. We design and demonstrate up to date the most compact MMI splitter with low loss performance on 300 nm silicon platform. The splitter footprint only takes area of $1.5\times1.8\ \mu m^2$, about ten times smaller than the previously reported MMI splitters. Meanwhile, the splitter is polarization insensitive and the measured excess losses for TE and TM modes at 1.55 μm telecommunication wavelength are as low as 0.11 dB and 0.18 dB, respectively (In terms of loss performance, only one work reports better performance [4], where the excess loss is about 0.06 dB for TE polarization, but the device footprint is much larger than ours demonstration and the splitter only works for TE polarization). We also present the design and optimisation principles to achieve compact low loss MMI splitters.

IV. The general design procedures for low loss delay line units using hybrid waveguide schema are proposed. For this work, we design and experimentally demonstrate 50 picoseconds low loss delay line on 300 nm SOI platforms. The delay line unit consists of straight rib waveguide and strip bend section linked by a transition taper waveguide. Low propagation loss of ~0.1 dB/cm is achieved on the straight rib waveguide. Taking into account of both low loss and desirable delay, a complete design and characterization process for passive delay lines is presented.

V. We experimentally demonstrate a frequency domain method for optical group delay measurement. Using the method, only common instruments i.e. regular speed modulator, photodetector (PDs) and spectrum analyzer are required,

which simplifies the measurement setup and release the rigorous instrument requirements. Although we are not the first to propose the method, we have greatly promoted the method to general cases from theoretical aspects and provided the formula and approaches for accuracy analysis.

VI. We design and implement an integrated 16 tap FIR filter on silicon photonics platform. A feasible design schema is proposed to achieve high order FIR filter on silicon photonics. In current research community, most of the research efforts still focus on single component design and optimisation while system integration for functional devices are usually conducted by large semiconductor companies like Intel and IBM etc. [5], [6]. In this work, we attempt to make a system integration of several photonic and RF components to achieve high order FIR filter on silicon photonics platform. The design schema and system integration is presented, and the experience obtained can provide a useful reference for similar processes.

1.4 Thesis organization

This thesis comprises of seven Chapters with the following organization:

Chapter 1 introduces the background and motivation of silicon photonics based devices design and optimisation as well as their integration for system level filtering applications. The scope of the research is stated, major contributions are described, and the organization of the thesis is outlined.

Chapter 2 reviews the critical passive components studied in this dissertation including couplers, waveguides and splitters, and the discussion is extended to relevant passive devices such as ring resonator and arrayed waveguide gratings etc.

The state-of-the-art design and performance of passive photonic components is summarized.

Chapter 3 reviews the research status on planar waveguide grating couplers, followed by studies on the bandwidth mechanism of grating couplers and simplified efficiency optimisation approach. The general bandwidth formula is derived and several novel design ideas are presented for grating couplers with specific functionalities. Experimental results of single port and multi-port grating couplers are also discussed in the Chapter. We then further summarize our experiences of alignment operations obtained from these experiments.

Chapter 4 describes the design and optimisation of low loss silicon waveguides and delay lines on silicon photonics platform. We also present a frequency domain method to measure the group delay of silicon waveguides. The experimental setup and measurement results are further discussed in the Chapter.

Chapter 5 focuses on ultra-compact low loss power splitter design on silicon photonics. We first describe the observed fringe phenomena in Y-junction splitter when they are linked with multimode waveguides, followed by providing a solution to making fringe free spectrum using the MMI splitter. Then, rules to determine the minimum width of multimode core waveguide to keep low loss performance are given for design of MMI splitters and we demonstrate the most compact MMI splitter up to date. The splitter is polarization insensitive and the excess losses for both TE and TM modes are below 0.2 dB.

In Chapter 6, we integrate the components designed in Chapter 3, 4 and 5 with a set of VOAs and photodetectors to realize a spectrum reconfigurable microwave FIR filter. A feasible design schema is proposed with considering the advantages of both the

fiber and on-chip sub-systems. The whole design processes, testing system and measurement results are discussed.

Finally, the thesis ends with the conclusion and plan for future work in Chapter 7.

Chapter 2 LITERATURE REVIEW

This Chapter reviews several topics on silicon photonics passive components that are relevant to the research presented in the later Chapters. The review focuses on the critical passive components studied in this dissertation including couplers, waveguides and splitters, and the discussion is extended to other popular passive devices such as ring resonator and arrayed waveguide gratings etc. The state-of-the-art design and performance of passive photonic components is summarized.

2.1 Silicon Photonic devices and applications

Silicon electronics based applications have once revolutionized the way the world operates and people's life in many aspects. However, with the increasing requirement of computing ability and bandwidth, the inherent limitations of large scale integrated metallic circuit such as heat rise and power dissipation become the bottleneck for further improvements. Silicon photonics provides a potential approach to overcome these limitations by carrying information with photon instead of electron, which is physically free of heat issue and electromagnetic interference and also allows for broad bandwidth. Under these motivations, owing to excellent material properties of silicon and mature complementary metal–oxide semiconductor (CMOS) compatible fabrication technologies, silicon photonics has attracted increasing attention and research interest. As illustrated in Figure 2.1, the potential area stands to impact a number of industries ranging from computing and telecommunication to biomedicine and brings value to people. However, several challenges also exist. One of the main challenges is material integration since it is not possible to solely reply on silicon material to realize all the functional devices needed for large scale photonics

integration. For instance, silicon is not a direct bandgap semiconductor material, and thus it needs to bring new materials into the silicon platform system such as III–V materials which can be used to create on-chip light sources etc. Moreover, not like silicon electronics, nowadays most research groups continue to design, build and test chips internally rather than sharing a common CMOS foundry infrastructure with a mature and standardized photonic device library[7]. Most of the industry has been focused on developing individual silicon photonics elements and components. Few companies have developed integrated product solutions. In addition, silicon photonics has not been able to achieve high enough volumes of production so far in industry due to high development cost.

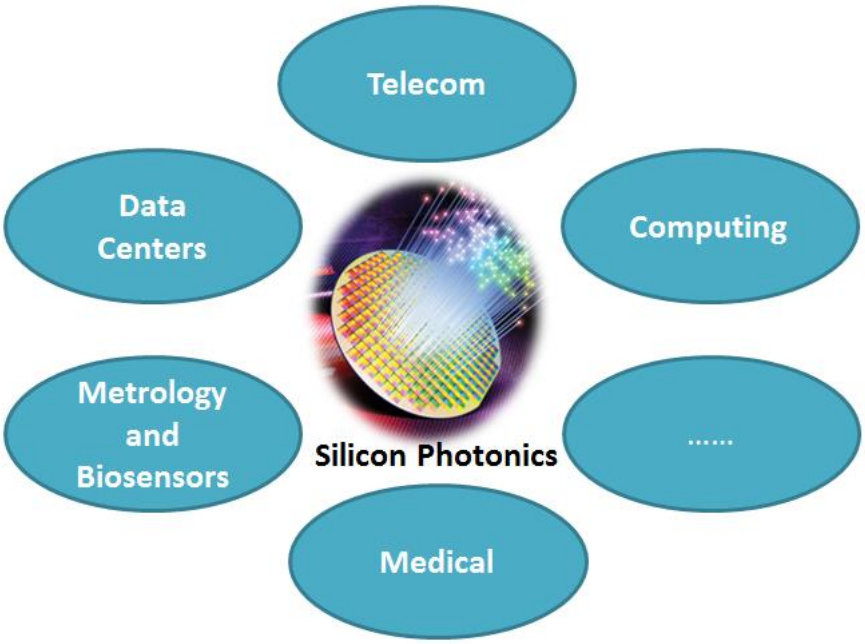

Figure 2.1 Uses of silicon photonics for a number of industries

The objective of silicon photonics is to achieve similar mechanism already existing in silicon electronics, allowing separated design and fabrication procedures and re-using the standardized design to manufacture low-cost information processing components. The “pluggable” schema of silicon photonics devices shown in Figure 2.2 is an ideal

solution for very large scale integration in silicon photonics. The community works on finding suitable technologies or similar alternatives to achieve the purpose.

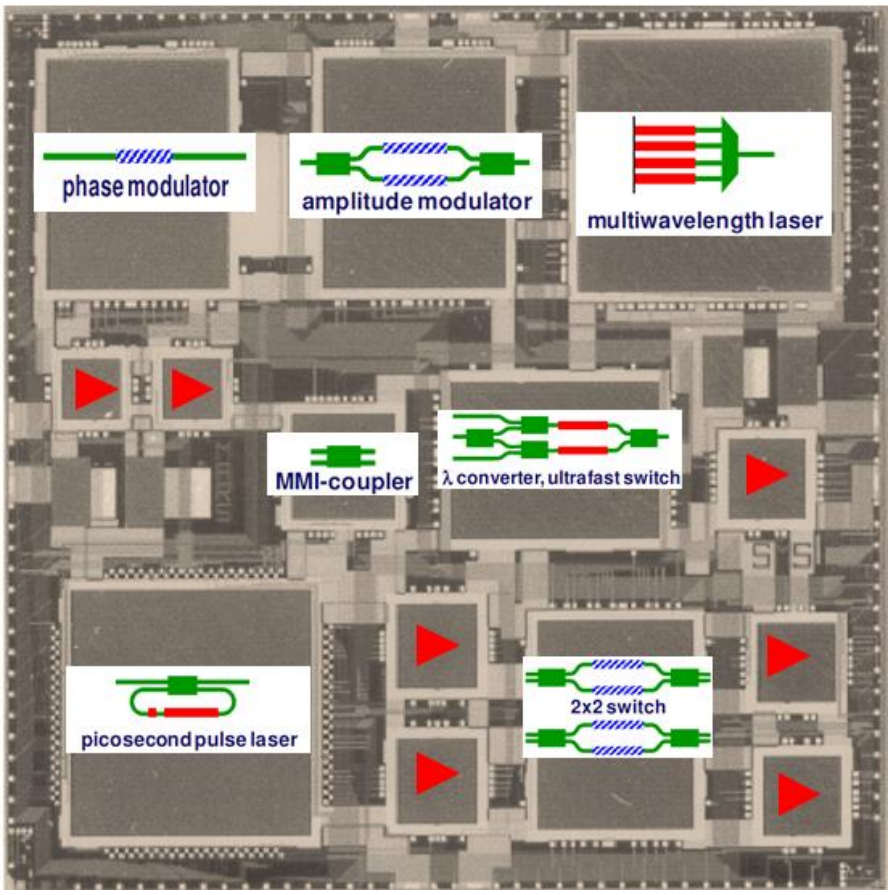

Figure 2.2 Integration of multiple functional silicon photonics devices

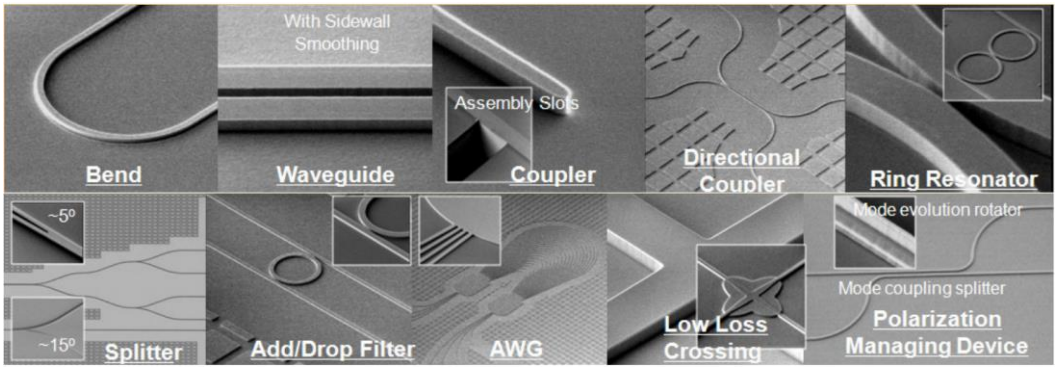

Figure 2.3 IME passive devices library

Silicon photonics devices can be generally classified to passive and active devices. Passive devices are a set of critical components which operate without source of energy. Numerous passive photonic devices arouse research interest in the community for several years; they are waveguides, directional couplers, multi-mode interference couplers, ring resonators, gratings and so on. Figure 2.3 illustrates the passive devices library established in Institute of Microelectronics, Agency for Science, Technology and Research (IME, A*STAR). Active devices require external source of energy for their operation and support specific electronics-photonics functions. The critical active components include silicon-based lasers, modulators and detectors and so on. In later sections of this Chapter, the review focuses on the critical passive components that are relevant to the research presented in the thesis.

2.2 Couplers

In an optical communication system, fiber as the major signal transmission medium bridges the network devices such as switch, router and signal amplifier with network terminals. Silicon photonics based devices are usually deployed at the intermediate nodes of the network in order to achieve necessary networking and processing functions. In order to process light signals on silicon chip, the coupling of optical signals between fiber system and waveguides on chip is the first step to launch on-chip signal processing.

As illustrated in Figure 2.4, the major problem for signal coupling between fiber and waveguide on chip is that the dimensions of fibers are much larger than that of silicon waveguides. The core diameter of single mode fibers is between 8 and 10.5 μm, but dimensions of silicon waveguides are around several hundreds of nanometers. If

directly coupling light from fiber to waveguide without proper interface design, the dimensional mismatch will lead to serious mode mismatch and power loss.

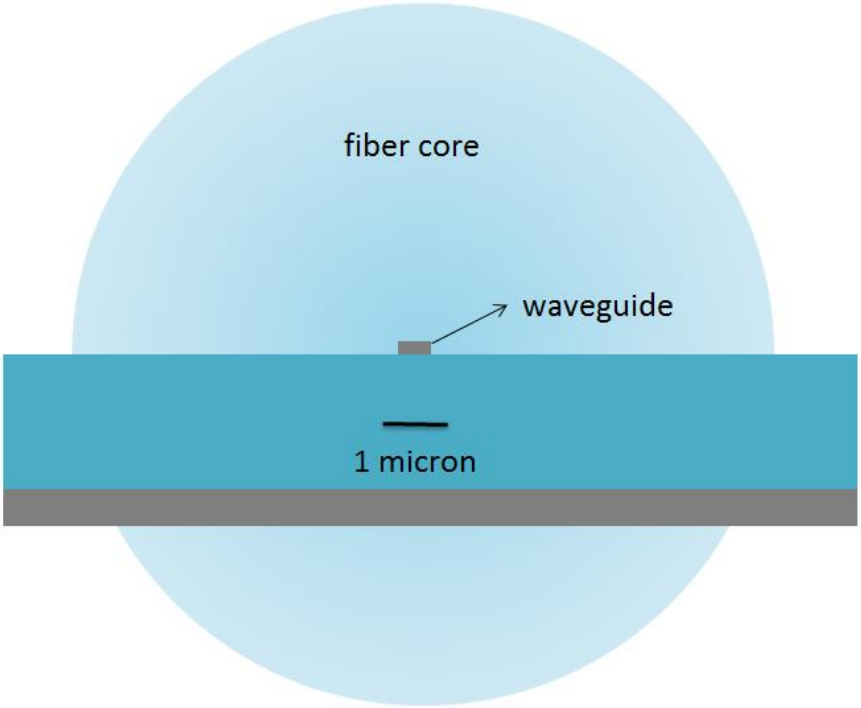

Figure 2.4 Comparison of dimension of fiber and waveguide

Various methods, such as using a prism [8], [9], taper coupling[10], [11] or with a grating[12], [13] have been proposed to achieve the coupling between fiber and silicon waveguide. Prism coupler is separated from silicon waveguide and requires a holder to keep the coupling condition constant. Using tapers or gratings as interfaces are the most popular approaches to achieve coupling between fiber and waveguide.

Wedge-shaped taper and inverse/inverted taper are adopted to achieve fiber-to-chip mode excitation horizontally. In these methods, the fiber and waveguide are located in the same plane and we call them “horizontal coupling”. The wedge-shaped taper and inverse/inverted taper structures are illustrated in Figure 2.5 (a) and (b). For wedge-shaped taper, the fiber mode first couples into a wide “widget” and evolves adiabatically into a standard rib mode through the “wedge” taper and finally

propagates within the waveguide. Based on published report, coupling losses of less than 0.5 dB per facet have been demonstrated with wedge shaped taper couplers [14]. By adopting the similar idea, a structure with a relatively large silicon block on top of a sub-micrometer dimensional silicon rib waveguide is used to achieve fiber to chip coupling[15].

Compared with wedge shaped tapers, inverse/inverted tapers are easier to be fabricated. Inverse taper is simply fabricated at the end of silicon waveguide, which has the same height with the waveguide and therefore is not required for extra etch processes. The inverse tapers can gradually extend the guided mode to match the dimension of fiber. The coupling losses of most inverse couplers are typically less than 1 dB with 3 dB bandwidth of hundreds of nanometers [10], [16]–[19].

The other popular method shown in Figure 2.5(c) is to fabricate a diffraction grating area, which normally has much the same dimension as the fiber, at the entrance of silicon waveguide to achieve optical excitation from vertical direction. Diffraction grating couplers provide a practical and effective means of light coupling between fiber and chip. Unlike the taper couplers, grating couplers are more practical by eliminating the need of signal excitation from the edge of the chip to provide flexibility. Besides, they are easier to package in a monolithic system and capable of multi-port applications[20]. The coupling loss of grating couplers for fiber-to-chip excitation are around -1.6 to -6 dB [21]–[25]. The drawbacks of grating couplers are their limited bandwidth performance. Compared with the taper couplers which allows for a 3 dB bandwidth of hundreds of nanometers, most grating couplers have a 3 dB bandwidth of tens of nanometers.

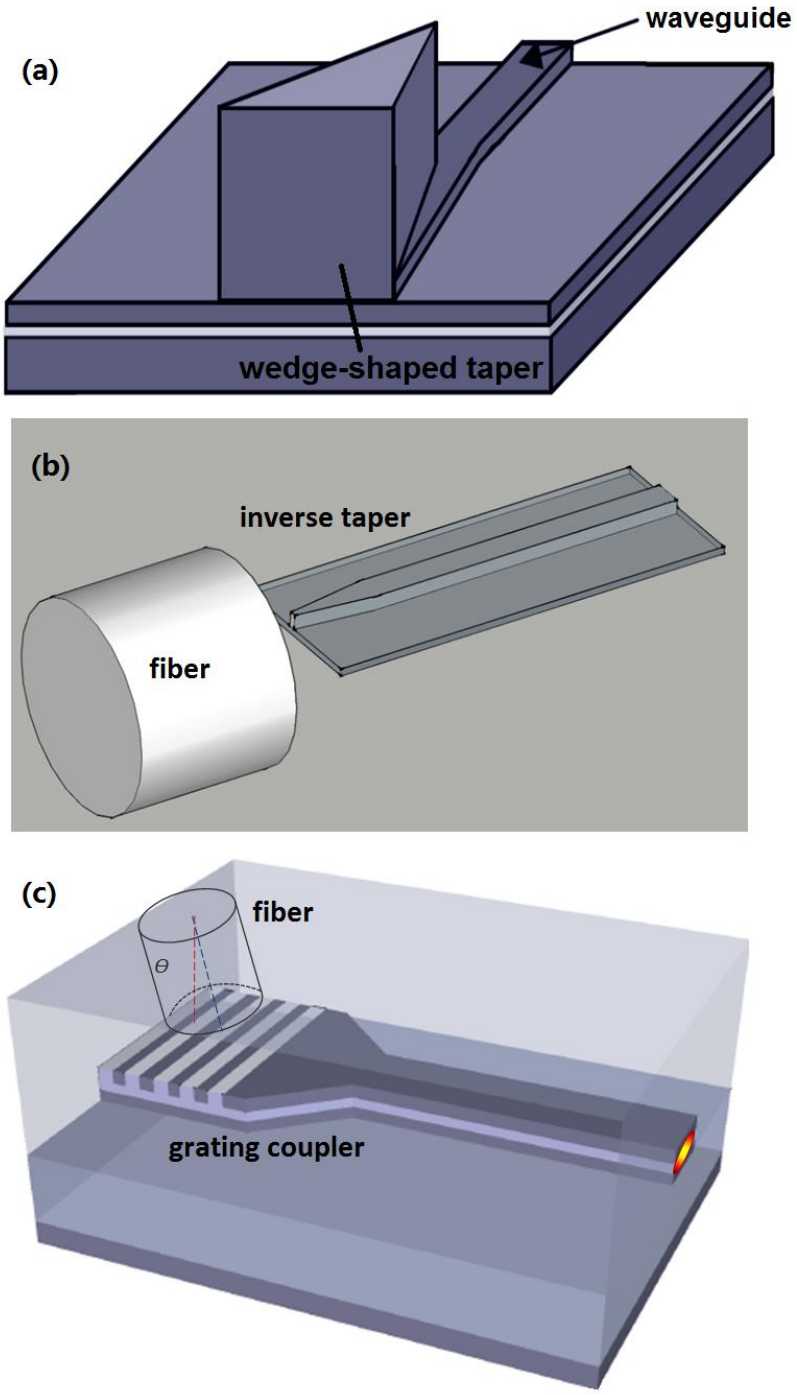

Figure 2.5 (a) Wedge shaped taper; (b) Inverse/Inverted taper; (c) Diffraction grating coupler

2.3 Waveguides

After the optical signal is coupled from fiber to chip through the grating interface, the optical signal starts its journey in the silicon waveguide. It is commonly recognized

that silicon waveguides induce much larger propagation loss than optical fibers. The optimisation of loss performance of silicon waveguide is one of the most important considerations. In practical cases, the etched sidewall roughness of waveguides is a significant source of propagation loss. Optimized waveguide structure with good optical mode confinement can relieve the issue to some degree. Besides, compactness is another consideration in design of silicon waveguides.

In Figure 2.6, two types of widely-used waveguides – strip and rib/ridge waveguides are illustrated. Strip waveguides have a rectangular cross section layer confined between claddings. Rib waveguides consist of the slab with a strip superimposed onto it. Till now, using standard fabrication processes, the propagation loss of silicon strip waveguides is around 2–3 dB/cm [26]. Shallow-ridge waveguides can achieve ~ 0.1 – 0.3 dB/cm propagation loss [27], [28] and the loss is determined by waveguide width and etch depth. Using etch-free fabrication processes such as the local oxidation of silicon (LOCOS), waveguide sidewall profile can be smoothed, and in this case, sub-dB propagation loss is achievable [29], [30]. Recently, H. Lee *et al*. demonstrated on-chip 27 meter ultra-low loss delay lines based on special waveguides of wedge geometry cross-section with smooth edges using optimized fabrication [31], which reveals the potential for ultra-long delay on integrated photonic platform.

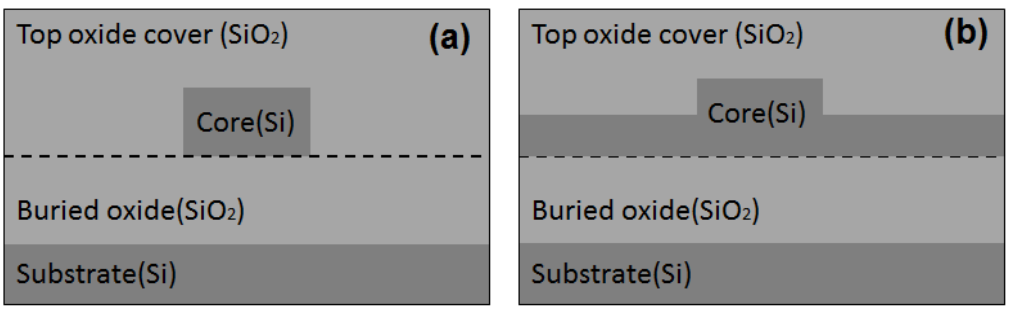

Figure 2.6 (a) Strip waveguide; (b) Rib/ridge waveguide

Another set of newly developed waveguides are slot waveguides, which are demonstrated for highly enhanced optical confinement in low refractive index slot, providing a new potential solution of the integrated optical systems [32], [33]. The configurations of slot waveguides are categorized into vertical and horizontal slot waveguides (shown in Figure 2.7) according to slot orientations. A slot-waveguide consists of two strips of high-refractive-index materials separated by a sub-wavelength-scale low-refractive-index slot region. Because of the field discontinuity at the high index contrast interfaces, the optical field are strongly enhanced in the low index region nears the interfaces. The model field profiles of quasi-TE in a vertical slot waveguide and quasi-TM mode in a horizontal slot waveguide are illustrated in Figure 2.8. It can be seen that light is strongly confined in narrow slot regions. Note that waveguide configuration is not limited to single slot, multiple slots can be configured in design if necessary.

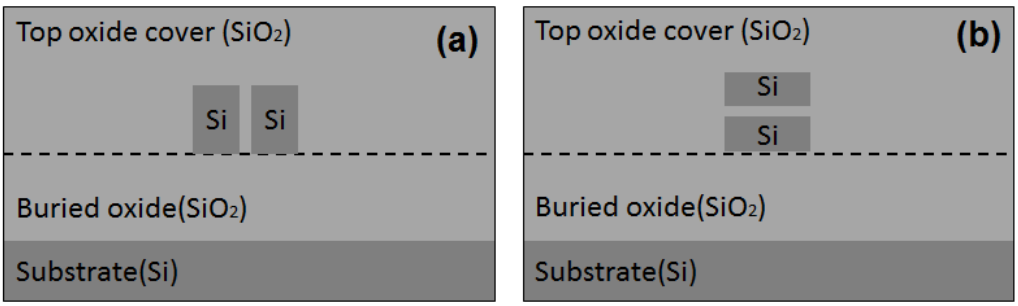

Figure 2.7 (a) Vertical slot waveguide; (b) Horizontal slot waveguide

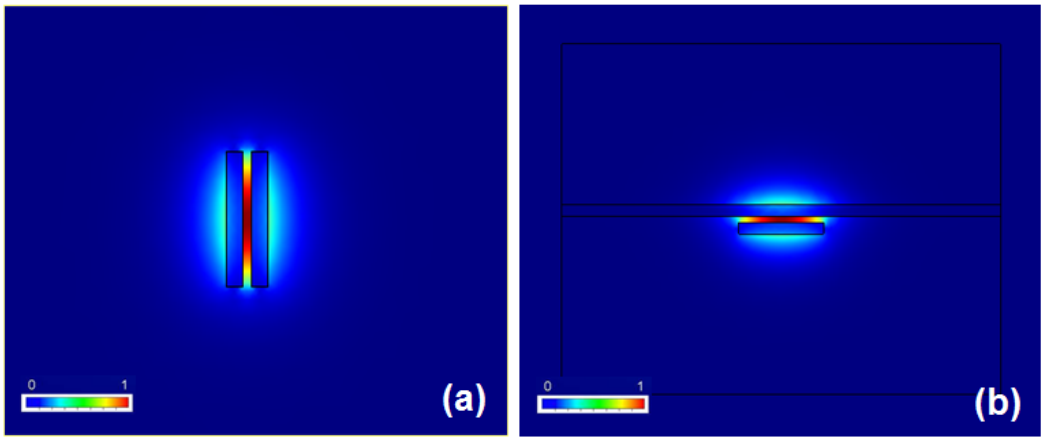

Figure 2.8 (a) Quasi-TE mode field in a vertical slot waveguide; (b) Quasi-TM mode field in an asymmetric horizontal slot waveguide

In practical cases, compared with the vertical slot structure which is challenging to be fabricated and has high loss due to strong field falling on etch caused side wall roughness, the horizontal slot structure is a better configuration for material integration and fabrication. Based on the reported experimental results, the propagation loss for the quasi-TE mode in a vertical slot waveguide with a single slot of 50 nm or less is greater than 11.6 ± 3.6 dB/cm [34]; the propagation loss is around 6.3 ± 0.2 dB/cm and 7.0 ± 0.2 dB/cm for horizontal single and multiple slot waveguides, and the loss is mainly due to absorption of a-Si waveguide material [35]. The tight optical confinement property inside the slot area allows for highly efficient interaction between fields and materials, which enables wide range of applications such as all-optical switching [36], signal modulator [37], and optical detection and sensor [38]–[40] on integrated photonics platform. Some of these applications are illustrated in Figure 2.9.

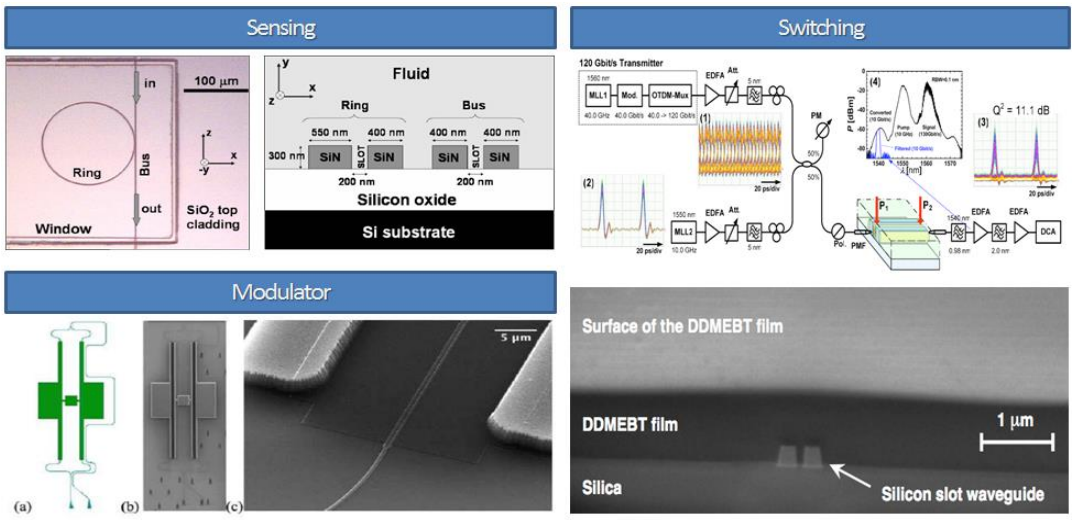

Figure 2.9 Slot waveguides based applications[36]–[38]

2.4 Splitters

In practical cases, optical signals seldom only travel in single channel. Routing signals to separate channels is essential in most functional devices on silicon photonics platform. Power splitters play a critical role in many applications such as Mach-Zehnder Interferometer (MZI), wavelength division multiplexing (WDM) and optical switch systems etc. Figure 2.10 shows several typical structures to achieve power splitting. They are Y-junctions, directional couplers, and multimode interference (MMI) waveguides. The microscope pictures of an arc-shape Y-junctions and a MMI splitter are illustrated in Figure 2.11. Excess loss, uniformity and compactness are major specifications required for optimisation in splitter design. The power uniformity can be indicated by the ratio of the maximum and minimum output powers, and the excess loss is the total loss except the 3dB power splitting loss induced by the splitter. Compactness is critical consideration in design for scaling high-density integration.

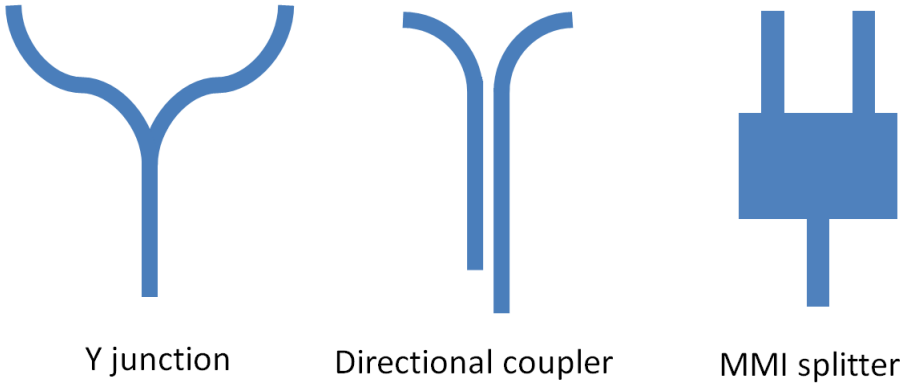

Figure 2.10 Typical structures which enable power splitting

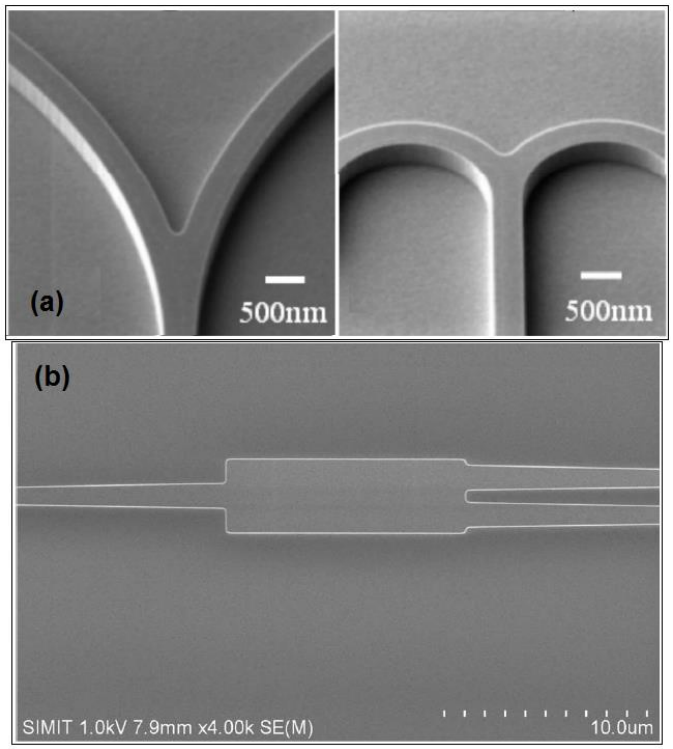

Figure 2.11 (a) Arc-shape Y-junction splitters [41] (b) MMI splitter with taper for input and output waveguides[4]

Y-junction consists of a straight waveguide linked with two branches through a tiny taper. It normally has compact footprint and polarization insensitive splitting performance. Typical loss for a conventional Y-junction splitter with small splitting angle is 1 dB [42]. Fabrication of a conventional Y-junction needs very high lithographic resolution, and it is not possible to fabricate a perfect branch tip due to

the limited processing resolution. Besides, photo-resists or etch residues could be left in the tiny gap between two branches during the fabrication processes [41]. To optimize the splitting angle of Y-junction with arc-shaped branches, excess loss of 0.15 dB per facet is achievable [41].

Compared with Y-junction splitters, multimode interference (MMI) splitters have better fabrication tolerance and sub-dB loss performance. The working mechanism of MMI splitters is based on self-imaging principle, that is, an input field will be periodically reproduced in a single or multiple images insides the multimodal core. When output waveguides are aligned with these images, the input power can split into multiple output waveguides. One of drawbacks of conventional MMI splitters is that they normally have large device footprint [43], [44], and they are also polarization sensitive. It is reported that 0.06 dB excess loss is achievable by the MMI splitter with optimized tapers linked with input and output waveguides for TE polarization light [4].

Directional couplers are normally applied to design polarization splitters [45]–[51]. The working principle is to enable cross-polarization coupling through breaking the horizontal and vertical symmetries of two parallel waveguides of directional couplers. Conversion efficiency, extinction ratio and fabrication error tolerance are important considerations in splitters structure design. Based on previous works, ~ 0.02 to 1 dB conversion efficiencies are demonstrated and up to ~20 dB extinction ratio is achievable [45]–[51].

2.5 Other passive components

Ring resonator is one of critical passive components which can be utilized to create other functional devices such as optical buffers [52], modulators [53]–[56], filters [57],

[58], and sensors[59], [60] etc. Resonant structures are based on a directional coupler with one arm routed back to the input acts as a feedback loop. When a waveguide is properly positioned next to a ring resonator, it can achieve "critically coupled", i.e. perfect equilibrium between power coupled into the ring and power lost. There are lots of configurations of ring based resonators. They are all-pass resonators and add-drop ring resonators[61], nested ring resonators[62] and cascaded ring resonators [63] and so on. The quality factor (Q-factor) which measures the resonance sharpness and free spectral range (FSR) which is defined as the spacing between neighbor resonances are significant specifications of resonant structures. Q-factor is normally determined by loss performance and system spectral response function. FSR depends on the ring circumstance and resonator length. High Q-factor and relatively large FSR are common requirements for most of applications [61].

Arrayed waveguide grating routers (AWG) are another set of useful passive devices. They are normally used as multiplexers/demultiplexers. AWG consists of an array of waveguides with linearly increasing length and two couplers. Due to the phase relationship, interference and diffraction occur within the structure and an optical signal of multiple wavelengths will be distributed to an array of output waveguides according to wavelength. On silicon photonics platform, AWG can be fabricated with an array of strip or rib waveguides and two star couplers. Based on published studies, 16 and 32 channel spacing of 200 GHz with around 20 dB crosstalk are reported based on trip or rib waveguides[64], [65].

Chapter 3 GRATING COUPLER DESIGN AND OPTIMISATION

3.1 Introduction

Fibers to chip interconnection devices are critical components in the use of silicon photonics devices. The large dimensional mismatch between optical single mode fiber and high index contrast waveguide challenges the signal excitation between one and the other. In this Chapter, we focus on the design and optimisation of grating couplers on a silicon photonics platform. The objective is to make the design process simple and efficient. Since the optimisation for grating coupling efficiency is intensively studied in previous research works, our research angle is put on the optimisation of grating bandwidth, which though seldom discussed before, has aroused increasing demands in broadband optical communication system. In one section of this Chapter, we give a systematic discussion on bandwidth mechanism of grating couplers and investigate the important parameters of both fiber and gratings that have influence on bandwidth performance, and based on the discussion, the design and optimisation rules are summarized. In addition, we propose a general simplified process to design high efficiency wide band grating couplers. Meanwhile, a novel method is proposed for design of polarization insensitive grating couplers and a separate grating design schema is presented to solve the low coupling efficiency problem for grating couplers on low-contrast refractive index waveguides.

In a later section of the Chapter, we discuss the experimental works using single port and multi-port grating couplers to achieve fiber-to-chip excitation. For the multi-port coupling experiment, we use four grating couplers to excite 16 channels of silicon

waveguides. The work is also the preparation for the integrated filter project presented in Chapter 6. The measurement results are discussed and our practical experience to operate fiber and grating alignment is summarized.

3.2 Literature review on grating couplers

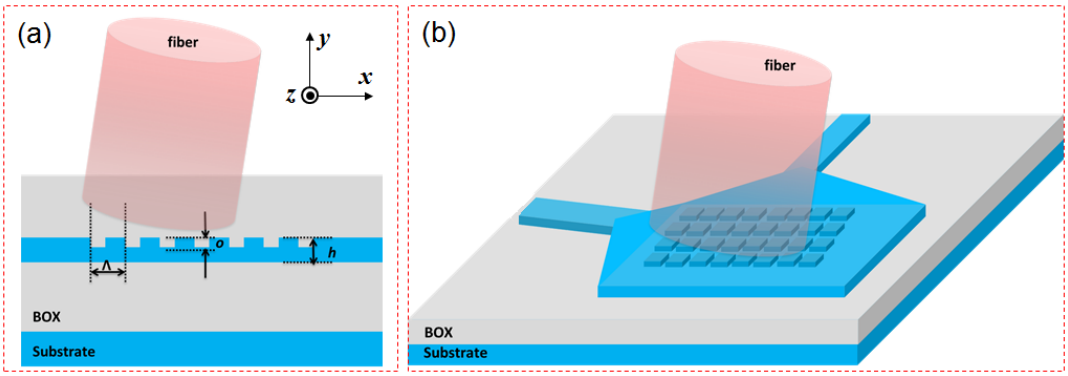

Figure 3.1 (a) One dimensional grating coupler; (b) Two dimensional grating couplers

Diffraction grating couplers are one of effective interfaces to achieve light coupling between fiber and chip. Unlike the taper couplers stated in Chapter 2, grating couplers are more practical and flexible by eliminating the need of signal excitation from the edge of the chip. Besides, they are easier to package in a monolithic system and capable of multi-port applications[20]. Grating couplers are generally classified as one dimensional (1-D) and two dimensional (2-D) structures. The configuration of one dimensional grating couplers is shown in Figure 3.1(a). For 1-D grating couplers, grating grooves are uniform in transversal direction (z direction). The critical dimension parameters include grating period/pitch, etch depth and grating thickness etc. The filling factor is defined as the ratio of the length of unperturbed area (without etching) to the period. The configuration of two dimensional grating couplers is illustrated in Figure 3.1(b) (Although two outputs are shown here, it is not a necessary

condition in 2-D grating couplers definition). Unlike 1-D grating couplers, 2-D grating couplers have refractive index modulation in both lateral and transmission directions. Thus, the design and optimisation of 2-D grating couplers is more complicated. However, whatever for 1-D or 2-D configurations, the working principle of grating couplers is the same, i.e., to enable the phase velocities match between the guided mode and one order of diffracted lights inside grating region to achieve mode excitation.

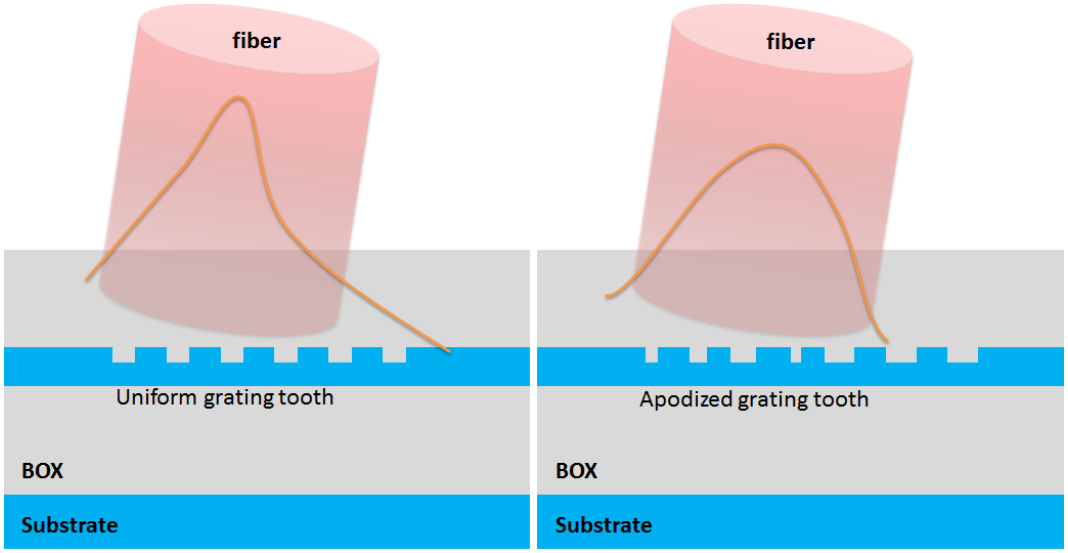

Figure 3.2 Outgoing beam profile of (a) Uniform grating coupler and (b) Apodized grating coupler

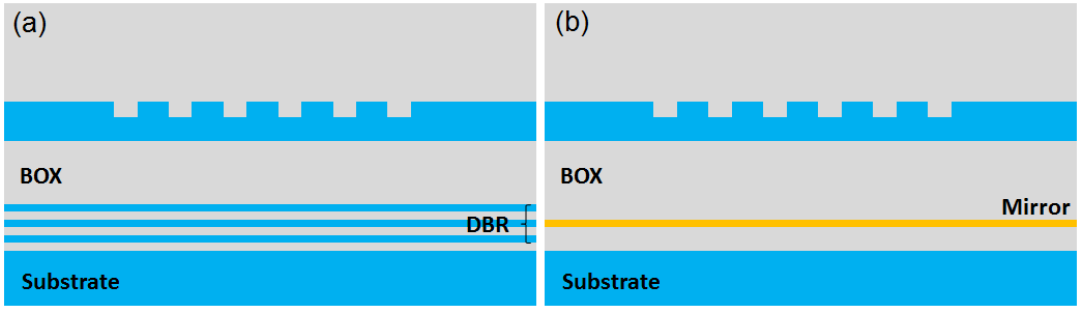

Figure 3.3 (a) Distributed Bragg reflector; (b) Reflection mirror

Efficiency and bandwidth are two critical specifications of planar waveguide grating couplers. Many techniques have been reported to increase the coupling efficiency. These approaches can be generally categorized into two sets. The first set of approaches is to modify the grating structure itself to enhance the coupling efficiency. This kind of methods include using apodized grating strength to tailor the leakage factor of the grating to the mode profile of the fiber [66]–[69] and using poly-silicon overlay [70] to decrease the upward and downward power leak to the surround cladding layers, etc. The outgoing beam profiles of normal uniform grating and apodized grating couplers are illustrated in Figure 3.2. If using a uniform gratin coupler, the coupling efficiency is reduced because that the outgoing beam profile from the grating coupler differs from the Gaussian shape of fiber beam[71]. Thus, apodized gratings are proposed to match the outgoing beam profile with the mode profile of fiber. The other set of approaches is to control the power flow around the grating coupler interface by adding external layers such as bottom reflection mirror or reflection gratings [72], [73] in the buried oxide (BOX) layer to enhance the coupling efficiency. The external layers are configured to direct the power back into the grating structure for constructive effect. The illustrations of these methods are shown in Figure 3.3. The drawback of this type of methods is that much extra fabrication complexity is introduced because to fabricate the reflection structures at the backside of the chip is not easy in practical.

In the research community, compared with intense researches on optimisation of coupling efficiency, only a few attempts have been reported to increase the coupling bandwidth[74]–[76]. Compared with taper couplers, the drawback of grating couplers is their limited bandwidth performance. The typical 1 dB bandwidth of silicon grating couplers is around few tens of nanometers. Large bandwidth can bring better

fabrication and operation tolerance and it is also required for wide bandwidth applications such as high speed optical communication. C. R. Doerr *et al*. first made an approximate calculation of the bandwidth of grating couplers by relating the efficiency drop in the coupling spectrum to the wavelength-dependent diffraction angles [74]. This approach overestimates the coupling bandwidth, as the grating dispersion effects have been neglected. At the same time, we also investigate the bandwidth mechanism of planar waveguide grating couplers. We attributed the coupling bandwidth to the mismatch of effective indices between the diffracted beam and the actual grating structure around the resonant wavelength, and proved that the grating dispersion should not be ignored in bandwidth calculation. A simple bandwidth formula is derived based on the explanation [77]. Then, X. Chen *et al.* gave a discussion based on the explanation of C. R. Doerr *et al.* with the grating dispersion effects being considered [75]. However, these aforementioned studies are only based on simple estimations rather than rigorous derivation. Especially, the 1 dB bandwidth coefficient introduced as a constant in these bandwidth approximations has no proper physical explanation, which is too simple that important details are ignored. Thus, we further work on deriving the bandwidth formula for planar waveguide grating couplers based on the rigorous grating theory [78]. It is found that the 1 dB coefficient is not a constant value but a function of both fiber parameters such as beam width, position and the grating parameters such as the field decay rate of the grating coupler etc. We investigate in detail the effect of each of these parameters on the bandwidth behavior. A complete analysis is presented based on the rigorous bandwidth formula, which offers new insights on grating bandwidth and also provides practical guidelines for grating design and fiber operation for wideband fiber to chip excitation. The detailed works will be discussed in later sections of this Chapter. Until the time of writing this thesis, several design or experimental works have been

reported to support our proposed theoretical principles such as using low effective index gratings, small dispersion structures or small core fiber to increase the coupling bandwidth [75], [79]–[81].

In addition, some novel grating structures and design methods have also been proposed to achieve specific functionalities like multichannel coupling or duplexer [82], polarization splitter [83] and polarization insensitivity [84]–[87] etc. Some of these works are using refractive index engineering based grating structures, which are also attracting research interests and are used to enhance the grating coupling behaviors. Transformation optics approach has been also employed to design integrated silicon photonics coupler for fiber to waveguide excitation[88]. As for the polarization insensitive grating coupler design, most of design methods are actually to realize two grating interfaces (or combined as one interface) using two-dimensional structures for mode excitation. In our study, a one-dimensional method using double surface corrugation gratings is proposed to control the coupling modes and achieve polarization insensitive excitation [89]. We theoretically investigate the property of the structure and describe the excitation condition with formulas. Besides, we propose a separate design schema to solve the low coupling efficiency problem for grating couplers on low-contrast refractive index waveguides (silicon nitride waveguides). All the details of our works will be discussed in later sections.

3.3 Bandwidth mechanism of grating couplers

In this section, a systematic discussion on bandwidth mechanism of grating couplers is presented. Large bandwidth is required for broad bandwidth applications such as high speed optical communication and signal processing. It can also bring better fabrication and operation tolerance. For this part, we first give a simple derivation of

the bandwidth formula for grating couplers based on coherence theory and then make a rigorous derivation based on grating theory. At the end of the discussion, a series of bandwidth optimisation rules are summarized for design of grating couplers on silicon photonics platform.

3.3.1 A simple derivation of bandwidth formula based on coherence explanation

Before starting the rigorous bandwidth formula derivation for grating couplers, we first give an intuitive and simple derivation based on the coherence relation between guided mode in the grating region and diffraction mode induced by the input optical field. The simple configuration of grating couplers is illustrated in Figure 3.4, the major dimension parameters need to be determined during the design include the grating period Λ, the waveguide height *h*, the etch depth *o*, and the ratio of perturbed to non-perturbed grating region (filling factor). The values of these dimensions and the indices of the cladding and waveguide materials directly determine the effective index of the grating region and affect the diffraction of the incident light.

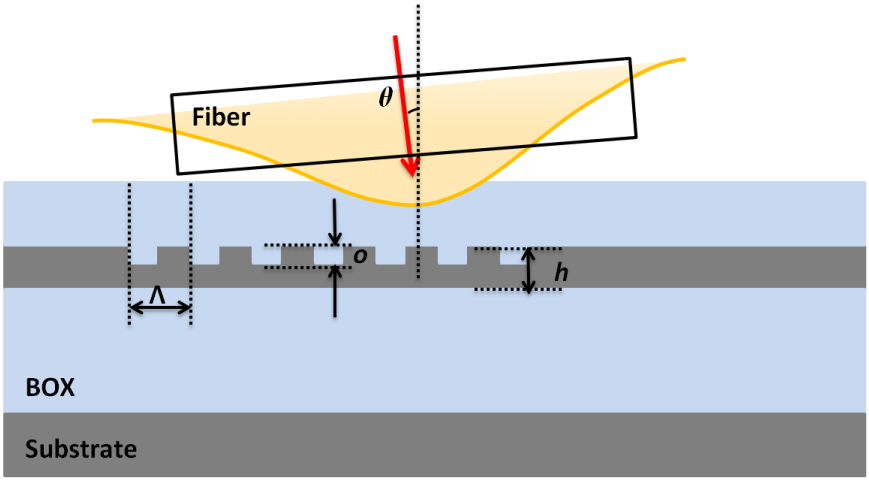

Figure 3.4 Grating coupler configuration schema

For fiber-to-chip coupling, the whole process consists of several sub-processes as follows: first, the input optical power is diffracted by gratings and forms several order of diffraction modes; then, if the tangential component of wavevector of one order (usually the -1 order is used for fiber-to-chip coupling) of the diffraction modes has the same value with the guided mode wavevector in the grating region, the diffraction mode will excite the grating guided mode; along the grating tangential direction, the diffracted light is superposed with the excited guided mode in the grating region and the coupling effect is continuously increased until the end butt of the grating region is reached. In this process, only at certain resonant wavelength λ_0, the excited guided mode is always in phase with the diffraction mode and the coupling effect is strengthened. But for the waveguide deviating from wavelength λ_0, these two modes are off phase and the coupling is weakened. Based on this explanation, we can attribute the coupling bandwidth to the mismatch of effective indices (or wavevectors) between the diffracted beam and the actual grating structure around the operation wavelength for fiber to waveguide excitation. Thus, it is easy to derive the bandwidth formula as follows:

Eq. (3.1) is the diffraction equation [69] of grating coupler,

$$-\frac{n_0}{\lambda}\sin\theta + \frac{n_d}{\lambda} = \frac{1}{\Lambda} \tag{3.1}$$

where n_0 is the refractive index of the top cladding of the grating, n_d is defined as $|\boldsymbol{\beta}_{d//}|\lambda/2\pi$, $\boldsymbol{\beta}_{d//}$ is the tangential component of wave vector of the diffracted light (diffraction order is set to be -1) along the grating surface, λ is the free-space wavelength, Λ is the grating period and θ is incidence angle of the light. The actual effective index of a grating coupler, noted as $n_w(\lambda)$, represents the dispersion

characteristic of the grating coupler. It can be calculated using the method given in previous works [90]. At the resonant wavelength λ_0, the effective index of the diffracted light matches with the actual grating effective index, i.e. $n_w(\lambda_0) = n_d(\lambda_0)$. For a given grating structure with fixed pitch (Λ) determined by the resonant wavelength λ_0, the effective index of the diffracted light as a function of wavelength can be written as:

$$n_d(\lambda) = \frac{[n_w(\lambda_o) - n_o \sin\theta] \cdot \lambda}{\lambda_o} + n_o \sin\theta \tag{3.2}$$

where, $n_d(\lambda)$ has a mismatch with the actual effective index $n_w(\lambda)$ except the resonant wavelength, which is noted as $D_n(\lambda)$. Then we have:

$$D_n(\lambda) = \frac{[n_w(\lambda_0) - n_0 \sin\theta] \cdot \lambda}{\lambda_0} + n_0 \sin\theta - n_w(\lambda) \tag{3.3}$$

Obviously, at the resonant wavelength, $D_n(\lambda_0)$ is equal to zero. Using the Taylor series expansion of Eq.(3.3) at the resonant wavelength and keeping the first order term of $\Delta\lambda$, we obtain:

$$\Delta\lambda = \frac{\Delta D_n \Big|_{\lambda = \lambda_0}}{\frac{n_w(\lambda_0) - n_0 \sin\theta}{\lambda_0} - \frac{dn_w(\lambda)}{d\lambda}\Big|_{\lambda = \lambda_0}} \tag{3.4}$$

Eq.(3.4) relates the shift in wavelength from λ_0 to the increases of effective index mismatch (ΔD_n) which is responsible for the coupling efficiency drop. We introduce a 1 dB mismatch coefficient $C_{1\text{dB}}$ that induces 1 dB of coupling efficiency drop, i.e.:

$$\Delta\lambda_{1dB} = C_{1dB}\left|\lambda = \lambda_0\right| \left| \frac{1}{\frac{n_w(\lambda_o) - n_o \sin\theta}{\lambda_o} - \frac{dn_w(\lambda)}{d\lambda}\Big|\lambda = \lambda_o} \right| \qquad (3.5)$$

Eq.(3.5) can be used to calculate the intrinsic 1-dB bandwidth of a given grating structure without detailed numerical simulations. According to Eq. (3.1) and (3.2), the first term in the denominator in Eq.(3.5) is equal to $1/\Lambda$ which also equals to the slope $dn_d(\lambda)/d\lambda$. It is clear that the denominator in Eq.(3.5) is the slope difference of $n_d(\lambda)$ and $n_w(\lambda)$ around resonant wavelength, which represents the mismatch between the effective indices of diffraction light and grating structure. $C_{1\mathrm{dB}}$ is a wavelength dependent coefficient. By studying various grating couplers with different structures and materials, we find $C_{1\mathrm{dB}}$ is about 0.10 and 0.05 for operating wavelength at 1.55 μm and 1.31 μm, respectively. The results are verified by X. Chen *et al*[74], [75]. Eq.(3.5) is the basic form of bandwidth formula of grating couplers, but in this formula, a general coefficient $C_{1\mathrm{dB}}$ is used without exact physical explanation. Actually, the empirical value of the coefficient is obtained at specific coupling conditions that the fiber is located at the best coupling position [12] and the input fiber has normal numerical aperture etc. In next section, we will derive the bandwidth formula based on rigorous grating theory, and the concrete form of the coefficient will be clear.

3.3.2 Derivation of rigorous bandwidth formula for fiber-to-chip excitation

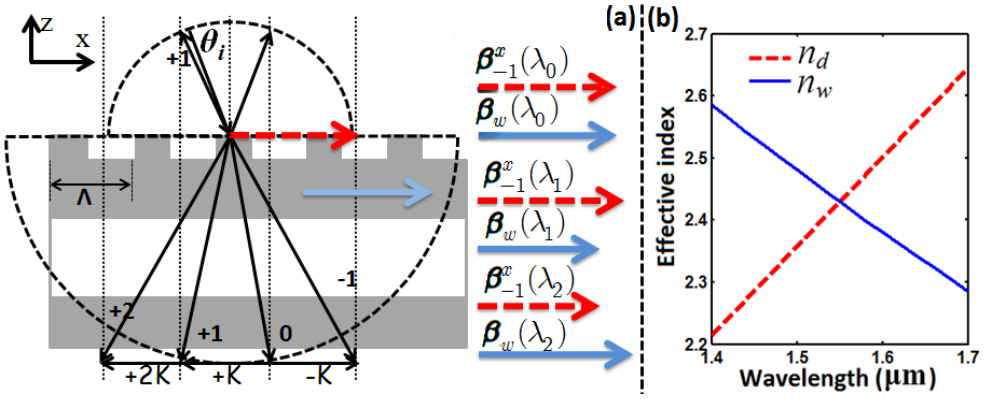

Figure 3.5 (a) Grating coupler model for fiber to waveguide excitation and wave vector diagram (Wave expansion with wave vector from vector Floquet Condition); (b) Dispersion diagram

In this section, we will derive the rigorous bandwidth formula of planar waveguide grating couplers. The theoretical model of a planar waveguide grating coupler is shown in Figure 3.5 (a). Here the rigorous wave expansion from vector Floquet condition is adopted for wavevector illustration. There are other completely equivalent rigorous wave expansions given in [69], these expansions have different wavevector magnitudes in z axis but their tangential component are completely the same along the grating surface. While optical beam is incident into grating coupler from the fiber at tilt angle θ_i, the interaction of the grating in redirecting the incident light is simply dividing the incident light into many diffracted inhomogeneous plane waves that have directions given by $\boldsymbol{\beta}_q = \boldsymbol{\beta}_u - q\boldsymbol{K}$, where q=0, ±1, ±2, ..., q is the diffracted order number, $\boldsymbol{\beta}_u$ is the wavevector of the undiffracted beam (i.e. q = 0), and $\boldsymbol{\beta}_q$ is the wavevector of the q diffracted order. $\boldsymbol{K}$ is grating vector, which is defined as $\boldsymbol{K}=2\pi/\Lambda$. This condition is known as Floquet condition [69], which indicates the satisfaction of boundary conditions for tangential electric field along the periodic grating surface. Each order of the diffracted lights is determined by the incident field

(the undiffracted item $\boldsymbol{\beta}_u$) and the grating structure ($q\boldsymbol{K}$ item). In Figure 3.5, the -1 order diffracted light is illustrated for fiber to waveguide coupling as it is used in most practical grating couplers (-1 order is also considered in the following discussion). When coupling occurs, it is required that the tangential phase velocity of -1 order diffracted wave is able to be the same with that of the guided mode in the grating region for the guided mode excitation [91]. Consider the case without grating structure, a fundamental problem is encountered that the phase velocity of the refractive light is always smaller than the guided mode of the waveguide along the propagation direction, causing that the guided mode cannot be excited. The grating therefore serves as enabling to match the phase velocity with the guided mode by -1 order diffracted light in the grating region. According to the coupling theory, the strongest coupling occurs while the diffracted light has the same tangential wavevector with the guided mode of the grating coupler. However, since the wavevectors of the diffracted light and guided mode are functions of wavelength with different slopes, so only one intersection exists in the dispersion diagram (here $\lambda - n_{eff}$ diagram is utilized). By taking silicon grating coupler as an example, Figure 3.5 (b) illustrates the typical dispersion diagram for grating couplers, where n_w is the effective index of guided mode in the grating region and n_d is index of diffracted light. A more intuitive illustration is given in Figure 3.5 (a), the wave vectors of the diffracted light and the guided mode are well-matched at resonant wavelength λ_0 for the strongest coupling, but at other wavelength that deviating from the resonant wavelength (like $\lambda_1 > \lambda_0$ or $\lambda_2 < \lambda_0$ in Figure 3.5 (a)), a mismatch is introduced between both wavevectors causes the drop in coupling efficiency. Based on the Floquet condition, the wavevector mismatch can be written as:

$$\Delta\boldsymbol{\beta} = \boldsymbol{\beta}_w - \boldsymbol{\beta}_{-1}^x = \frac{2\pi}{\lambda} n_w - \left(\frac{2\pi}{\lambda} n_0 \sin\theta_i + \frac{2\pi}{\Lambda}\right) \tag{3.6}$$

where n_0 is the refractive index of top cladding, $\boldsymbol{\beta}_w$ is the wave vector of the guided mode, $\boldsymbol{\beta}^x_{-1}$ is the tangential wave vector of the -1 order diffracted light, n_w is the effective index of the grating region, θ_i is the incident angle and Λ is the grating pitch. Using the Taylor series expansion of Eq.(3.6) at the resonant wavelength λ_0 with the condition of $\Delta\boldsymbol{\beta}(\lambda_0)= 0$ and keeping the first order term of $\Delta\lambda$ (here, we write in form of absolute value), we obtain:

$$\Delta\boldsymbol{\beta} = \pm\frac{2\pi}{\lambda_0}|\Delta\lambda| \cdot \left|\frac{1}{\Lambda} - \frac{dn_w(\lambda)}{d\lambda}\Big|_{\lambda=\lambda_0}\right| \qquad (3.7)$$

In Eq.(3.7), the positive sign is for the wavelength range of $\lambda < \lambda_0$, the negative sign is for $\lambda > \lambda_0$. Now we investigate the effect of such a mismatch on the coupling bandwidth based on rigorous grating theory [78].

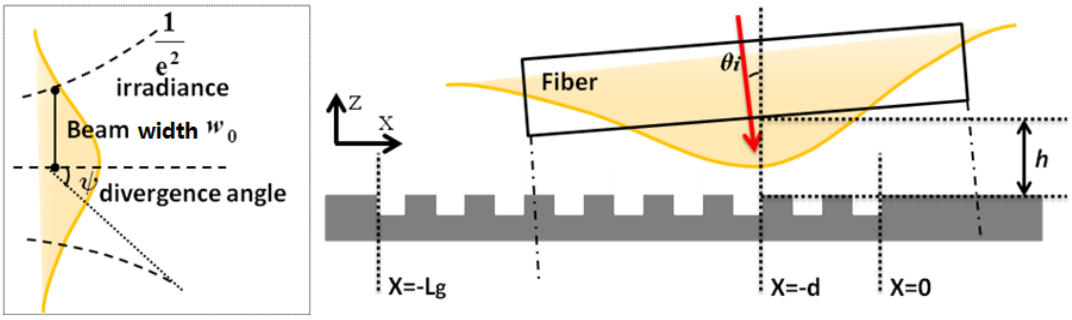

Figure 3.6 Fiber Gaussian beam model and schematic grating coupler structure in coordination system

Figure 3.6 schematically illustrates a typical fiber-to-chip grating coupler interface in the coordinates. The coordinate origin (x = 0) is located at the first pitch of the gratings. The amplitude distribution of the fiber beam can be modeled by a Gaussian profile shown in Figure 3.6. Provided that the x-axis position of the beam center is at $-d$, in the defined coordinate, the complex amplitude of incident Gaussian beam can be expressed as:

$$s_0(x) = E_0 \exp[\frac{-(x+\mathrm{d})^2}{w_0^2}] \exp[-ikz - ik\frac{(x+\mathrm{d})^2}{2R(z)} + i\varsigma(z)] \tag{3.8}$$

Where, E_0 is the peak amplitude of incident Gaussian beam on the grating plane, w_0 is the beam width, k is the wave number, $R(z)$ is the radius of curvature of the beam's wavefront and can be expressed as Eq.(3.9), $\varsigma(z)$ is the Gouy phase shift expressed as Eq.(3.10).

$$R(z) = z[1 + (\frac{z_R}{z})^2], z_R = \frac{\pi w_0^2}{\lambda} \tag{3.9}$$

$$\varsigma(z) = \arctan(\frac{z}{z_R}) \tag{3.10}$$

In Eq.(3.8), $\exp[-ikz - ik\frac{(x+\mathrm{d})^2}{2R(z)} + i\varsigma(z)]$ is the phase item of incident Gaussian beam. We find that the phase item can be ignored to simplify the bandwidth formula derivation. This is because that the coupling efficiency can be expressed as a definite integral of a function over grating coordinates in *x*-axis (The coupling efficiency expression is given in Eq.(3.16), and details are discussed later in this section). Inside the exponent function, only the item $-ik\frac{(x+\mathrm{d})^2}{2R(z)}$ is a function of *x* and the other two items will produce constant value after operating the definite integral. In practical operations, fiber should be put as close as possible to the grating surface, i.e. *h* is a very small value (the configuration are shown in Figure 3.6). In this case, the beam doesn't form curved wavefront within the short propagation distance, i.e. the beam wavefront can be approximated as a plane and then Guassin beam can be viewed as a plane wave in the propagation direction. In this case, $R(z)$ is several orders larger than other parameters in the phase item, so the phase item is ignorable in the derivation. Therefore, the field amplitude of the fiber beam can be simplified as (E_0 indicates the peak amplitude):

$$s_0(x) = E_0 \cdot e^{-(x+d)^2/w_0^2} \tag{3.11}$$

The incident fiber beam propagates along *z* axis with a tilt angle θ_i. Then, the amplitude distribution of the beam impinging on the grating coupler surface can be approximated by:

$$\begin{cases} s(x) = E_0 \cdot e^{-(x+d)^2/w_1^2} \\ w_1 \simeq [w_0 + h\tan(\psi)] \,/\, \cos(\theta_i) \end{cases} \tag{3.12}$$

where *h* is the height between the fiber and grating surface shown in Figure 3.6 (w_0 is much greater than *h*), ψ is the divergence angle of the Gaussian fiber beam, w_1 can be also expressed as:

$$w_1 \simeq [w_0 + h\frac{\mathrm{NA}}{n_0\cos(\psi)}] \,/\, \cos(\theta_i) \tag{3.13}$$

Where, NA is the numerical aperture of fiber, which characterizes the range of angles over which the fiber can accept or emit light. In order to calculate the coupling efficiency, the complex amplitude of the guided wave in the grating region excited by the fiber source (precisely, in the fiber beam effectively covered grating region) is expressed as $A(x) = a(x) \cdot e^{i\beta_w x}$. Thus, the coupling efficiency is given by:

$$\eta = C \cdot \left|a(0)\right|^2 \tag{3.14}$$

where *C* is a constant which represents the transition ratio of the power from the grooved grating region to the waveguide region, $a(x)$ is the reduced field amplitude in the grating region, which is determined by three contributions: the amplitude decay rate α due to grating diffraction, the external fiber source distribution, $s(x)$, and the

wavevector mismatch, $\Delta\beta$. It should be noted that, for the input-coupling, the diffracted inhomogeneous plane wave in the grating region has a tangential wavevector $\beta_{-1}^{x} = \beta_{w} - \Delta\beta$, so $a(x)$ has a factor of $e^{-(\alpha+\Delta\beta i)x}$. The reduced field amplitude $a(x)$ therefore satisfies the differential equation [78], [92]:

$$\frac{da(x)}{dx} = -(\alpha + i\Delta\beta)a(x) + c \cdot s(x) \tag{3.15}$$

Based on Eq.(3.14) and Eq.(3.15), the solution of the coupling efficiency can be written as Eq.(3.16), of which we make the integral operation over the grating area in [-L_g, 0], and the final expression of the coupling efficiency is given by Eq.(3.17).

$$\eta = C' \left| \int_{-Lg}^{0} e^{(\alpha+i\Delta\beta)x} e^{-(x+d)^2/w_1^2} dx \right|^2 \tag{3.16}$$

$$\begin{cases} \eta = \dfrac{1}{4} C' \pi w_1^2 e^{\frac{1}{2}(-4\alpha d + \alpha^2 w_1^2 - \Delta\beta^2 w_1^2)} \cdot C_{erf} \\ C_{erf} = \left| -Erf[-\dfrac{d}{w_1} + \dfrac{1}{2}(\alpha + \Delta\beta i)w_1] + Erf[\dfrac{-d + L_g}{w_1} + \dfrac{1}{2}(\alpha + \Delta\beta i)w_1] \right|^2 \end{cases} \tag{3.17}$$

C' is a constant coefficient by integral. The coupling efficiency calculated using Eq.(3.17) is the absolute efficiency, in order to examine the efficiency drop caused by the wavevector mismatch, we define the normalized efficiency referring to the zero detuning as below:

$$\eta_0 = \frac{\eta}{\eta\big|_{\Delta\beta=0}} = e^{-\frac{1}{2}\Delta\beta^2 w_1^2} \cdot \frac{C_{erf}}{C_{erf}\big|_{\Delta\beta=0}} \tag{3.18}$$

Consider 1 dB normalized efficiency in Eq.(3.18), i.e. η_0=$10^{-0.1}$, and based on the relationship between the wavelength deviation and the wavevector mismatch given by

Eq.(3.7), we can obtain the corresponding wavelength deviation that resulting in 1 dB efficiency drop given by Eq.(3.19). It is worth to mention that $\Delta\lambda_{1\mathrm{dB}}$ indicates the wavelength variation for 1 dB efficiency drop at each side of the resonant wavelength, which should be calculated separately for both regions (i.e. for both cases of $\Delta\beta > 0$ and $\Delta\beta < 0$, or say, for the corresponding wavelength region $\lambda < \lambda_0$ and $\lambda > \lambda_0$). In the discussion below, we call $\Delta\lambda_{1\mathrm{dB}}$ as 1 dB wavelength variation. $\Delta\lambda_{1\mathrm{dB}}$ is defined as the absolute value of wavelength shift from the resonant wavelength λ_0 which leads to 1 dB drop in coupling efficiency.

$$\begin{cases} \Delta\lambda_{1dB} = \dfrac{1}{\left|\dfrac{1}{\Lambda} - \dfrac{dn_w(\lambda_0)}{d\lambda}\right|} \cdot C_{1dB} \\ C_{1dB} = \dfrac{\lambda_0}{2\pi w_1}\sqrt{\dfrac{ln10}{5} + 2ln\dfrac{C_{erf}}{C_{erf}\big|_{\Delta\beta=0}}} \end{cases} \tag{3.19}$$

By substituting Eq.(3.13) into Eq.(3.19), $\Delta\lambda_{1\mathrm{dB}}$ can be related to fiber numerical aperture and divergence angle given by:

$$\Delta\lambda_{1dB} = \frac{1}{\left|\dfrac{1}{\Lambda} - \dfrac{dn_w(\lambda_0)}{d\lambda}\right|} \cdot \frac{n_0\cos(\theta_i)\cdot\lambda_0}{2\pi[w_0 n_0 + h\cdot \mathrm{NA}/\cos(\psi)]}\sqrt{\frac{ln10}{5} + 2ln\frac{C_{erf}}{C_{erf}\big|_{\Delta\beta=0}}} \tag{3.20}$$

$$\mathrm{NA} = n_0 \sin\psi \approx \lambda_0 \,/\, \pi w_0 \tag{3.21}$$

Using Eq.(3.21), we can also write the rigorous bandwidth formula in other equivalent forms. Compared Eq.(3.19) and Eq.(3.20) to the bandwidth formulas in references [75] and [77], we find that the 1 dB bandwidth coefficient introduced in these references should not be a constant, which is actually determined by both the fiber and grating parameters. We will analyze these parameters in detail in later section.

Here several grating couplers are taken as examples to discuss the bandwidth calculation using the derived rigorous bandwidth formula. The analytical solution will be compared with the FDTD calculation and reported experimental results for verification. Here, Lumerial FDTD solutions is used for all the simulation calculations [2]. In Table 1, C-I is a silicon grating coupler with a poly-silicon overlay[70], and it works at TE polarization. C-II is conventional TE grating silicon coupler with shallow etch depth [93]. C-III is a horizontal slot waveguide grating coupler for TM mode excitation proposed in [77]. C-IV is a 400 nm silicon nitride grating coupler which has fully etched structure with pitch of 1.14 μm and filling factor of 50%. While BOX layer thickness is tuned to 2.2 μm, the best efficiency of 45% is achievable. The main parameters required for calculation include the grating dispersion at resonant wavelength, grating pitch Λ, amplitude decay rate α, fiber x-axis position d and width w_0. Note that here the fiber position d is optimized for the best efficiency in these references as it is used in practical cases. Grating dispersion can be easily obtained by mode field analysis using COMSOL[1]. With FDTD technique[2], through observing the mode field decay of the guided mode propagating in the core layer of the grating region, α value can be obtained. It is worth to mention that α is the field amplitude decay, i.e. half of the decay rate in intensity. α is determined by the grating dimension parameters

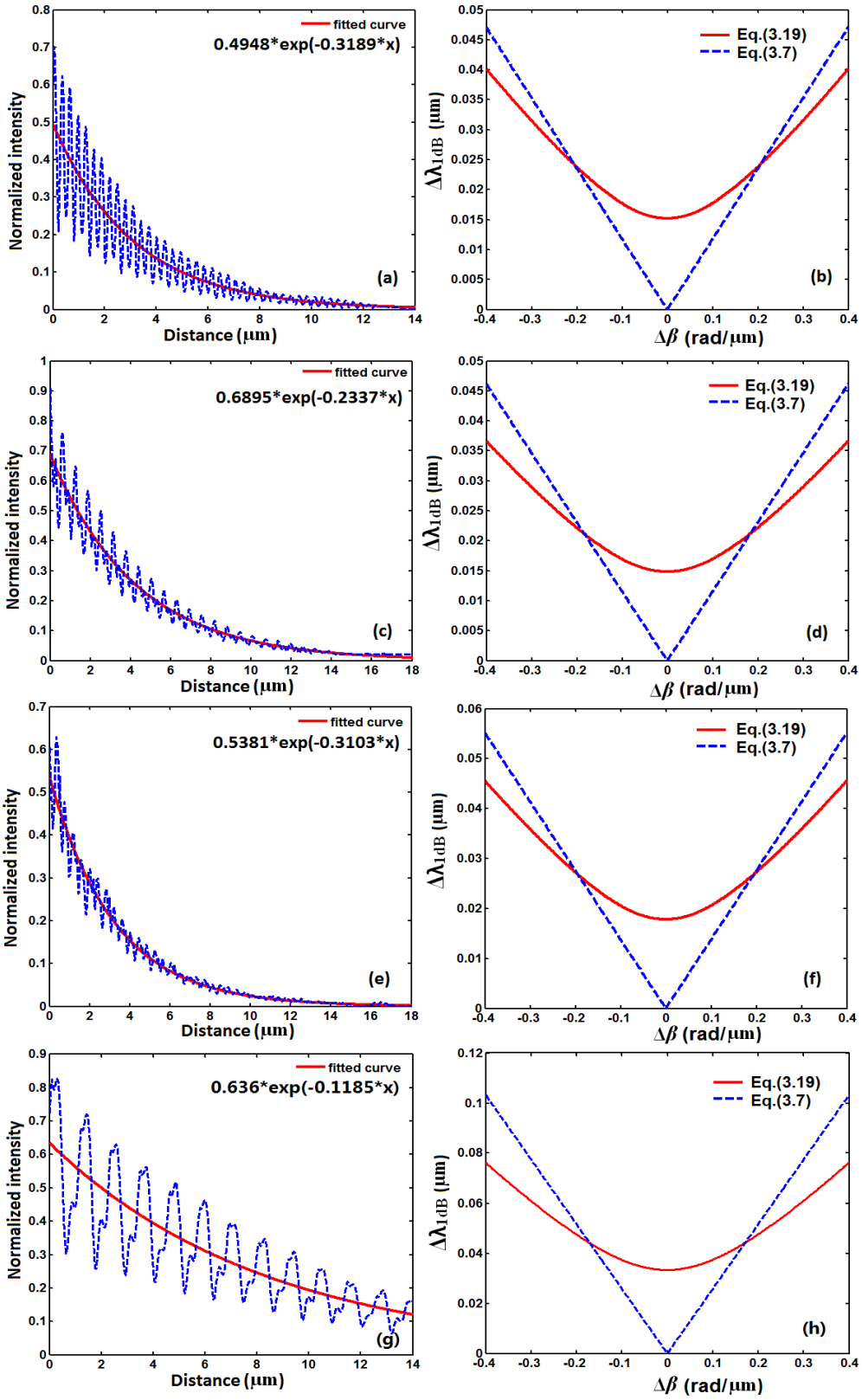

Figure 3.7 Grating field decay and the bandwidth calculation by Eq.(3.7) and Eq.(3.19): (a) and (b) for C-I; (c) and (d) for C-II; (e) and (f) for C-III; (g) and (h) for C-IV

Table 1. *Grating parameters and bandwidth calculation by FDTD and formula*

Parameters & performance		**C-I**	**C-II**	**C-III**	**C-IV**
Grating & fiber parameters	Λ (nm)	610	630	814	1140
	$dn_w(\lambda)/d\lambda$ (μm^{-1})	-0.457	-0.55	-0.56	-0.078
	amplitude decay rate α μm^{-1}	0.1595	0.1169	0.1552	0.0592
	fiber x position d (μm)	3.6	4.2	3.8	3.8
	incident angle θ_i	10^o	10^o	8^o	8^o
	beam width w_0 (μm)	5.2	5.2	5.2	5.2
Bandwidth	$\Delta\lambda_{1dB}$ by FDTD calculation	50 nm	44 nm	60 nm	86 nm
	$\Delta\lambda_{1dB}$ by experiment	50 nm	42 nm	--	--
	$\Delta\lambda_{1dB}$ by Eq.(3.7) and (3.19)	48 nm	44 nm	56 nm	86 nm
Efficiency	η_p by simulation	66%	36%	65%	45%

such as the etch depth and is also wavelength dependent, but here we choose a fixed decay rate value calculated at resonant wavelength to simplify the derivation and the rationality of this operation is discussed in detail in later section. The intensity decay profiles for the grating couplers C-I, C-II, C-III and C-IV are illustrated in Figure 3.7 (a), (c), (e) and (g), respectively. The intensity decay factors are calculated by fitting the exponent coefficient indicated in Figure 3.7. Utilizing the parameters listed in Table 1, we can plot the two curves determined by Eq.(3.7) and Eq.(3.19) to calculate the 1 dB bandwidth for the four grating couplers in Figure 3.7 (b), (d), (f) and (h), respectively. (The bandwidth can't be calculated solely by Eq.(3.19), because the 1 dB $\Delta\beta$ variation also exists in C_{1dB}). In this group of figures, two intersection points actually indicate two solutions of the equation system by Eq.(3.7) and (3.19). The ordinates of the two intersections correspond to the 1 dB wavelength variation $\Delta\lambda_{1dB}$ in the cases of $\lambda < \lambda_0$ and $\lambda > \lambda_0$, respectively. It is obvious that they have almost the same value, which can explain the nearly symmetric spectral response of grating couplers at both sides of the resonant wavelength. By summing up the wavelength variations (or approximating by doubling the $\Delta\lambda_{1dB}$), we can obtain the total 1 dB

bandwidth for the three grating couplers. The bandwidth results are given in Table 1 along with the cited simulation and experimental results. We can see that the bandwidths calculated by the derived rigorous equations have a good agreement with the simulation and experimental results. Based on Figure 3.7 (b), (d), (f), (h) and Table 1, we can also observed that, for these grating couplers excited by fiber beam of 10 μm mode field diameter, the wavevector mismatch is about 0.2 rad/μm for 1 dB wavelength variation while the fiber position is optimized for the best efficiency using the approach reported in previous work [21]. Eq.(3.7) and Eq.(3.19) reflect the intrinsic bandwidth property of grating couplers which does not include external layer factors such as the substrate, BOX layer, and top cladding. However, we also observe that while the parameters of external layers are optimized to achieve the best coupling efficiency for practical purpose, i.e. exerting constructive interferences into the grating region, then the interfaces outside the grating layers have little impact on the achievable bandwidth. Taking the substrate reflection as an example, the reflection normally has a spectrum with much wider bandwidth than the coupling bandwidth due to the short optical path difference. While the layer is tuned for constructive interference back into grating region, the peak of both spectrums will be overlapped at the resonant wavelength; because of the relatively small power of the reflection light and its large bandwidth, it has little impact on the coupling bandwidth.

3.3.3 Investigation on the effect of individual parameter on grating coupler bandwidth

In this section, we investigate the effect of individual parameters on bandwidth performance of planar waveguide grating couplers. We take grating coupler C-I as an example for this part of discussion. Normally for silicon grating couplers, L_g can be set as 30 times of grating period Λ (L_g should be larger than $2w_0$) and a larger L_g will

not affect the coupling performance. Likewise, both the analytic results and FDTD calculation results are provided as a comparison. Lumerial is used for all the FDTD simulations in later discussions[2] In Eq.(3.19), the grating pitch and dispersion relationship are determined by the grating materials and structure, which are fixed after the grating design. Here, we focus on discussion of the parameters in C_{1dB} including the fiber x-axis position d, fiber beam size w_0 and amplitude decay factor α. Let us first examine the dependency of coupling bandwidth on the fiber position.

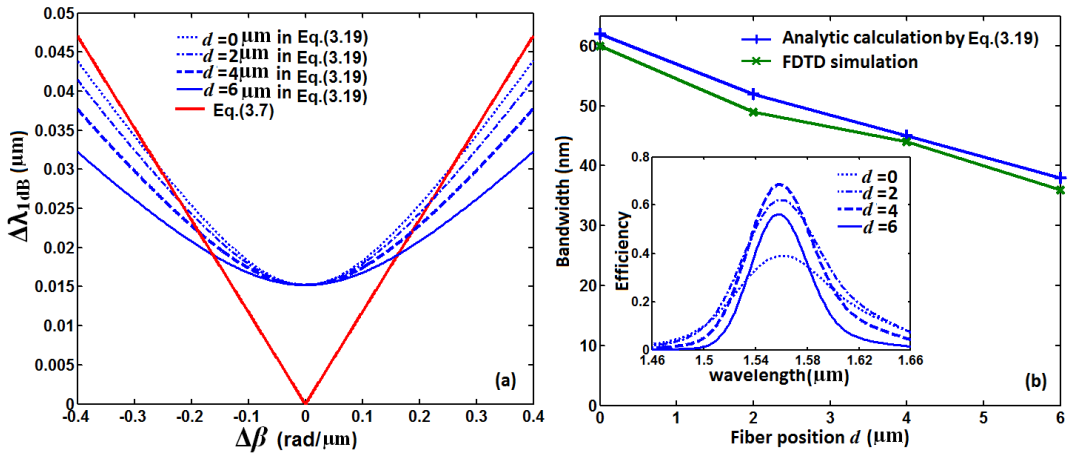

Figure 3.8 (a) A analytic bandwidth calculation based on Eq.(3.7) and Eq.(3.19) for different fiber x-axis position d; (b) Comparison of the bandwidth calculation by FDTD simulation and analytic results. Inset: spectral response obtained by FDTD simulation.

Figure 3.8 (a) illustrates the bandwidth calculated by Eq.(3.7) and (3.19) for a group of different fiber position values. It can be seen that the 1 dB bandwidth decreases with increase of fiber position d. The same trend is also achieved by the FDTD results shown in the inset of Figure 3.8 (b). The comparison of bandwidth calculation by the rigorous equations and simulation results is also illustrated in Figure 3.8 (b), which indicates a good agreement. The small difference ($\pm$ 4 nm) of both bandwidth results comes from the calculation accuracy limitation. Calculation accuracy limitation

mainly comes from two aspects – the calculation error of various parameters in analytical bandwidth formula, and the sampling resolution of the variables, such as wavelength λ and wave vector mismatch $\Delta\beta$ etc. in the calculation.

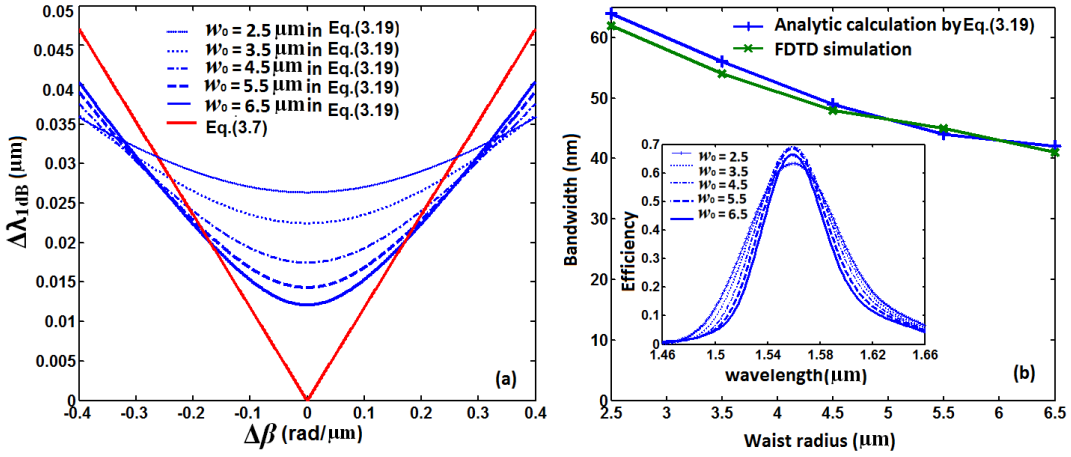

Figure 3.9 (a) Analytic bandwidth calculation based on Eq.(3.7) and Eq.(3.19) for different fiber width w_0; (b) Comparison of the bandwidth calculation by FDTD simulation and analytic results. Inset: spectral response obtained by FDTD simulation.

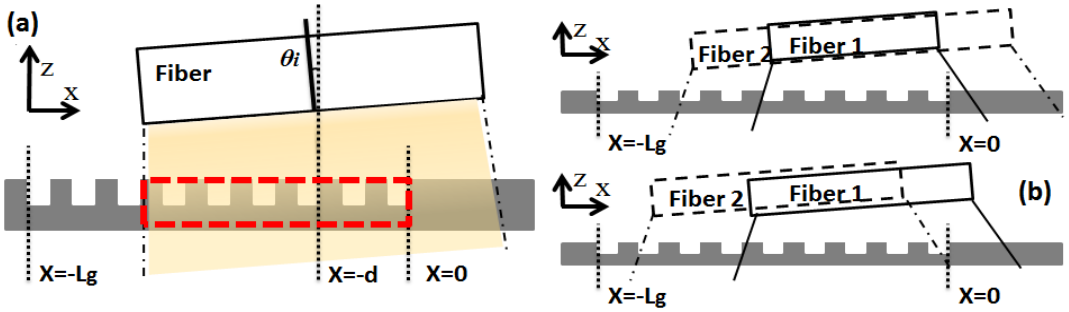

Figure 3.10 Illustration of "effective interaction area" and its variation as fibers beam width and position changes

Then, we investigate the effect of fiber beam width w_0 on the coupling bandwidth. In the same way, the analytic results are illustrated in Figure 3.9 (a). It can be observed that the coupling bandwidth will increase when the grating is excited by a fiber beam with smaller width. The results of FDTD calculation are given in the inset of Figure

3.9 (b), which verifies the trend. The comparison of 1 dB bandwidth calculated by the rigorous equations and simulation results is also given in Figure 3.9 (b). By comparing the Figure 3.8 (b) and Figure 3.9 (b), we observe that to adjust the beam width is a better choice to broaden the coupling bandwidth because it would not induce great efficiency drop while increasing the coupling bandwidth. In addition, according to Eq.(3.21), it is known that the Gaussian beam with smaller beam width exerts a larger numerical aperture. It means that to increase the incident beam numerical aperture will also broaden the coupling bandwidth.

These relationships are directly determined by the monotonicity of the solution of Eq.(3.7) and (3.19). The curve of Eq.(3.7) is unchanged once the grating structure is fixed. Thus, $\Delta\lambda_{1dB}$ is mainly affected by the parameters of C_{1dB} in Eq.(3.19). By examining the mathematic properties of C_{1dB}, we give a more intuitive explanation for these relationships. We first introduce a definition of "effective interaction area", that is, the fiber beam effectively covered grating area. In Figure 3.10 (a), the dash-line labeled area indicates the effective interaction area. To alter the fiber beam width or position is inherently changing the size of effective interaction area and power distribution in the area. Figure 3.10 (b) intuitively illustrates the effective interaction area when fibers beam width and position changes. It is clear that a larger beam width or a further distance between the fiber center and the first grating pitch ($x = 0$) exerts a larger interaction area, which will result in narrower coupling bandwidth according to the aforementioned discussion. The trends can be simply understood that since the wavevector mismatch always exists in the effective interaction area for the wavelengths that deviating the resonant wavelength λ_0, so a traveling distance in the area will induce more serious efficiency drop for these wavelengths and therefore narrow down the coupling bandwidth. Since the integral operation needs to be done

over the whole effective interaction area, a longer effective interaction area in the propagation direction therefore results in a smaller coupling bandwidth. It is easy to imagine that the size of the effective interaction area will become constant while the distance d from the first grating pitch to fiber center is large enough (larger than w_1). In Figure 3.11 (a), we show the bandwidth calculation for the case that the fiber is put relatively far away from the grating beginning (d equals to 10, 11, 12 and 20 μm). It can be seen that the 1 dB bandwidth is almost unchanged (about 30 nm) even though d keeps increasing. The results are verified by FDTD simulation as well.

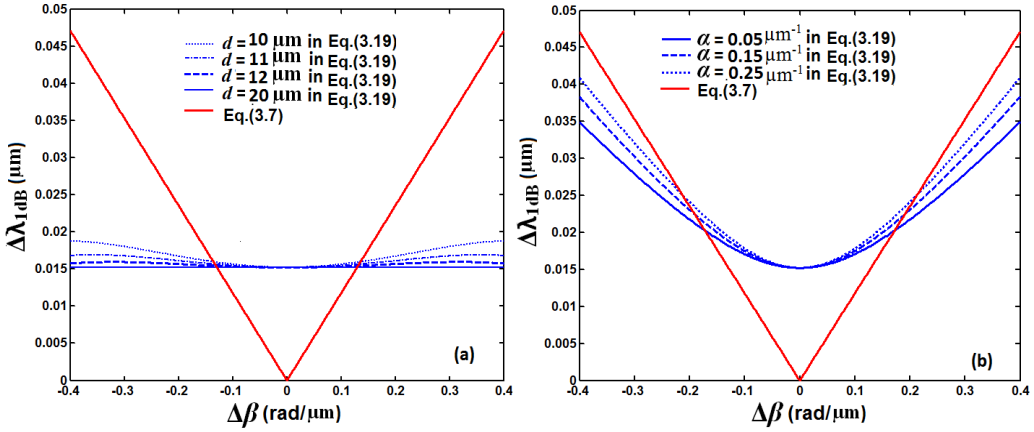

Figure 3.11 (a) Analytic bandwidth calculation based on Eq.(3.7) and Eq.(3.19) for relatively large fiber position d; (b) Analytic bandwidth calculation for different field amplitude decay rate α

Finally, we investigate the relationship between the bandwidth and the field amplitude decay rate α. α is not easy to be solely adjusted because other parameters in Eq.(3.19) such as grating pitch and dispersion will also change correspondingly when the grating structure changes. Here, we just simply consider the monotonicity of the bandwidth versus the field amplitude decay rate α by assuming other parameters remain unchanged. In Figure 3.11 (b), we change the field amplitude decay rate α with value of 0.05, 0.15 and 0.25 μm^{-1} to calculate the 1 dB bandwidth. We can see

that the bandwidth monotonically increases with the increase of α. However, in practical design, it should be noted that the decay rate α will affect the coupling efficiency and increase of α will lead to decrease of the achievable coupling efficiency. It is worth to mention that the value of α is actually wavelength dependent by the rule that modes at larger wavelength have larger decay within a fixed grating structure. In aforementioned discussion, we simplify the bandwidth formula derivation by calculating the decay factor α at the resonant wavelength λ_0. This actually provides an average value for bandwidth estimation (note that the calculation by Eq.(3.7) and Eq.(3.19) is implemented at both sides of the resonant wavelength, i.e. both $\lambda < \lambda_0$ and $\lambda > \lambda_0$). Besides, within the concerned wavelength range of 1 dB bandwidth, α change is also very limited. In Figure 3.11(b), the field amplitude decay rate α is spacing with interval of 0.1 μm^{-1}, which is actually a large value. Based on our calculation, the wavelength should change more than 100 nm to make α increase or decrease by 0.1 μm^{-1} (Taking C-I as example, 100 nm change in wavelength will cause 0.07 μm^{-1} change of α), and combined with the opposite trends at each side of the resonant wavelength (α decreases for $\lambda < \lambda_0$ and increases for $\lambda > \lambda_0$), it is reasonable to calculate the 1 dB bandwidth with an average α obtained at resonant wavelength.

3.3.4 Bandwidth mechanism for waveguide to fiber excitation

Owing to reciprocality of the fiber-to-chip grating coupling system, the transmission spectrum is the same for waveguide to fiber and fiber to waveguide coupling. The rigorous bandwidth formula can be adapted for the chip-to-fiber output coupling. In this section, we give a brief discussion on the case of waveguide to fiber output coupling. The model of waveguide to fiber coupling is shown in Figure 3.12 (a). The output coupling can be described as the guided mode propagating along an open periodic dielectric waveguide (grating region) [78] and the optical power gradually

radiates into the claddings. The grating coupler is regarded as a structure that transforms a surface wave into one or more leaky waves (space-harmonic fields) into top cladding and the BOX layer. The upward power will be partly collected by the fiber. The wavevectors of each order of space-harmonic waves are related by [78], [94]:

$$\boldsymbol{\beta}_q = \boldsymbol{\beta}_w + q\boldsymbol{K} \tag{3.22}$$

where q=0, ±1, ±2, ..., q is the order number, $\boldsymbol{\beta}_w$ is the wavevector of the guided mode in the grating structure, and $\boldsymbol{\beta}_q$ is the wavevector of the q^{th} order space-harmonic wave. In the tangential direction, Eq.(3.22) can be written for -1 order wave as below:

$$\beta_{-1}^{x} = \beta_w - \frac{2\pi}{\Lambda} \tag{3.23}$$

The corresponding expression in form of the effective index can be written as:

$$n_0 \sin\theta_r(\lambda) = n_w - \frac{\lambda}{\Lambda} \tag{3.24}$$

where n_w is the effective index of the guided mode in the grating structure. θ_r is the diffraction angle. θ_r can be viewed as a function of wavelength, that is, the radiation angle of the space-harmonic wave is wavelength dependent.

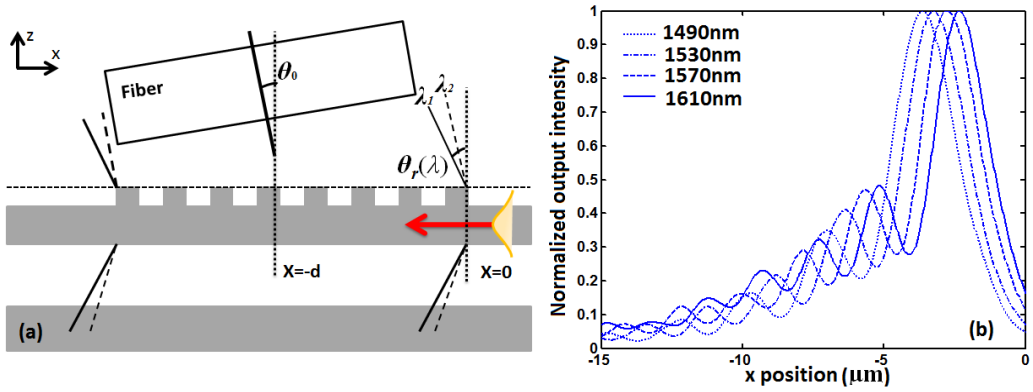

Figure 3.12 (a) Modeling of output coupling from waveguide to fiber coupling; (b) Typical intensity profile of the output radiation waves

Taking grating coupler C-II as an example, the output intensity profile is illustrated for several different wavelengths in Figure 3.12 (b). It can be seen that the intensity peak shifts with different wavelength. The amplitude decay rate α is a critical parameter determining the shape of the output profile. More details of the output intensity profile of grating couplers were theoretically investigated in [71]. Since the fiber has a tilt angle θ_0, it can more effectively receive the radiation wave transmitted upward at this angle. Thus, the coupling efficiency of the corresponding wavelength wave will be higher than other wavelengths, which leads to a coupling window of certain bandwidth. Based on this understanding, the bandwidth of grating coupler may be approximated by relating the 1 dB wavelength variation to the derivative of θ_r. In previous work, the bandwidth formula for the output coupling is derived by introducing a constant 1 dB coefficient as (note that in this thesis, $\Delta\lambda_{1\mathrm{dB}}$ means 1 dB wavelength variation instead of the total 1 dB bandwidth) [75]:

$$\Delta\lambda_{1dB} = \frac{n_0\cos(\theta_0)}{\left|\frac{1}{\Lambda} - \frac{dn_w(\lambda_0)}{d\lambda}\right|}\cdot\eta_{1\mathrm{dB}} \tag{3.25}$$

Comparing Eq.(3.25) with Eq.(3.20), we can find that both the formulas have the similar form, and the bandwidth coefficient can be expressed as:

$$\eta_{1\mathrm{dB}} = \frac{\lambda_0}{2\pi[w_0 n_0 + h \cdot \mathrm{NA}/\cos(\psi)]}\sqrt{\frac{In10}{5} + 2In\frac{C_{erf}}{C_{erf}\big|_{\Delta\beta=0}}} \tag{3.26}$$

Likewise, $\eta_{1\mathrm{dB}}$ is a function of fiber and grating parameters including d, w_0 and α (NA and divergence angle are directly determined by the fiber beam width w_0 according to Eq.(3.21)). Here, we give an intuitive explanation on these monotonic relationships for the output coupling case. As stated for the input coupling case, we know that increasing the fiber x-axis position d and beam width w_0 will decrease the coupling bandwidth owing to a larger effective interaction area. Similarly, for the output coupling case, we can define an "effective collection area" at the fiber butt. The amount of receiving power can be calculated through integral of the Pointing vector over this area. Thus, a larger effective collection area of the fiber will increase the difference in collecting efficiency between the radiation wave of the best accepting wavelength (i.e. the wave transmitting upward right at the fiber tilt angle) and other wavelengths, and therefore leads to a narrower coupling bandwidth. Obviously, to increase the fiber x-axis position and beam width are the means to increase the effective collection area. In addition, as for the amplitude decay rate α in the coefficient $\eta_{1\mathrm{dB}}$, it is known that the shape of the output intensity profile also affect the coupling performance; α will affect the output intensity profile [16] and thus influence the bandwidth behavior. The monotonic relationship of the coupling bandwidth versus the field amplitude decay rate α has been discussed for the input coupling case. Thus, the bandwidth mechanism of grating couplers is systematically discussed for both input and output coupling cases.

3.4 A simplified design process and its application on design of horizontal slot waveguide grating couplers

Based on the discussion in section 3.3, we understood the bandwidth mechanism of grating couplers as well as several practical optimisation principles to increase the bandwidth of fiber-to-chip grating interface. However, for a grating coupler design, to increase the coupling efficiency is always the most important consideration. The optimisation of coupling efficiency normally involves many factors including the internal parameters such as the groove height and etch depth as well as the external parameters such as BOX layer and top cladding thickness. This results in a multi-parameter optimisation problem, usually a time-consuming scanning process. In order to reduce the design complexity, here we propose a method by separating optimisation parameters in a sequence of steps shown in Figure 3.13 to simplify the optimisation process for grating couplers.

We first focus on the structure with semi-infinite cladding and BOX layer, and optimize the film structure. Here we fix the duty ratio at 50% for better fabrication tolerance. Figure 3.13 (a) is a waveguide structure to be coupled. In Figure 3.13 (b), we first tune the film structure so that out of plane percentage transmission of the unpatterned grating region is at 50%. This number is an observation from many numerical simulations for different grating structures. The optimum efficiency is always achieved with certain unpatterned film structure that gives balanced film transmission and reflection for incident waves which are injected at the same angle as the tilted fiber. If the unpatterned structure has multi-layer films configuration, it should include the full stack of films for the films' transmission calculation.

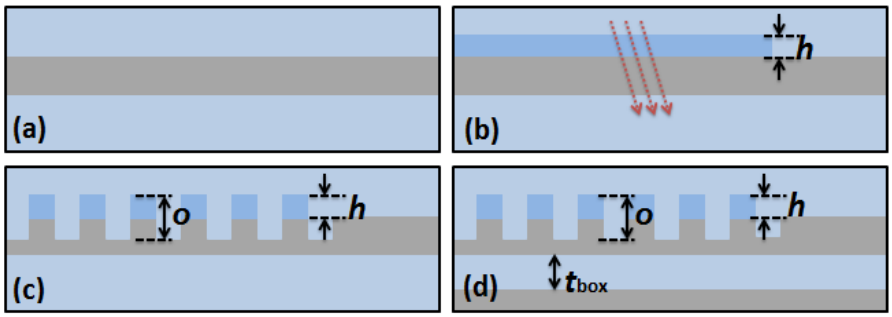

Figure 3.13 The parameter-separate optimisation process. (a) Planar waveguide structure; (b) Optimize the unpatterned grating region with an overlay for half film transmission; (c) Scan for the best etch depth; (d) Tune the external interference layers

For practical reasons, when tuning the film structure we only add an extra overlay with tunable thickness (*h*) on top of the existing waveguide structure and the refractive index of the overlay can be different to that of the waveguide layer. Taking a recent demonstration [8] as an example, we illustrate our observations in Figure 3.14 (a) which shows the achievable coupling efficiency (by scanning *o*) and film transmission coefficient as a function of the overlay thickness *h* operating at 1.55 μm. We can see that the maximum coupling coefficient is achieved at an *h* value that gives the 50% film transmission. This phenomenon was observed in all the simulations we have done on various layered grating structures including horizontal slot waveguide structures we will show later. One thing we should note is that there are more than one values of *h* lead to the 50% film transmission and among them only one *h* value will give us the maximum coupling efficiency, which means we can use the 50% film transmission as a criteria to narrow down the optimisation dimension associated with *h* to some (normally two or three) discrete values which will be used in the following optimisation steps. A practical consideration here is that the thickness of the overlay (*h*) cannot be too big otherwise the mode mismatch between the grating region and waveguide will reduce the coupling efficiency. Then, we optimize the etch depth (*o*)

by scanning *o* over a reasonable region using the values of *h* obtained from the previous step as shown in Figure 3.13 (c). This step was illustrated in Figure 3.14 (b) which shows the coupling efficiency versus the etch depth at three discrete values of *h* with 50% film transmission identified with the blue curve in Figure 3.14 (a). It is clear that among the three *h* values the best coupling efficiency (about 60%) is achieved at *h* = 160 nm (*o* = 220 nm). After the two steps mentioned above, we have achieved the optimum grating structure whose performance can be further enhanced (to a relatively small extent [70]) by adding external layers (Figure 3.13 (d)) such as BOX layer, top cladding layer, or a DBR. The effect of external layers is widely discussed in previous literatures [72].

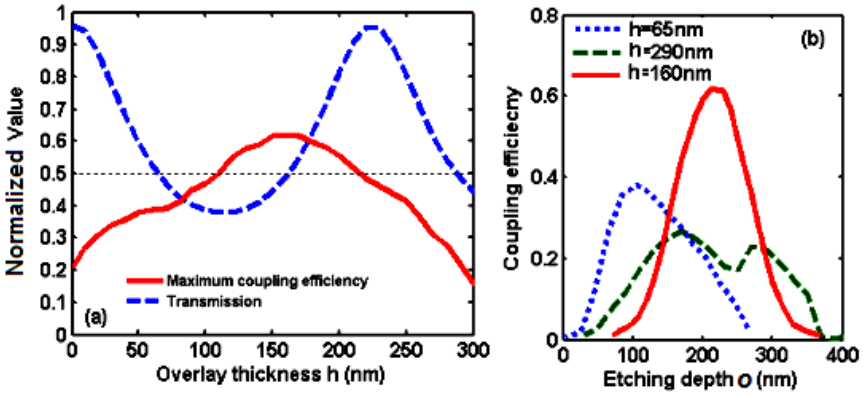

Figure 3.14 (a) The optimum coupling efficiency and film transmission at different overlay thickness; (b) The coupling efficiency versus the etch depth while overlay thickness is 65 nm, 160 nm and 290 nm

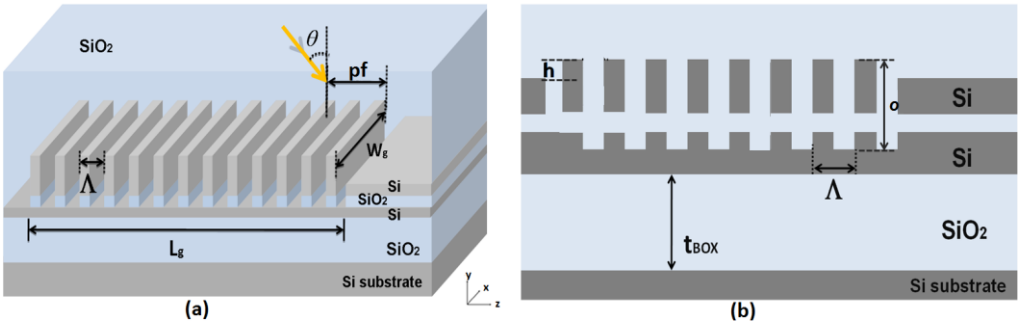

Figure 3.15 (a) Proposed grating coupler structure. (b) Schematic showing main parameters.

To illustrate our proposed optimisation process, here we demonstrate how to optimize a grating coupler at telecommunication wavelengths for a horizontal slot (H-slot) waveguide [95]. The reason we choose H-slot waveguide as an example is because it has a layered sandwich structure which can prove that our method is generally suitable for design of layered grating couplers, besides the low index core layer will give us a relative low grating effective index to reduce the term $1/\Lambda$ in denominator of Eq.(3.20), and the layered grating structure has a comparable dispersion with typical silicon grating coupler, so it is expected to achieve a broadband coupling performance.

We design the horizontal slot waveguide grating coupler by following the aforementioned process. The proposed coupler structure and the main parameters are shown in Figure 3.15. The coupler works at TM polarization with field enhancement in the low refractive index slot [35]. The refractive indices of Si and SiO_2 are 3.48 and 1.46, respectively. The waveguide section has a 50 nm SiO_2 slot layer sandwiched by two silicon slabs with thickness of 205 nm. The fiber tilt angle is positive 8^o. The film design is optimized with an overlay h = 135 nm for 50% film transmission of which the spectral dependence is illustrated in Figure 3.16 (c). The etch depth o is 420 nm which is optimized for better coupling at 1.55 μm wavelength, and the grating pitch calculated is 814 nm. Figure 3.16 (a) indicates the coupling performance of the grating coupler. The peak efficiency of 65% with 60 nm 1 dB bandwidth is achieved for the grating coupler while the BOX layer thickness is optimized to 3.4 μm. The coupling performance is much better than the previously reported results, i.e. 48% coupling efficiency and 35 nm 1 dB bandwidth without considering the optimisation of top film overlay thickness[12]. While the parameters of external layers are optimized to achieve the best coupling efficiency for practical purpose, i.e. exerting constructive interferences into the grating region, the interfaces outside the grating

layers have little impact on the achievable bandwidth. In Figure 3.16 (a), compared to the result without substrate, the coupling efficiency achieved with substrate and optimized BOX layer thickness has only around 5% increase and the bandwidth has nearly no change. Actually, the substrate reflection normally has a spectrum with much wider bandwidth than the coupling bandwidth due to the short optical path difference. While the layer is tuned for constructive interference back into grating region, the peak of both spectrums will be overlapped at the resonant wavelength; because of the relatively small power of the reflection light and its large bandwidth, thus it has little impact on the coupling bandwidth. Figure 3.16 (b) shows the mismatch between the effective index n_d of the diffraction light and real index n_w for the coupler. n_d is calculated according to Eq.(3.2), and n_w is calculated using the effective medium theory proposed in [90], the slope difference is about 1.788 μm^{-1}. Compared with the previously reported work[12], the H-slot waveguide grating coupler has a larger coupling bandwidth while remaining a high coupling efficiency.

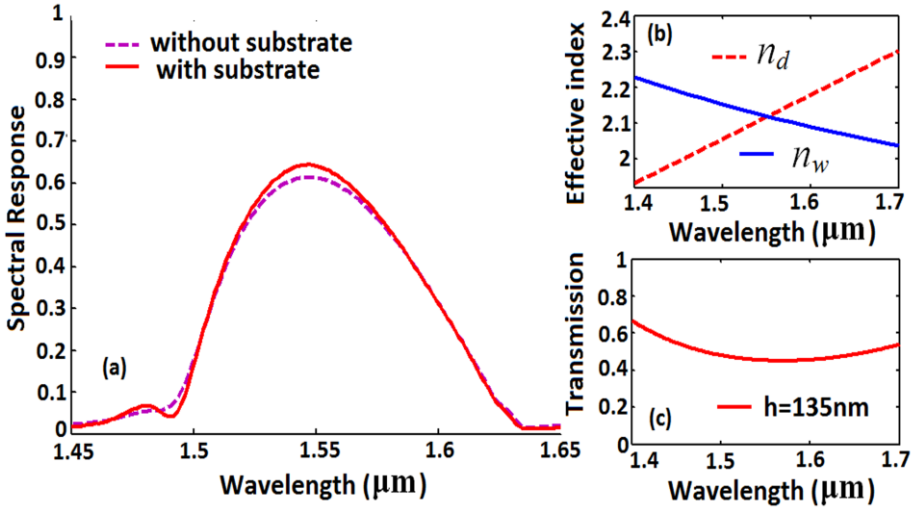

Figure 3.16 (a) The coupling efficiency of the proposed grating coupler with and without substrate. (b) The detuning between the n_{eff} of diffraction light and the actual n_{eff} of the grating coupler. (c) Film transmission spectrum of the unpatterned grating region.

3.5 Polarization insensitive grating coupler design using double surface-corrugation (DSC) structure

Conventional grating couplers normally operate at single polarization, exciting either TE or TM mode into planar waveguides at specific working wavelength. The resonant wavelength of TE mode is always longer than that of TM mode due to the asymmetric geometry of the grating region (i.e. the grating waveguide width is much larger than height and then the effective index of TE mode is larger that of TM mode). Therefore, it is difficult to effectively tune and utilize the resonance behavior of both TE and TM modes, which limits its potential for novel applications. In order to extend the functionalities, we propose grating couplers with double surface-corrugation (DSC) to adjust TE and TM mode excitation simultaneously. We observe that the diffraction effects of the two grating surfaces result in more resonance combinations compared with single grating, which enables the characterization of the resonance spectrum for both TE and TM modes. Based on the DSC structure, for the first time to our knowledge, we design a one dimensional (1-D) grating coupler which enables polarization-independent (POI) fiber-chip optical excitation. The operation principle of our proposed grating coupler is entirely different from the previously reported two dimensional (2-D) POI grating coupler [66], which works based on equal effective index of TE and TM mode through perturbation of the grating groove in lateral direction. The 1-D design is much easier to handle, and a simple design procedure is presented. The operation principle and design methods of the DSC based grating couplers are also theoretically discussed.

3.5.1 Operation mechanism of DSC grating coupler

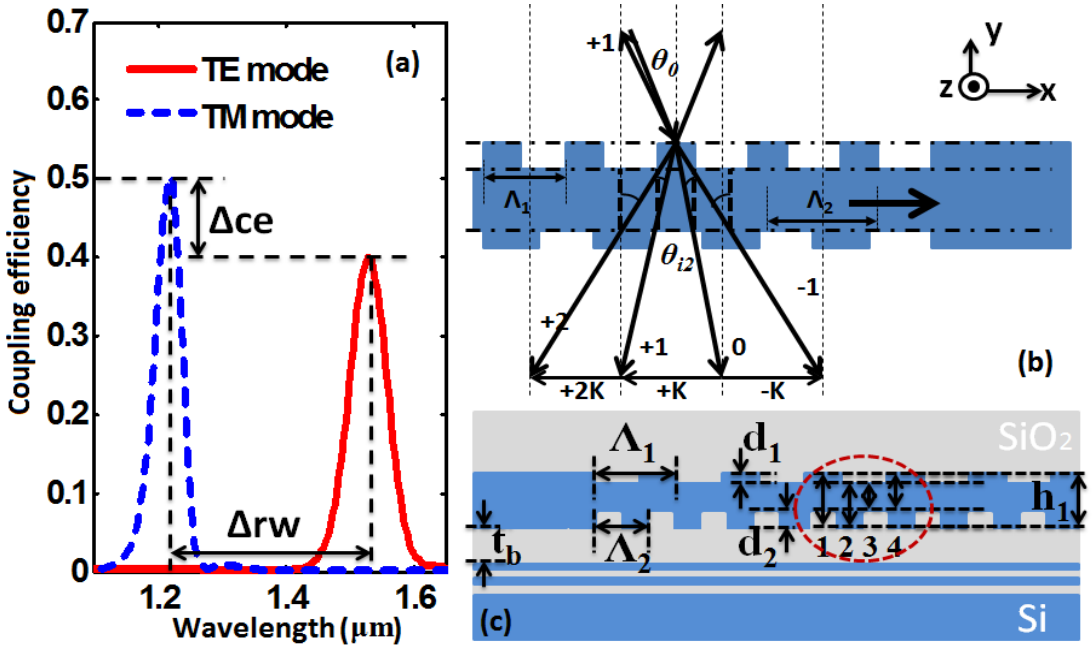

Figure 3.17 (a) Spectral response of both TE and TM mode excitation in a general 1-D grating coupler (b) Working principle and (c) Main parameters of DSC structure.

The typical spectral response of TE and TM mode excitations in a conventional 1-D grating coupler is illustrated in Figure 3.17 (a). TE mode is excited at wavelength longer than that for TM mode, and the achievable efficiency is usually different for each polarization. Provided that the wavelength space, Δrw, (in Figure 3.17 (a)) between TE and TM resonant wavelength and the corresponding efficiencies and their difference, Δce, (in Figure 3.17 (a)) can be adjusted to desirable values, many potential applications can be exploited, for example, double-channel communication or polarization-insensitive excitation (i.e. Δrw = 0, Δce = 0). We observed that, by using the sophisticated diffraction and interference effects inside the grating couplers with double-surface corrugation, it is possible to achieve such performance through a proper selection of dimension parameters. DSC grating structures were previously used to enhance the coupling efficiency [96], [97]. However, their investigations were

based on analytical studies under rigid assumptions, such as the same pitch for both corrugations with 50% filling factor. Nowadays, the photonic device design relies heavily on numerical methods which enable more flexible modeling and parameter selection. Since the DSC structure has a constant lateral geometry, accurate calculations can be obtained by 2-D modeling which is more time-saving and easier to handle. In this section, all the theoretical calculations are based on 2-D finite-difference time-domain (FDTD) algorithm using Lumerical FDTD Solutions[2]. Consider the basic model of a DSC grating coupler which is periodically corrugated at both top and bottom surfaces, as shown in Figure 3.17 (b) and (c). Unlike in the single grating structure case, the mode diffraction inside the perturbed dielectric layer of the DSC structure is a result of superposition of both corrugation surfaces. The principle of operation is intuitively illustrated in Figure 3.17 (b). The incoming fiber beam (with incident angle θ_0) strikes the top corrugated surface and experience the first diffraction. The diffracted lights with various angles θ_{i2}, then travel through the dielectric layer and reach the bottom surface where some of the lights are diffracted upward and travel back again to the top grating surface. The iterative process involves multi-diffraction and interference. In the DSC structure, the tangential wave vector $\boldsymbol{\beta}_{qp}$ of each diffracted light along the grating surface can be generally expressed by Eq.(3.27), which is applicable for both TE and TM modes.

$$\beta_{qp} = \beta_{in} - q\frac{2\pi}{\Lambda_1} - p\frac{2\pi}{\Lambda_2} \tag{3.27}$$

where $\boldsymbol{\beta}_{in}$ is tangential wave vector of incident light along the top grating surface, Λ_1 and Λ_2 are the pitch of top and bottom surface gratings, and q and p, are the diffraction orders for top and bottom gratings, respectively. The guided mode is excited when $\boldsymbol{\beta}_{qp}$ is equal to the wave vector of the guided mode in the grating region. For an infinite DSC structure, a combination of two corrugated grating surfaces can

be defined into four different height sections (indicated in Figure 3.17 (c)). Then, the effective indices of the guided TE and TM mode in DSC structure can then be estimated approximately using Eq.(3.28) according to effective medium theory [90].

$$n_{eff}^{\mathrm{TE}|\mathrm{TM}} = \sum_{i=1}^{4} n_i^{\mathrm{TE}|\mathrm{TM}} r_i \qquad (3.28)$$

where $n_i^{\mathrm{TE|TM}}$ stands for the effective index in each height sections for TE or TM mode, and r_i is the corresponding ratio of each height section in the grating structure. Compared with the diffraction effects in the single grating case (without the third item in the right hand side of Eq.(3.27)), the diffraction effects of the two grating surfaces have more resonance combinations, which enables the characterization of the resonance spectrum for both TE and TM modes simultaneously.

3.5.2 DSC based polarization independent grating coupler design

To verify the aforementioned mechanism, we design the POI grating coupler. In our design, the light beam from single mode fiber (10.4 μm diameter) is incident on the grating at a tilt angle of 8^{o}. We select a 660 nm thick unpatterned silicon layer as the basis to construct the DSC grating coupler. The thickness is not fixed and we can also achieve the POI behavior on thinner silicon layer (we will discuss this later). However, the silicon layer cannot be too thin, since thinner DSC structure has a lower refractive index contrast with the claddings which will result in the incident light traveling much easier through the DSC structure and leaking into the claddings. Moreover, thinner silicon layer will also limit the depth of grating grooves. According to Eq.(3.27) and Eq.(3.28), to allow the excitation of the guided mode, the selection of Λ_1 and Λ_2 should satisfy $2\pi n_{\mathrm{Si}}/\lambda \geq \boldsymbol{\beta}_{qp} \geq 2\pi n_{\mathrm{SiO_2}}/\lambda$, where, n_{Si} and $n_{\mathrm{SiO_2}}$ are the refractive index of Silicon (3.48) and SiO_2 (1.46), respectively. The tangential wave vector, $\boldsymbol{\beta}_{qp}$, is determined after the pitches are selected, then we can tune the etch

depth d_1 and d_2 of both grating surfaces to adjust the effective index of the guided mode of the grating region, making the structure resonate at desirable wavelength. For the POI DSC coupler, 50% fill factor is adopted, and the initial pitch values Λ_1 = 800 nm and Λ_2 = 640 nm are chosen for the top and bottom grating surfaces. The initial values are obtained according to several rounds of trials to make sure resonant wavelength of TE and TM modes are not far away each other. If necessary, they should be corrected by a little amount for a better polarization dependent loss (PDL) performance after tuning the etch depths. In order to enhance the coupling efficiency, a distributed Bragg reflector (DBR) is deployed at substrate side to reflect the transmitted light back into the DSC structure. The DBR consists of three pairs of cascaded 111 nm silicon and 269 nm silica layers, and the BOX layer thickness t_b is 1.5 μm.

In our design, only the etch depths d_1 and d_2 at both grating surfaces are required to be swept simultaneously to optimize the POI performance (i.e. to make |Δce| close to 0 at 1.55 μm wavelength). The sweep results in the form of contour profile as illustrated in Figure 3.18 (a). The area in the profile indicated by a circle has the minimum |Δce|, hence the corresponding etch depths, d_1 = 80 nm and d_2 = 200 nm, are selected. It should be noted that if there is more than one area with value close to 0, we need to check each area and select the one with highest efficiency for design. The spectral response of the POI grating coupler is given in Figure 3.18 (b), it can be seen that multiple resonances exist for both TE and TM polarizations. By considering the intrinsic property of the grating structure (i.e. no external DBR and substrate layers are included), we observe that the resonant wavelengths basically remain unchanged. These mode resonant wavelengths can be theoretically verified based on Eq.(3.27) and Eq.(3.28). The external waveguide of 660 nm thickness can support multiple modes, and we observe that the TM_{00} fundamental mode and TE_{01} mode are excited in

the structure (TE_{mn}/TM_{mn} stands for the TE/TM mode with field distribution which has m "field zeros" in the z direction and n "field zeros" in y direction).

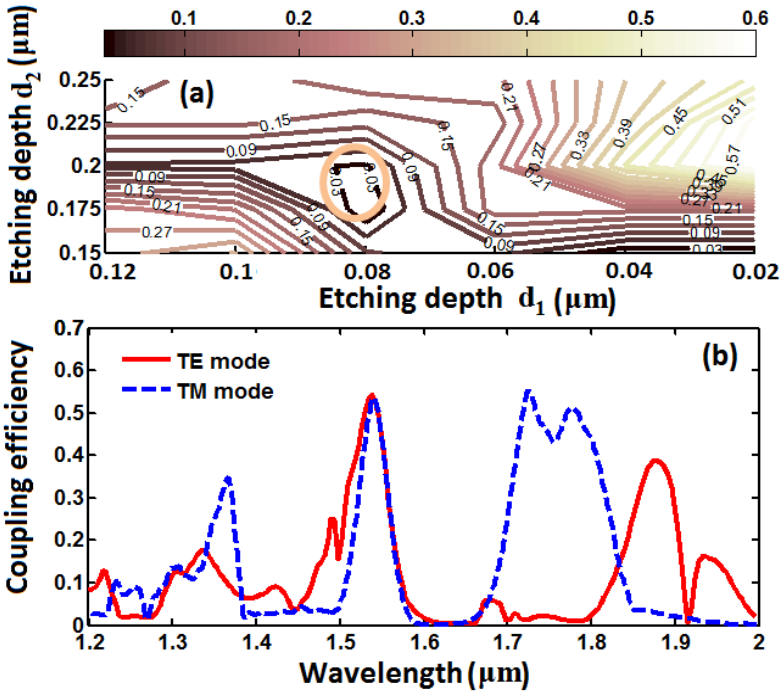

Figure 3.18 (a) Contour profile of Δce for sweep on etch depth d_1 and d_2;

(b) The spectral response of the POI grating coupler

Table 2. ***Comparison of the calculated βqp and βeff based on Eq.(3.27) and Eq.(3.28)***

TE mode					TM mode				
λ	q	p	β_{qp} (rad/μm)	β_{eff} (rad/μm)	λ	q	p	β_{qp} (rad/μm)	β_{eff} (rad/μm)
1.35 μm	1	-2	12.72	12.78	1.35 μm	-3	1	14.69	14.83
1.55 μm	-1	0	10.64	10.37	1.55 μm	1	-2	12.61	12.71
1.88 μm	0	-1	8.533	8.423	1.74 μm	-1	0	10.55	10.65

In Table 2, we calculate the wavevector $\boldsymbol{\beta}_{qp}$ of the effective diffracted light and the wavevector $\boldsymbol{\beta}_{eff}$ (= $2\pi n_{eff}/\lambda$) of the guided mode in the grating region at each resonant wavelength for a comparison. It can be seen that $\boldsymbol{\beta}_{qp}$ is very close to $\boldsymbol{\beta}_{eff}$ at each resonant wavelength λ, allowing the excitation of guided mode into the planar waveguide. In Figure 3.18 (b), it is also obvious that one resonant wavelength at 1.55 μm is shared by both TE and TM modes. A clearer spectrum of the POI grating coupler is given in Figure 3.19 (a) for the wavelength range from 1.5 μm to 1.6 μm.

The performance of the POI grating coupler for the TE and TM modes overlap quite well in the wavelength range of 1540–1580 nm, which implies good polarization independence. The polarization dependent loss performance is shown in Figure 3.19 (b). Polarization dependent loss is defined as a measure of the peak-to-peak difference in transmission of an optical component or system with respect to possible states of polarization. The POI grating coupler exhibits a high performance of polarization-independence around 1550 nm wavelength and the PDL is about 4.1×10^{-3} dB at 1550 nm. The PDL is less than 0.05 dB in the wavelength range of 1544 nm to 1561 nm, and less than 0.5 dB in a large range of 1535 nm to 1580 nm. The peak efficiency of 55% is achieved for both polarizations, and the 1 dB operation wavelength range is 1536–1563 nm for both TE mode and TM mode. We observe that each of the TE and TM diffractions will be primarily affected by one of the corrugated surfaces. In Figure 3.20, we illustrate the effect of top and bottom grating pitch changes on the resonant wavelength shift for TE and TM modes. We can see that the top grating surface primarily affects the TM mode and the bottom grating surface mainly affects the TE mode.

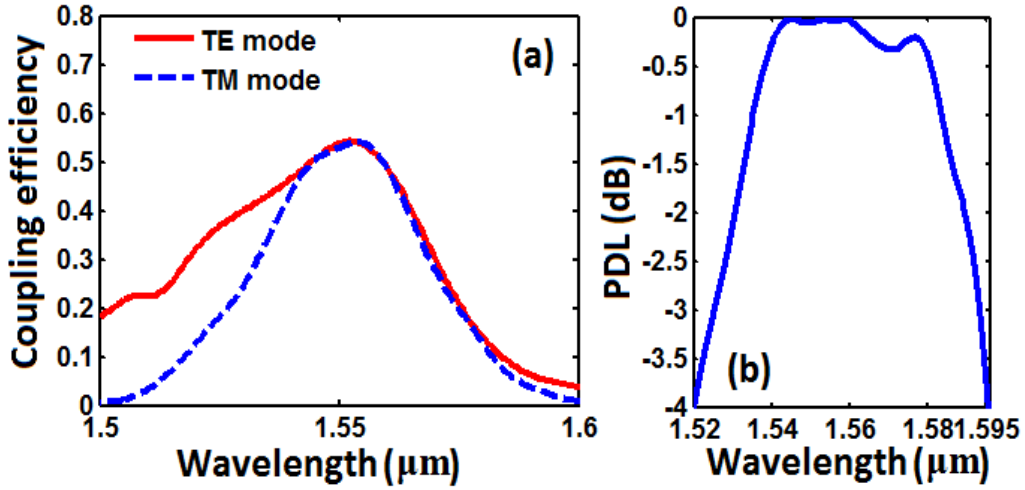

Figure 3.19 (a) The detailed spectral response for both TE and TM mode excitation in wavelength range of 1.5 μm to 1.6 μm (b) The PDL performance of the designed POI grating coupler.

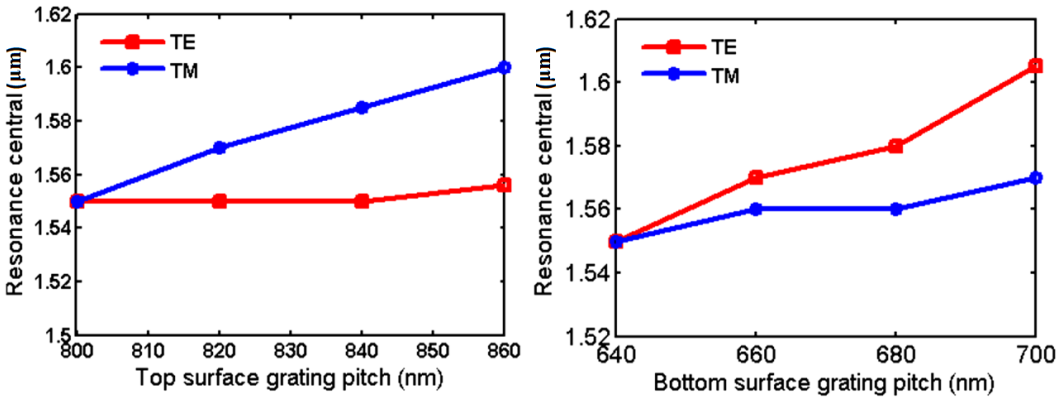

Figure 3.20 Top and bottom grating pitch changes versus the resonant wavelength shift

The double corrugation surface structure can be also constructed on thinner silicon layer. We also design a DSC based polarization independent grating coupler on 370-nm-thick silicon layer with backside DBR configuration to excite fundamental TE and TM modes. The spectral response of the POI grating coupler is shown in Figure 3.21(a). The achievable efficiency is around 50%. However, based on our investigation, we also find it is normally difficult to achieve high efficiency if the silicon layer is too thin. Due to perturbation in both top and bottom sides of silicon layer, the equivalent refractive index in DSC region is usually smaller than that of conventional single gratings, leading to a lower refractive index contrast with the claddings, which therefore makes the incident light travel easily through the DSC structure and leak into the claddings (into the cover cladding if the DSC grating coupler is configured with backside mirror). Moreover, thinner silicon layer will also limit the etch depth modulation of grating grooves.

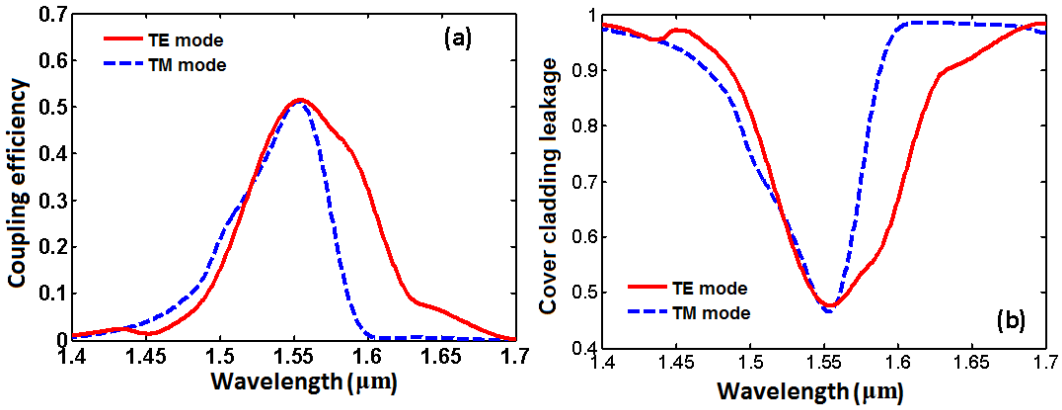

Figure 3.21 (a) The coupling behavior of DSC grating coupler based on 370-nm-silicon layer; (b) The spectrum of the power leakage into the cover cladding layer

As for the 370 nm DSC grating coupler, Figure 3.21(b) shows the spectrum of the power leakage into the cover cladding layer and it can be seen that most of the coupling loss comes from the leakage (If without DBR, the power leakage into substrate is around 60%. This situation gets more serious in thinner silicon layer case). For DSC grating couplers constructed on a thick silicon layer, a properly designed taper between the grating region and external waveguide is required in practical system in order to make the light can be smoothly delivered into the external thinner planar waveguide.

3.5.3 Double channel (DCH) grating couplers based on DSC structure

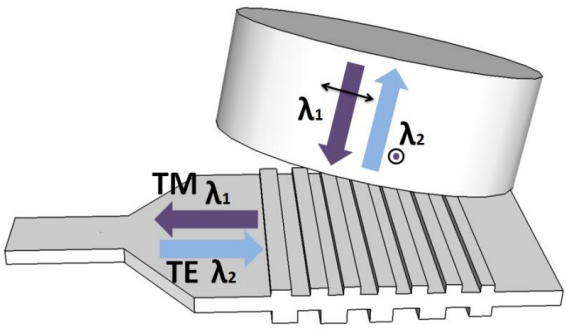

Figure 3.22 Schematic illustration of a DCH grating coupler and its operation principle

DSC structure can be also applied to design double channel (DCH) grating couplers. DCH grating couplers are used to excite the TE and TM modes at two desirable wavelengths (1.31 μm for TE mode and 1.49 μm for TM mode). Figure 3.22 shows the configuration of a DCH grating coupler and its operation principle. As shown in Figure 3.22, the two polarized lights work at different wavelengths with opposite data flow directions in the fiber and on-chip waveguides. The device can be used to duplex the two wavelength channels based on their polarization states. This feature can be applied in fiber to the home (FTTH) optical networks, in which 1.31 μm channel is used to transmit upstream data whereas 1.49 μm channel is used for downstream data. Using the polarization division technology, device footprint can be reduced to half that of previously reported spatially separated duplexer[82]. The design approach of DCH DSC grating couplers is the same as that of POI grating couplers. It should be noted that, now in the sweep step, the target is to make $CE_{TE|1.49} + |\Delta ce_{TE|TM}| + CE_{TM|1.31}$ close to 0, where $CE_{TE|1.49}$ is the coupling efficiency of TE mode at 1.49 μm wavelength, $CE_{TM|1.31}$ is the TM mode coupling efficiency at 1.31 μm wavelength, and $|\Delta ce_{TE|TM}|$ is the difference of coupling efficiency for TE mode excitation at 1.31 μm wavelength and TM mode excitation at 1.49 μm wavelength. The parameters of the designed DCH grating coupler are listed as follows: h_1 = 600nm, d_1 = 80nm, d_2 = 90 nm, Λ_1 = 755 nm with 355 nm unperturbed region and Λ_2 = 760 nm with 400 nm unperturbed region. In this case, no BDR is deployed, and the BOX layer thickness is 2.2 μm.

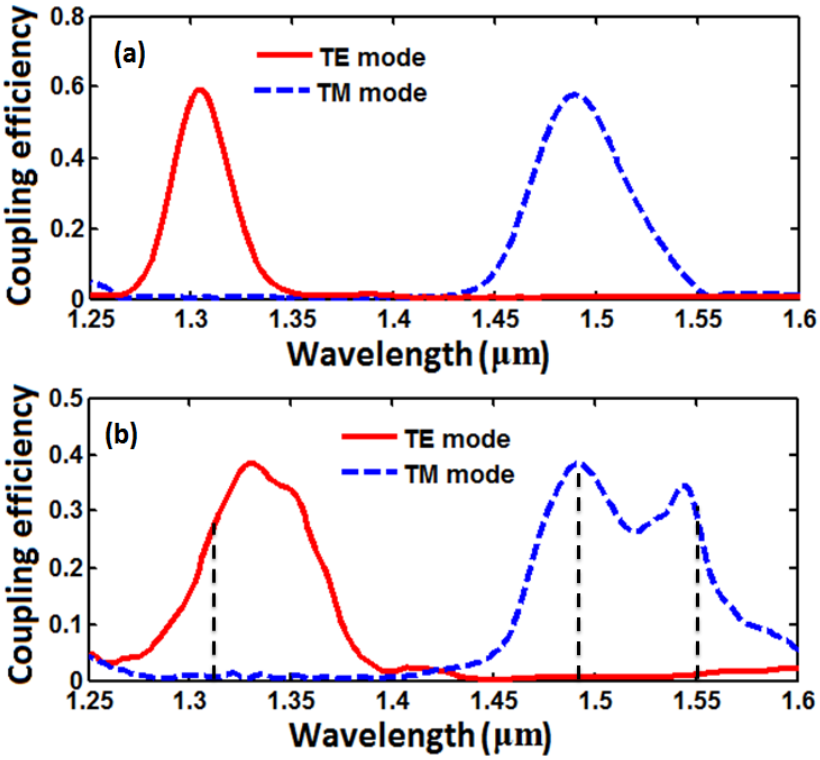

Figure 3.23 Coupling efficiency of the proposed DCH grating coupler for 1.31 μm and 1.49 μm channels. (b) The performance of DCH grating coupler with three channels at 1.31 μm, 1.49 μm and 1.55 μm.

The spectral response of the DCH grating coupler is shown in Figure 3.23(a). It can be seen that the TE mode is excited at 1.31 μm wavelength, and the TM mode is coupled at 1.49 μm. The efficiencies for both TE and TM channels are achieved around 60%, which are better than the spatially-separated DCH duplexer[82]. The 3-dB bandwidth for TE and TM polarizations is about 35 nm and 55 nm, respectively. In practical FTTH networks, because the downstream channel is usually divided into two sub-channels at 1.49 μm (for data) and 1.55 μm (for video), a broader bandwidth (or another resonance peak) around the downstream working wavelength is necessary. Then, we also designed a DSC grating coupler with such behavior as illustrated in Figure 3.23(b). The achievable efficiency for three channels at 1310 nm, 1490 nm and 1550 nm wavelength are 27%, 36% and 31%.

3.6 Vertical coupling for silicon nitride waveguides using silicon grating couplers and transitions – separated design method

In the prior sections, we have proposed several functional grating couplers on silicon waveguides. In this section, we will discuss the grating coupler design for silicon nitride waveguides. Recently, silicon nitride (Si_3N_4) based devices arouse increasing interest. Si_3N_4 has a lower refractive index than silicon. As such, the silicon nitride photonic devices have a lower sensitivity to surface roughness, resulting in better loss performance. They also have higher tolerance to dimensional deviations during fabrication [98]. Furthermore, the temperature coefficient of refractive index for silicon nitride is smaller than that for silicon [74]. Owing to these advantages, various applications have been explored on the silicon nitride platform, such as sensors [99], resonators [54] and optical switching [100] etc. However, conventional design techniques for planar silicon nitride waveguides exhibit low coupling efficiency owing to the fact that the coupler is directly constructed over the Si_3N_4 waveguide. The best reported result for coupling between Si_3N_4 waveguide and standard single-mode fiber is only -3.9 dB and -18 dB for TE and TM mode excitation, respectively [74]. We observed that the problem occurs due to the low refractive index contrast between the silicon nitride grating region and the silica claddings, which causes serious optical leakage into the substrate and limits the coupling performance. In this case, the efficiency is hard to improve if the grating design is constrained to the same material and structure as the target Si_3N_4 waveguide. Here we propose a new approach to enable the design of grating couplers which are not constrained by the target waveguide. The approach will enable design flexibility and makes it possible to reuse the existing optimized designs on silicon photonics platform [7]. Combined with the design principle stated in [77], the approach also enables the correction of the

coupling bandwidth behavior which cannot be optimized using conventional design techniques. Based on the idea, two kinds of optimized grating couplers, a silicon grating coupler and a horizontal slot waveguide based coupler, are applied for TE and TM mode coupling from fiber to silicon nitride waveguides. By introducing a proper transition section and not involving much extra design and fabrication complexities, the two grating couplers can achieve coupling efficiency of more than 55%. The fabrication issues in practical systems are also discussed.

3.6.1 The efficiency issues for fiber to silicon nitride waveguide excitation

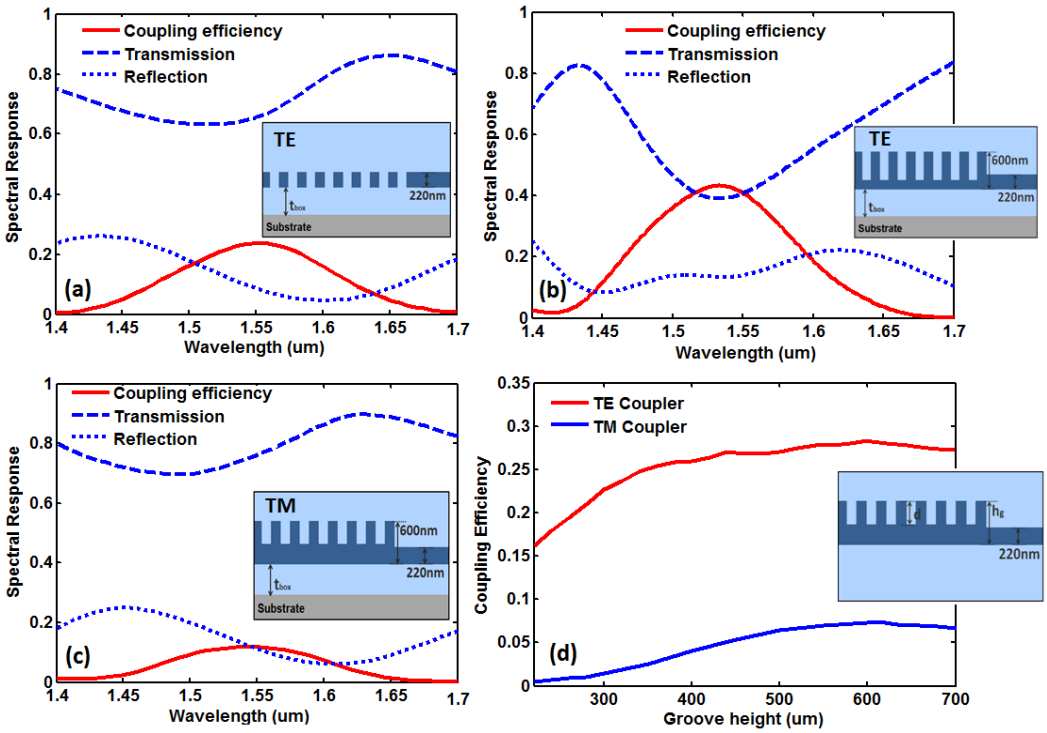

Figure 3.24 (a) Spectral response of 220 nm height silicon nitride grating coupler for TE mode excitation; (b) Spectral response of 600 nm-height silicon nitride grating coupler for TE mode excitation; (c) Spectral response of 600 nm height silicon nitride grating coupler for TM mode excitation; (d) The coupling efficiency at different groove height for TE and TM mode excitation.

We first give a theoretical discussion on the efficiency issues of grating couplers over silicon nitride waveguides, and here we also propose several possible solutions. In a practical structure, the silicon nitride waveguide is sitting on a Si substrate with a buried oxide layer and covered with silicon oxide upper cladding. The refractive indices of silicon nitride and SiO_2 are 2.0 and 1.45, respectively. The light is injected to the grating surface at 8^{o} incident angle, and the beam has 10.4 μm mode width between $1/e^2$ points of the power.

The coupling performance of several typical silicon nitride grating couplers with uniform grating grooves are shown in Figure 3.24. These results are calculated using Lumerical FDTD Solutions[2]. Figure 3.24 (a) illustrates a 220 nm height TE grating coupler and its coupling performance. The optimum efficiency is achieved when the grating is fully etched, and the maximum efficiency is 24% when the BOX layer thickness is optimized to 2.2 μm. It can be seen that most of light passes through the grating structure and leaks into the substrate. Selecting a proper groove height in the grating region can increase the coupling efficiency [77]. In Figure 3.24 (b), the optimized TE grating coupler has 600 nm height with 480 nm etching grooves. The coupling efficiency increases to 44% while the BOX layer thickness is tuned to 2.5 μm. The transmission leakage is still the major loss contributor. For the TM grating coupler, the 220 nm-height grating coupler exhibits nearly zero optical coupling into the target waveguide. By raising the grating height to 600 nm shown in Figure 3.24 (c), the achievable efficiency is 16%. The transmission leakage takes away more than 70% of the energy in a wide spectral window. As for more general cases, Figure 3.24 (d) shows the achievable coupling efficiency by optimizing the etch depth at different groove heights for TE and TM grating couplers (Here, we just investigate the intrinsic property of the grating coupler in relation to groove height, which is the dominant factor affecting the coupling behavior. Substrate interference effects are ignored.). It

can be seen that the coupling efficiencies are always at a low level. The problem occurs due to the low refractive index contrast between the silicon nitride grating region and the silica cladding, and typically exists in low refractive index contrast waveguide grating couplers.

In order to solve the problem, we have considered two approaches to modify the grating structure. The first approach is to add a high refractive index overlay (such as silicon overlay) on top of the silicon nitride waveguide in the grating region to prevent the transmission leakage. In this approach, the fiber beam is first injected into the high-refractive index overlay and then coupled into the silicon nitride waveguide via a transition taper. The disadvantages of this approach are the grating coupler and the transition taper need to be optimized to minimize the coupling loss, and that may increase the design complexity. It also lacks design flexibilities to some degree. The second approach is to use a separate grating coupler which is completely independent to the target silicon nitride waveguide, for example, using a silicon grating coupler for fiber to Si_3N_4 waveguide excitation. This approach allows reuse of the optimized grating design and we only need to optimize the transition section. The approach will be discussed in detail in the later section.

In addition, we have also considered the approach of modifying the external layers to control the transmission leakage such as adding a backside metallic mirror or a distributed Bragg reflector (DBR). For the TE grating coupler, this approach can realize over 60% coupling efficiency with proper backside mirror or reflector design. However, for the TM grating coupler, the coupling efficiency is still low at around 20%. Moreover, the major problem is that the fabrication of DBR and metallic mirror involves sophisticated processes at the backside of the wafer [101], which affects manufacturability. Thus, we give a prior consideration to the separate design method.

3.6.2 Separate TE and TM grating couplers design

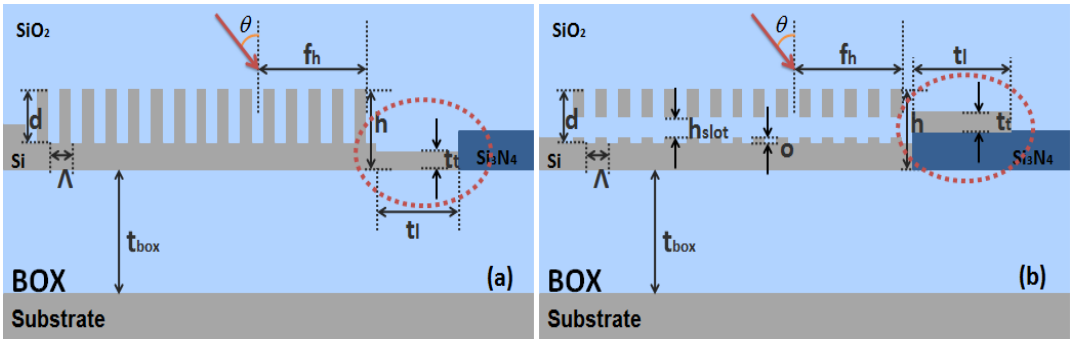

Figure 3.25 The structure and main parameters of separate grating couplers for fiber to silicon nitride waveguide for (a) TE mode excitation and (b) TM mode excitation.

We designed two grating couplers (illustrated in Figure 3.25) for TE and TM excitation, respectively. Figure 3.25 (a) gives the silicon grating coupler structure with its main parameters for TE excitation. Figure 3.25 (b) shows the horizontal slot (H-slot) waveguide based grating coupler for TM excitation. Owing to the reusability brought by separate coupler designs, both couplers directly refer to the optimized parameters in previous works. For the silicon grating coupler in Figure 3.25 (a), we basically adopt the coupler design with a poly-silicon overlay proposed in [70], [102]. Since our grating coupler has a silica cover rather than air cladding as in [70], [102], the grating parameters are correspondingly modified. Using the method described in [77], it is easy to obtain the optimized grating parameters: the groove height h is 430 nm, the etch depth d is 190 nm, the grating period is 606 nm (filling factor = 50%), and the best BOX layer thickness is tuned to 2.3 μm. For the H-slot waveguide based grating coupler, we use the same parameters as the design in section 3.4. In the grating region, the slot height h_{slot} is 50 nm, the groove height h is 595 nm, the etch depth d is 420 nm (over-etch depth o = 30 nm), the grating period is 814 nm (filling factor = 50%) and here we tune the BOX layer thickness to 2.5 μm for constructive

interference. Both the grating couplers are operating at 1.55 μm telecommunication wavelength at 8 ° fiber incident angle. Since the structure and materials applied in the grating region are different from the targeted waveguide, the direct coupling from grating region to the waveguide may cause mode mismatch (or reflection) and then induce losses. Hence, a proper transition section needs to be designed to bridge both parts. In our model, the transition sections are marked in the dotted cycles in Figure 3.25. Here, we select a simple structure as the transition section for easy fabrication consideration. For the silicon grating coupler, the transition section is a short piece of silicon waveguide with transition length t_l and height t_t being the two main parameters affecting the loss behavior. As for the H-slot waveguide grating coupler, we simply deposit a thin silicon film over a short silicon nitride waveguide as the transition section (shown in Figure 3.25). Likewise, both the length t_l and height t_t of the deposited film need to be optimized for a low loss mode transition. We sweep both dimensions of t_l and t_t for the optimum coupling in our calculations and show the corresponding coupling efficiencies in Figure 3.26. The result for the silicon grating coupler is shown in Figure 3.26 (a), which indicates that good coupling efficiency and tolerance can be achieved when t_l and t_t are configured to 1.02 μm and 0.2 μm, respectively. Likewise, Figure 3.26 (b) illustrates the result for the H-slot waveguide based coupler. In this case, we can set the layer of silicon film with 1.8 μm in length and 80 nm in height for good coupling performance and tolerance. It is obvious that the design and optimisation of the transition section only involves two parameters, which is much simpler than the grating coupler design which usually involves a sophisticated multi-parameter optimisation procedure.

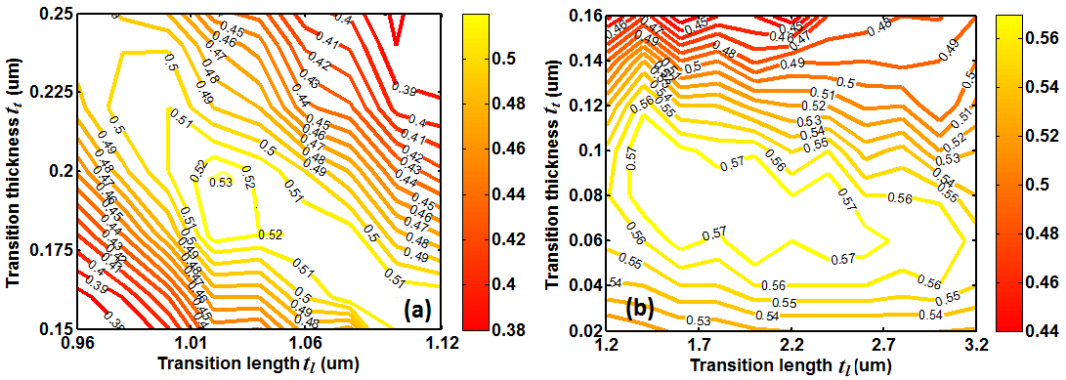

Figure 3.26 The optimisation of the transition section between silicon nitride waveguide and both the grating couplers for (a) TE mode excitation and (b) TM mode excitation

Figure 3.27 (a) gives the spectral response of the silicon grating coupler for fiber to silicon nitride waveguide TE mode excitation. We can see that a peak efficiency of 55% is achieved. Compared to the results in Figure 3.24 (a) and (b), the transmission spectral response has dropped to below 25% around the resonant wavelength at 1.55 um. Figure 3.27 (b) shows the spectral response of the H-slot waveguide based grating coupler for fiber to silicon nitride waveguide TM mode excitation. The peak coupling efficiency is close to 60%. The coupling performance is largely enhanced compared with the result of 16% in Figure 3.24 (c). The transmission spectrum is well-controlled and has a flat response around the resonant wavelength. The percentage transmission is below 20%.

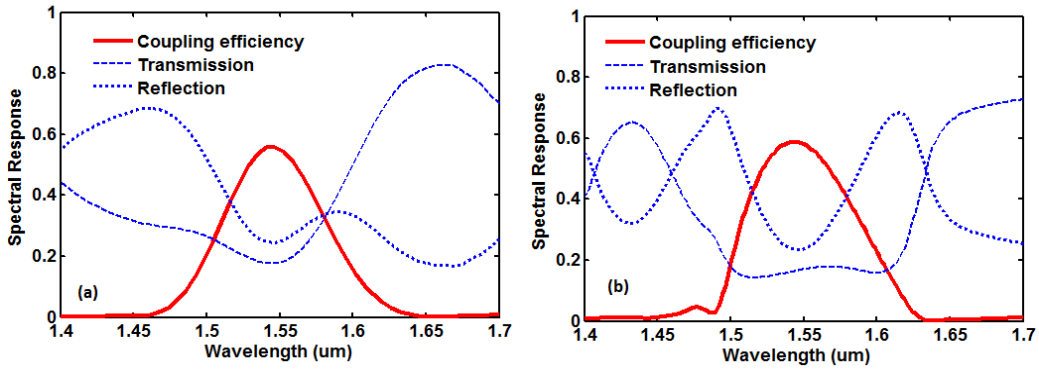

Figure 3.27 Spectral response of both the grating couplers for (a) TE mode excitation and (b) TM mode excitation

Sensitivity to fabrication and alignment tolerances of both couplers was also analyzed. To study fabrication tolerances, simulations were performed with different filling factors as well as different etch depths for both TE and TM mode grating couplers. Figure 3.28 (a) shows coupling efficiency results when varying these parameters for the TE mode grating coupler. It is observed that the coupling efficiency is almost constant (below 1 dB drop) for etch depth variations from 175 nm to 200 nm or for filling factor changes of more than 5%. To study alignment tolerances, the incident angles as well as the horizontal fiber positions were varied. Figure 3.28 (b) shows coupling efficiency results when varying those parameters. High coupling efficiency is maintained for tilt angle variations of 4 °from 6 °to 10 °or horizontal fiber position changes of 5 μm.

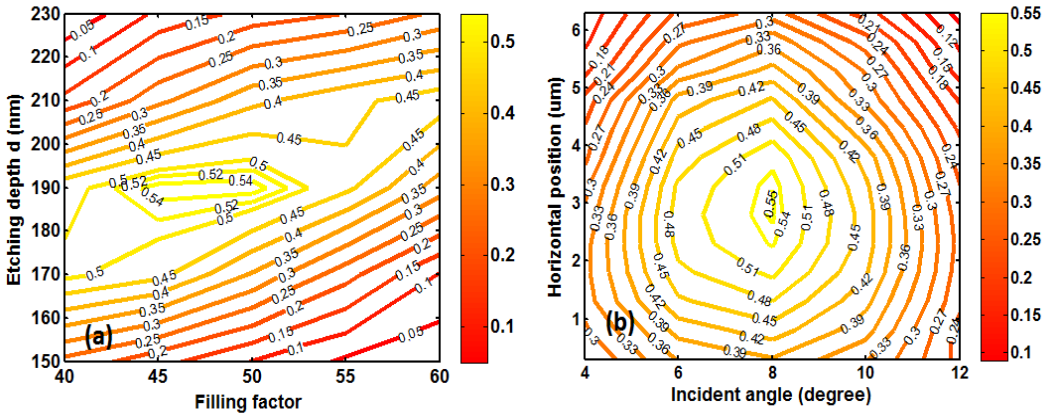

Figure 3.28 (a) Fabrication tolerance and (b) operation tolerance for the silicon TE mode grating couplers with a transition section.

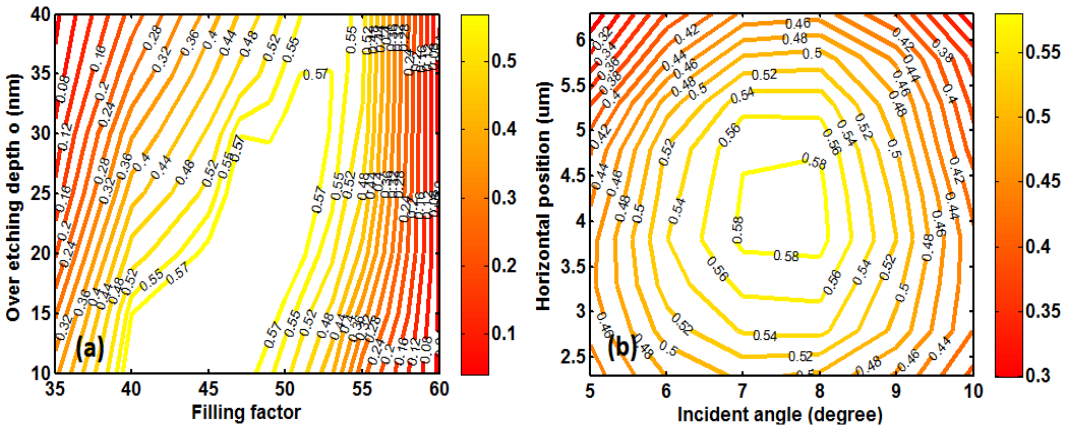

Figure 3.29 (a) Fabrication tolerance and (b) operation tolerance for the H-slot structure based TM mode grating couplers with a transition section.

Likewise, Figure 3.29 (a) shows coupling efficiency results when varying filling factor and over-etch depth for the TM mode grating coupler. It is observed that the coupling efficiency is almost constant (below 1 dB drop) for over-etch depth variations from 10 nm to 40 nm or for filling factor changes of more than 5%. For alignment tolerances, Figure 3.29 (b) shows the coupling efficiency results when varying the incident angle and the horizontal position of the fiber. High coupling efficiency is also maintained for tilt angle variations from 6 ° to 9 ° or for horizontal fiber position changes of 3 μm.

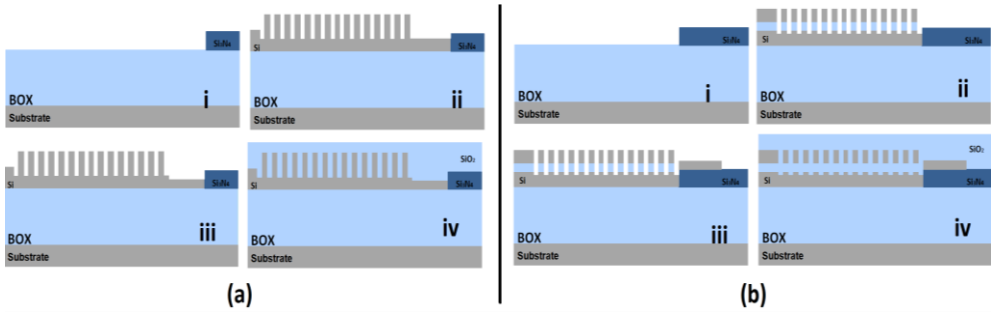

Figure 3.30 Simplified fabrication process flow for both the silicon waveguide based grating coupler and the H-slot structure based coupler, each with a transition section

The fabrication process of both grating couplers is shown in Figure 3.30. The general steps are listed as follows: first, a window is opened for the grating coupler; this is then followed by material deposition and masked etch-back to form the unpatterned grating region, and then by etching process to fabricate the grating grooves; next, the transition section is fabricated by a dry etching process (for TE coupler) or deposition process and masked etch-back (for TM coupler); finally, the structure is covered with the top oxide cladding. We can see that, compared with the typical coupler design with an overlay (to optimize the groove height), only step-i and step-iii are additional fabrication processes. Figure 3.26 indicates that the designed transition sections in both cases have good fabrication tolerance. It can also be seen that the coupling efficiencies are maintained at a high level for both the grating couplers even without the process of step-iii (i.e. t_t = 0.24 μm for TE coupler and t_t = 0 μm for TM coupler). As such, the separate grating coupler design would not introduce much extra fabrication complexities in practical systems.

3.7 Experimental demonstration of single port and multiport grating couplers

In this section, we discuss the experimental demonstration of single port grating coupler for single fiber excitation and multi-port grating array for the fiber array inputs. This work is also a preparation for the integrated microwave project presented in Chapter 6. Here, we first introduce the grating design and its parameters. The grating coupler is designed on 300 nm silicon platform as it is also the platform to fabricate our microwave filters in Chapter 6. A simple uniform grating structure with 50% filling factor is used in our design, and for this structure, only one round of etch process is required for the fabrication. According to our FDTD calculation, the simple

design on 300 nm silicon platform can achieve a satisfying coupling efficiency for practical applications. The structure and parameters are shown in Figure 3.31(a). Using the aforementioned design rules, the corresponding optimized parameters are listed as follows: grating period is 600 nm, etch depth is 120 nm and the BOX layer is 3 μm. The microscope photo graph of the fabricated grating coupler is illustrated in Figure 3.31(b). We characterize the coupling performance of the grating coupler, and both the simulation and experiment results are illustrated in Figure 3.32. It can been seen that the maximum theoretical coupling efficiency is about -2.2 dB and the maximum measured coupling efficiency is around -3.5 dB. The difference between the theoretical and experimental result mainly comes from the fabrication variations and operation limitations.

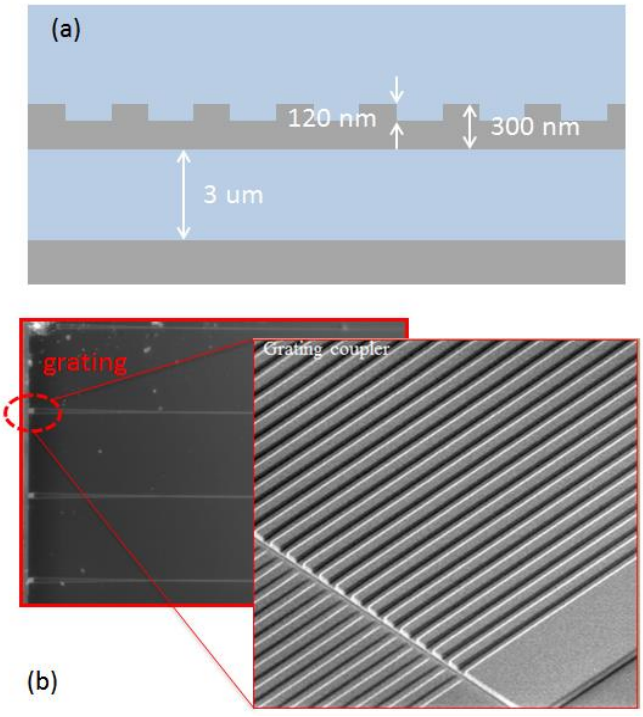

Figure 3.31 (a) The grating coupler structures with optimized parameters; (b) The microscope photo graph of the fabricated grating coupler.

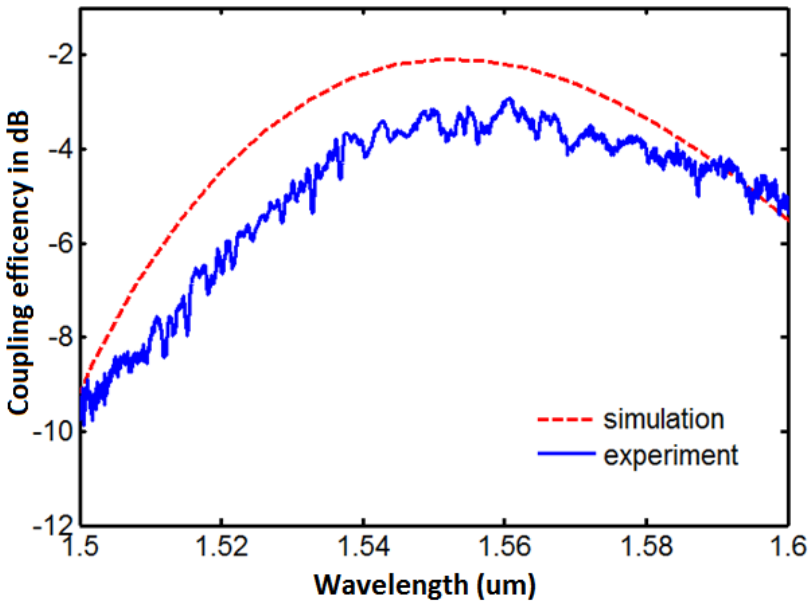

Figure 3.32 Simulation and measurement results of the grating coupler for single port input.

Then, we consider the case that using fiber array aligned with grating array to achieve multi-port excitations. Each grating coupler interface is the same as the grating coupler used in the above single input case.

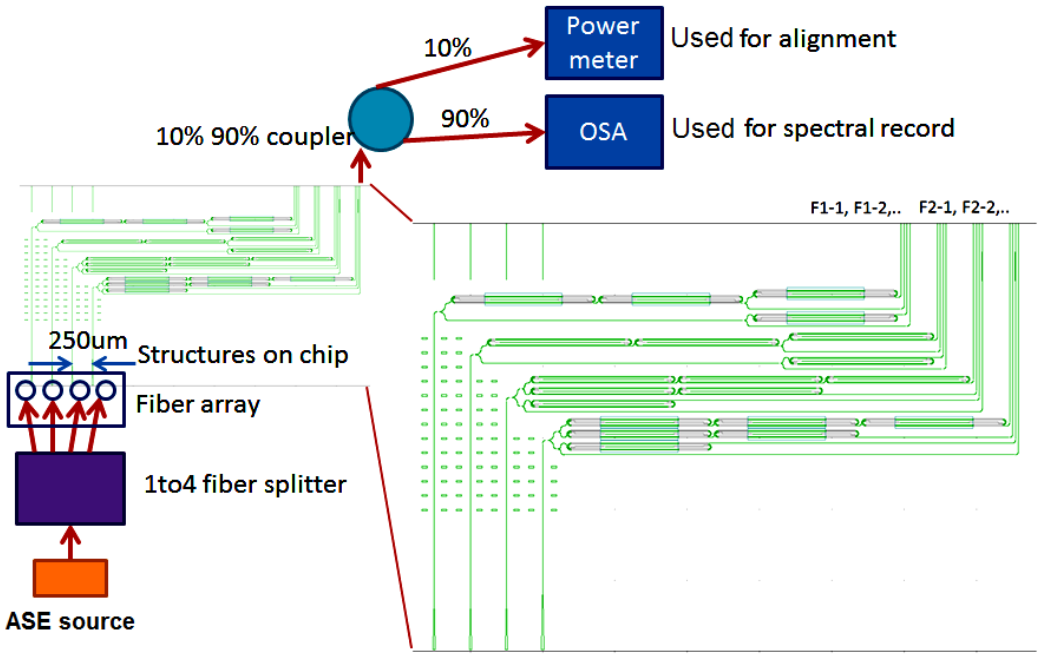

Figure 3.33 The structure mask layout and the measurement schema

The measurement setup illustration and the mask layout of to-be-measured structure are shown in Figure 3.33. The optical power comes out from the amplified spontaneous emission (ASE) laser source and enters a 1-by-4 off-chip splitter. Each channel output of the splitter is connected with one input of a 4 fiber array. The fiber interval of 250 μm in the fiber array is the same as the spacing between gratings fabricated on the chip. Through the grating arrays, the power is coupled into silicon waveguides on the chip. Each input grating channel will then split up into 4 channels and then forms 16 channels on chip. For each channel, different units of delay line are added to induce different group delays. At the end of the waveguide output, we use an inverse taper as horizontal coupling interface and the output power is finally collected by a lensed fiber. This work is an experimental preparation for the integrated microwave project presented in Chapter 6. The delay lines are included since we have the similar configuration and layout for the integrated microwave filter design. The measurement work has two main purposes: one is to make sure that the fiber array to grating array alignment can work properly, and the optical power can be coupled from fiber to chip; the other purpose is to do preliminary component integration and to confirm that the system loss is in an acceptable range.

The holder, input fiber array and the output port are shown in Figure 3.34. The holder can adjust the displacement in *x*, *y* and *z* axis as well as the angle in *x*-*y* plane and *x*-*z* plane. Compared with the alignment holder used by IMEC [103] who pioneers the grating coupler based multi-port excitation works, our alignment instruments are much simpler. In our measurement, we also find that there is enough operation tolerance for alignment between grating array and fiber array to achieve reasonable results.

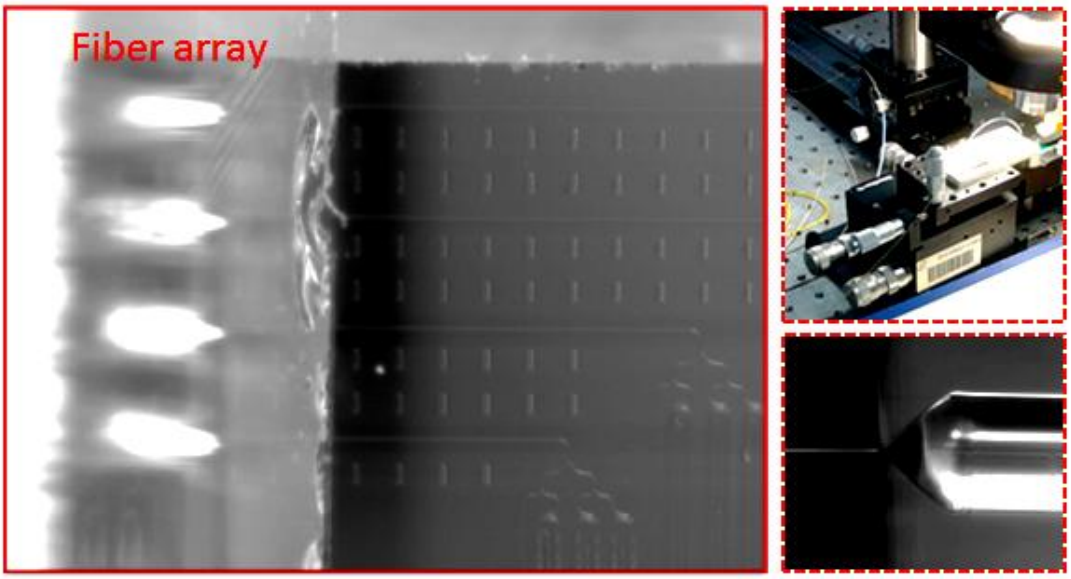

Figure 3.34 Fiber array holder illustration; multi-port grating array aligned with fiber array inputs and the collection lensed fiber under the microscope

Before the measurement, we first make a power budget calculation for this system. Each branch loss includes: TM elimination loss (3 dB), 1-to-4 fiber beam splitter loss including power splitting and coupler excess loss (8 dB), power splitting of Y splitter (6 dB) grating coupler loss (3.5 dB), inverse taper loss (3.5 dB), waveguide loss excluding the delay line unit (2 dB), connectors loss (0.5 dB), and 90% fiber coupler loss (0.5 dB). Thus, each branch loss is around 30 dB. The power budget doesn't provide exactly accurate loss values since the loss estimations are roughly based on measurement of individual components, e.g. the 3.5 dB loss of grating coupler which refers to single fiber to chip coupling, may increase in the case of multi-port coupling using fiber array. However, the power budget provides an expected reference for measurement results to verify whether the results are in a reasonable range.

The measurement results for each channel output are illustrated in the following group of figures - Figure 3.35 to Figure 3.38. Figure 3.35 shows the measurement results for port F11 to F14. It can be seen that, for the branch without delay line unit, the

insertion loss is around 30 dB which is consistent with our power budget prediction. For other branches, the loss increases due to the delay line units involved. Likewise, the analysis is the same for other group of channels. The fluctuations and fringes appearing in the spectrum are introduced by Y-splitters in the on-chip structure since high order modes are excited and intermodal coupling occurs at the imperfectly fabricated branch tip due to limited etching resolution. As for the fringes, a detailed discussion about this phenomenon is given in Chapter 5.

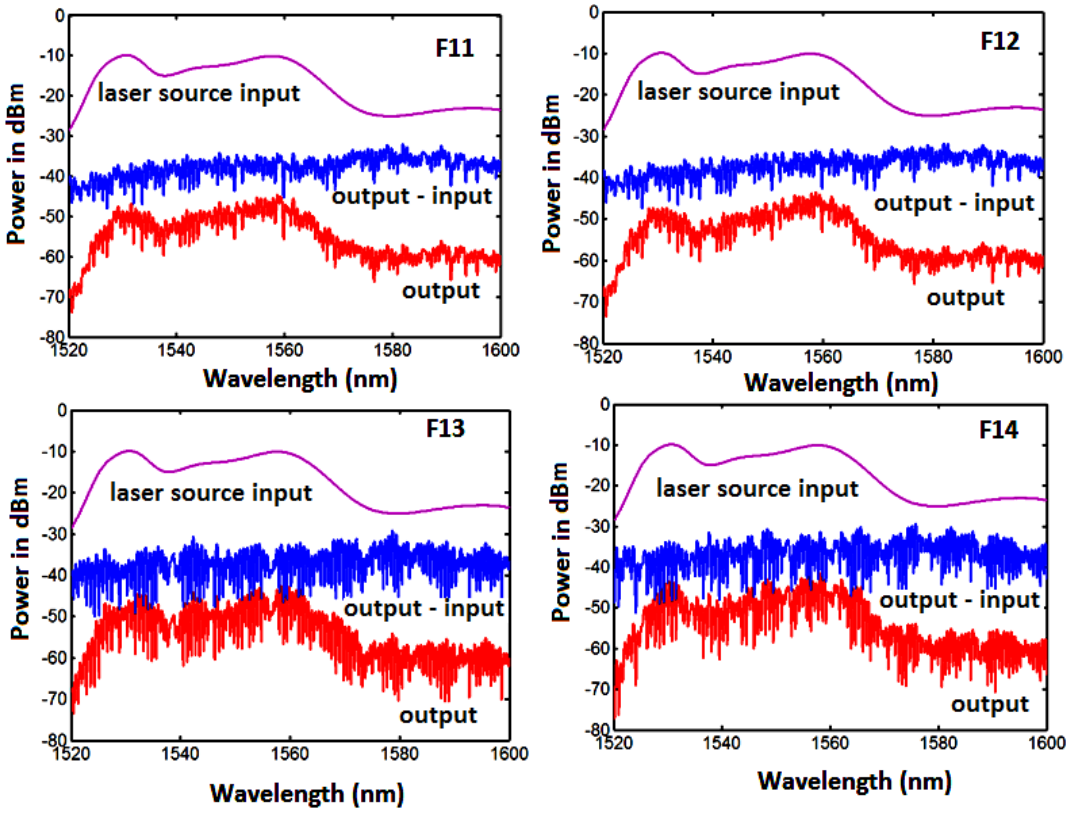

Figure 3.35 Measurement results for port F11 to F14.

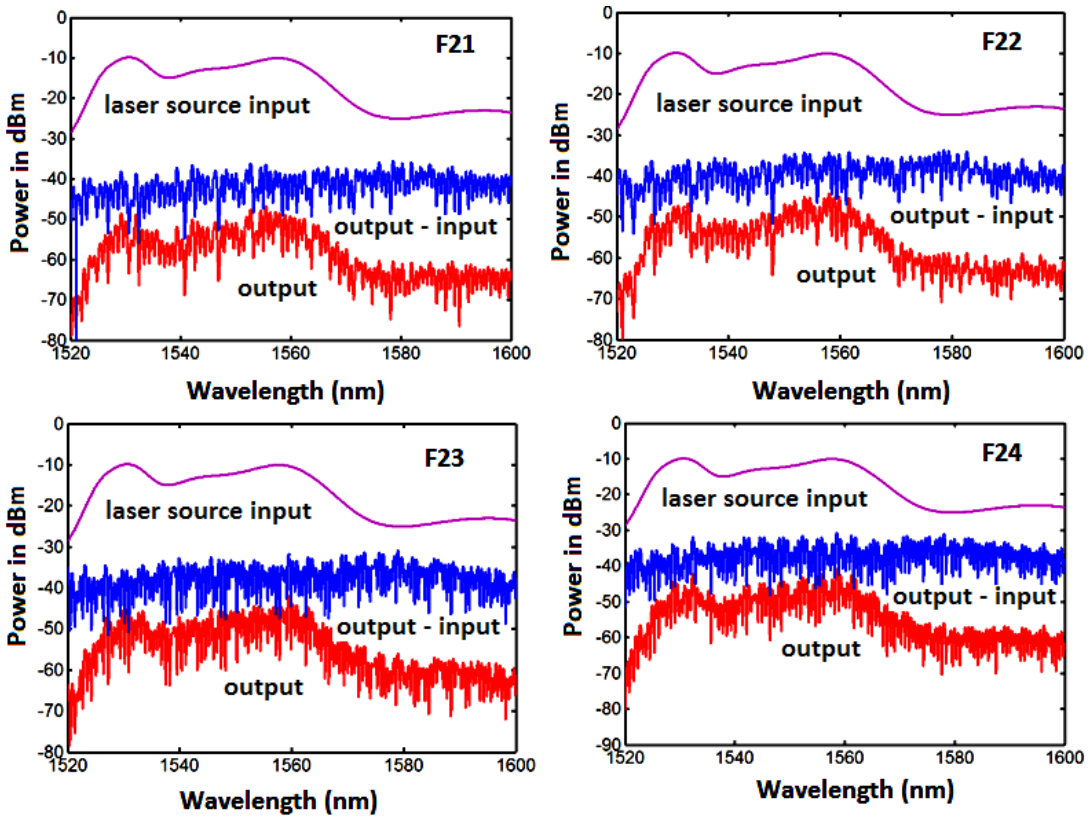

Figure 3.36 Measurement results for port F21 to F24.

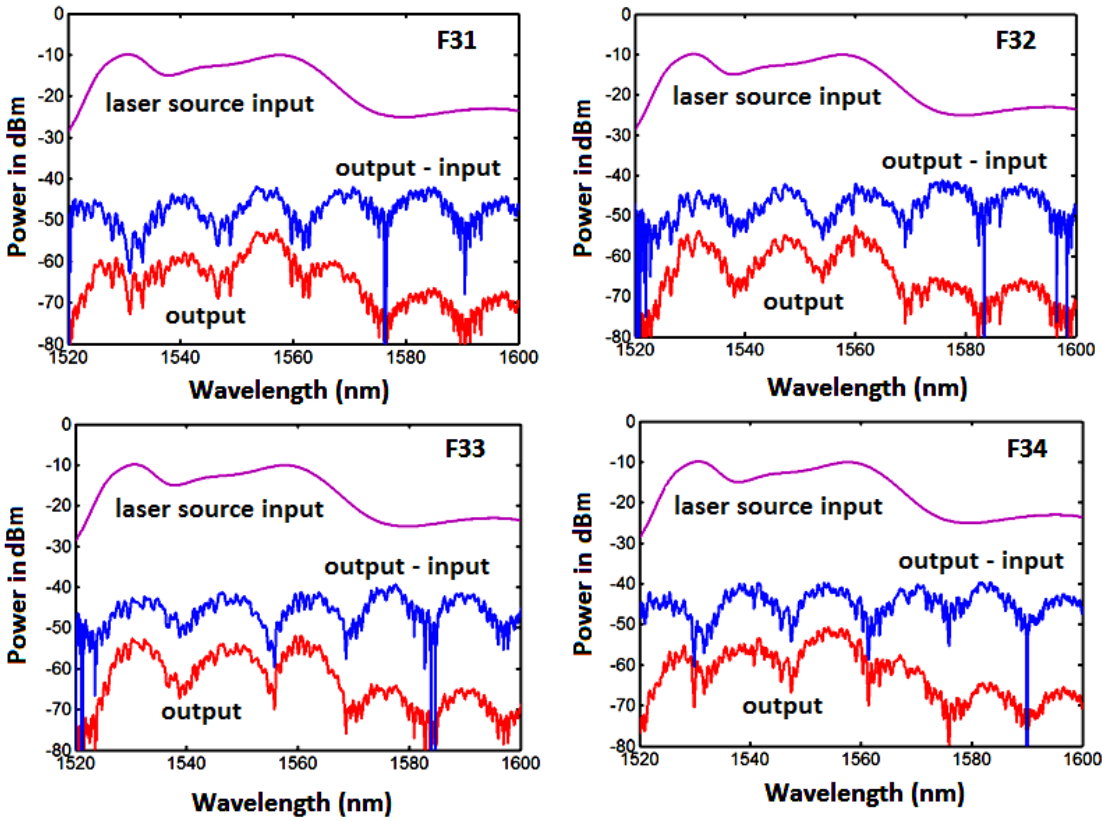

Figure 3.37 Measurement results for port F31 to F34.

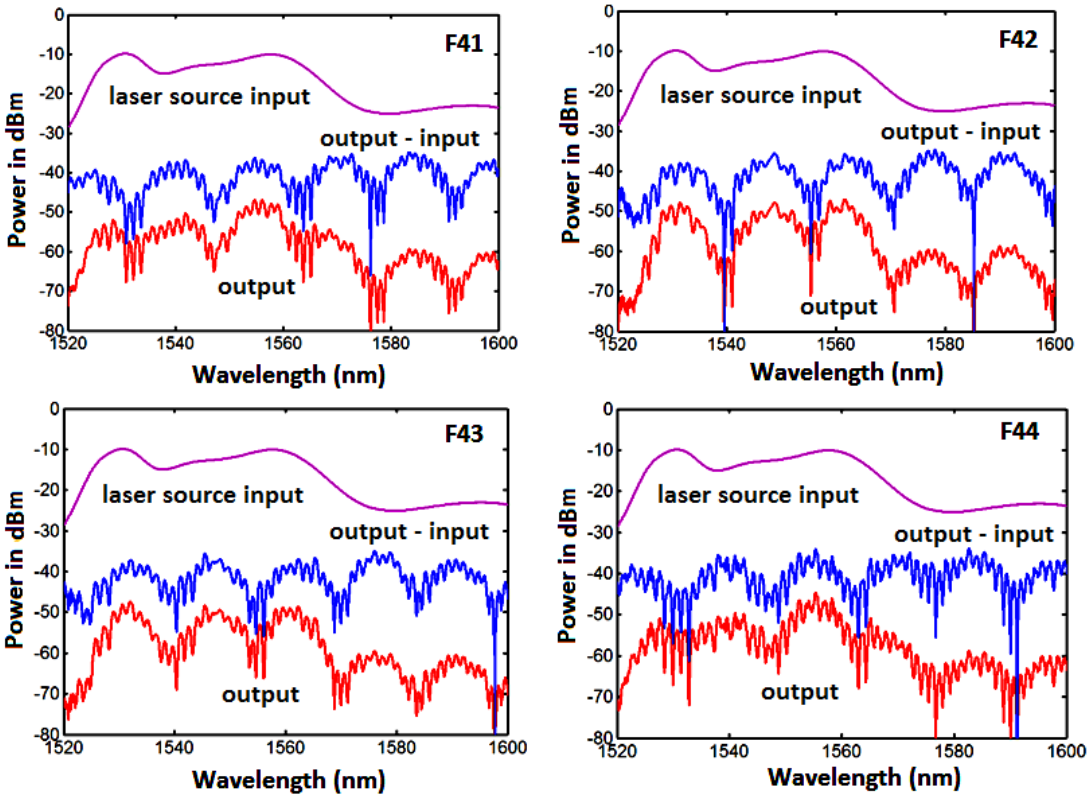

Figure 3.38 Measurement results for port F41 to F44.

At the end of this section, we summarize the alignment experience obtained for multiport input case as follows: (a) For the mask design, we should consider adding the necessary marks for alignment, the long waveguide itself can be good reference for alignment. (b) Because the microscope may not be perfectly vertically positioned, so there likely exists some displacement between the real position and the image shown by the microscope. To slowly adjust the fiber array around the target position is always a good idea. (c) It is easier to get a clear image of the fiber cores under the microscope if selecting the input fiber array with thinner plastic wrap and in this case, the feedback obtained from microscope is more accurate. (d) During the operation, it is required to first tune the angle to make the line of fiber array cores parallel with the line of the grating array, and then to do the *x*-*y*-*z* axis adjustment. The fibers in the center will usually get signal first. After a signal is obtained, one then needs to fine tune the angle and displacement to make the best coupling efficiency for all ports. (e)

The first time to do the alignment usually takes much longer time. To record the obtained alignment position under the microscope enables later alignments to be much easier and the signals can be normally obtained in minutes.

3.8 Summary

In summary of this Chapter, we have derived a bandwidth formula for planar waveguide grating couplers. The coupling bandwidth is determined by the intrinsic properties of the grating coupler and is also affected by the fiber parameters such as position and beam width etc. We investigated the effect of individual parameter on bandwidth behavior and obtained some intuitive vision on the bandwidth performance of grating couplers.

Based on the grating coupler bandwidth discussion in this Chapter, we summarize and list some useful guidelines for grating coupler design and fiber operation for broad bandwidth performance as follows: Firstly, in order to design wideband grating coupler, we should attempt to make the grating pitch as large as possible by decreasing the refractive index of the grating area. This can be achieved by adopting relatively low refractive index materials (silicon nitride) or through perturbation of the grating groove in lateral direction or using refractive index engineering structures etc. However, in view of the coupling efficiency, to decrease the refractive index of the grating area normally leads to a lower refractive index contrast with the claddings in the grating region, which therefore makes it easy for the incident light to travel through the structure and leak into the claddings. Hence, with this approach, we should consider controlling the power leakage to the claddings during the design. Secondly, according to the bandwidth formula, to properly design the grating structure (or choose special materials) of smaller dispersion can also increase the coupling

bandwidth. As for the fiber operation, the basic idea of broadening the coupling bandwidth is to reduce the effective interaction grating area. This can be achieved by putting the fiber closer to the grating start or using a fiber with smaller beam width or a larger numerical aperture. To optimize the beam size (or numerical aperture) is a better approach to increase bandwidth because it would not induce great efficiency drop (if the beam size is not greatly reduced).

Besides, we proposed a method by separating optimisation parameters in a sequence of individual steps to simplify the optimisation process for grating couplers. The optimisation approach works without a time-consuming scanning process to solve the multi-parameter optimisation problem existing in the grating coupler design, which greatly reduces the design complexity. We applied the design principles and achieved a broadband and high-efficiency horizontal slot waveguide grating coupler.

In addition, the DSC based grating couplers were proposed to simultaneously adjust both the TE and TM mode excitation. Based on the structure, we designed a polarization insensitive grating coupler with good performance. The DSC structure has already been proven to be feasible for fabrication [97]. It may have wide applications in practical systems such as double-channel communication and FTTH networks.

Furthermore, we offered a solution for the loss efficiency issue of fiber to silicon nitride waveguide mode excitation via a grating coupler. To achieve high coupling efficiency, we proposed a separate coupler design, which is not constrained by the external waveguide material or structure, offering design flexibility and reusability. Two kinds of optimized grating couplers, one silicon grating coupler and a horizontal slot waveguide based coupler, were designed for TE and TM mode excitation,

respectively. By introducing a proper transition section without adding extra design and fabrication complexity, coupling efficiencies of more than 55% were achieved for both polarizations. Both the couplers also have good fabrication and operation tolerances.

Chapter 4 LOW LOSS SILICON WAVEGUIDE AND DELAY LINE DESIGN

4.1 Introduction

Optical delay lines are one of critical functional components in photonic systems. They are able to adjust the time and phase properties of signals through introducing proper optical delay and is essential for various applications such as flip-flop memory [104], optical buffers [52] and interferometer [105] etc. Due to its critical role in optical communication systems, on-chip tunable delay lines have been widely investigated, and various approaches such as nonlinear phenomena [106], [107] and microring resonators [108] etc. are applied to achieve tunable optical delay. The challenges lie in the fact that tunable delay lines normally work with relatively narrow operation bandwidth and large excess loss, and they also require large device size or high fabrication precision [109]. Recently, H. Lee *et al*. demonstrated on-chip 27 meter ultra-low loss delay lines based on special waveguides of wedge geometry cross-section with smooth edges using optimized fabrication [31], which reveals the potential for ultra-long delay on integrated photonic platform. Routine silicon waveguide based passive delay lines with desirable delay are significant for many practical applications. They have the advantages of wide bandwidth, being easy-to-integrate, handling compact footprint and stable performance. Combined with thermo-optic switches or attenuators, passive delay lines are able to achieve the functions of digital delay lines or microwave filters etc. Low loss and precise group delay are two straightforward targets for design of passive silicon delay line. Many factors are involved in the design and optimisation such as group velocity of the waveguide

structure, waveguide crosstalk isolation, and delay unit layout arrangement and so on. In this Chapter, by taking all these factors into account, we report a complete design and characterization process for passive delay lines. Several 50 ps delay line units are designed and demonstrated on a 300 nm silicon platform for the first time. 50 ps delay are selected for our design since this work is also an experimental preparation for the integrated microwave project presented in Chapter 6, since the same configuration are adopted for the integrated microwave filter design. 300 nm silicon waveguides have better polarization insensitivity. Besides, as compared with 220 nm platform, we have already known that high efficiency grating couplers are more easily realized on 300 nm platform by single-etching fabrication process according to the discussion in Chapter 3. However, 300 nm waveguides usually have larger roughness sidewall boundaries (compared with 220 nm silicon waveguides), making it challenging to achieve low propagation loss. By decreasing the optical intensity on the sidewall boundary through an increased large core-size silicon waveguide with a width of 3 μm, loss below 0.1 dB/cm has been demonstrated on a 300 nm platform lately [28]. Here, we design two types of compact rib waveguides on a 300 nm platform for delay unit fabrication. By properly reducing the rib etch depth (i.e. reducing roughness sidewall area), a low propagation loss of ~ 0.1 dB/cm is realized in one of them. For the whole delay line structure, the hybrid waveguide schema [110], [111] is adopted for the layout design. We use the low loss rib waveguides for all the straight optical paths and quasi-single mode waveguides for the bend paths to guarantee that only the fundamental mode is excited and traveling in the structure. The delay is properly designed through choosing the correct length for each section of the waveguides. We characterize both the loss and delay performance of the proposed delay line units. The measurement results show that the excess loss of ~ 0.7 dB per delay unit with a broadband operation is achievable for the desirable 50 ps delay. The loss can be

further optimized by decreasing the delay line tracks and bend sections. We measure a series of fabricated delay line samples from two batches of wafers, and observe that the delay variation is within 3 ps.

4.2 Low loss silicon waveguide design method

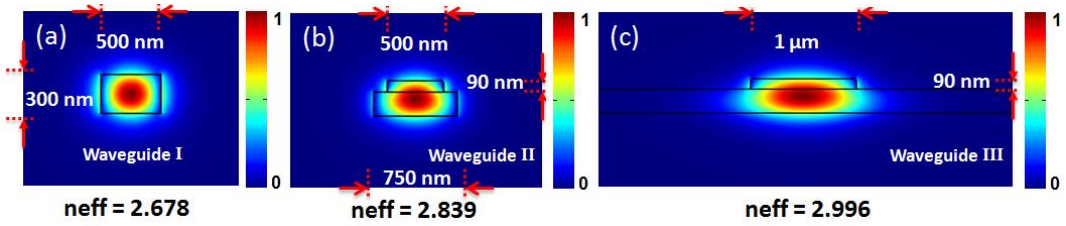

Figure 4.1 *x* component of E-field in the proposed strip and rib waveguides.

In order to design low loss delay line, the first step is to design low loss waveguides. In our schema, we use three types of silicon waveguides to compose the delay line unit. The optical field distributions in these waveguides are illustrated in Figure 4.1, the structure dimension parameters and corresponding effective index of fundamental guided mode are also indicated for λ=1.55 μm. Figure 4.1 (a) is a 500 nm × 300 nm strip waveguide (named by waveguide I) which is used for the bend section; Figure 4.1 (b) is a rib waveguide (waveguide II) with two etching steps, the top step has rib width of 500 nm and bottom step has width of 750 nm; Figure 4.1 (c) is also a rib waveguide (waveguide III) but it has wider rib width of 1 μm at top step and its bottom step has no etching sidewall inside the mode field reachable range (i.e. the sidewall boundary is far away enough and has little effect on the mode field). Since it is difficult to achieve pure single guided mode in 300 nm silicon waveguides, we determine the waveguide dimension parameters mainly according to the following two principles: firstly, the fundamental mode should be well-confined and have a low loss performance; secondly, the waveguide dimensions are optimized to make the

high order modes weakly-confined and lossy in order to avoid their effects on the delay behavior. On 300 nm platform, we choose 500 nm wide trip waveguide. Through numerical simulations using Lumerical mode solutions[3], 90 nm etch depth is selected for rib waveguides. Here we take waveguide III as an example to explain how we determine the etch depth. For waveguide III, the mode fields of the supported fundamental TE_{00} mode and TE_{01} mode are illustrated in Figure 4.2. Here, TE_{mn} stands for the TE mode with field distribution which has *m* "field zeros" in the *y* direction and *n* "field zeros" in *x* direction. Based on our design principle, the target is to keep TE_{00} mode with low loss performance TE_{01} mode leaky and lossy.

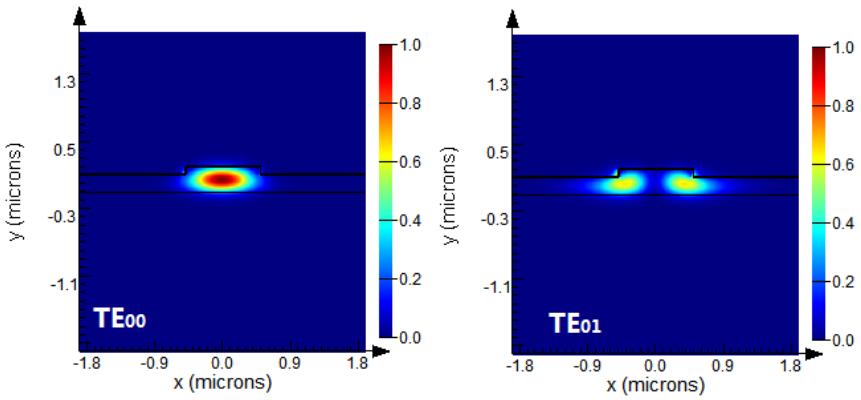

Figure 4.2. TE_{00} and TE_{01} mode field

We observe that both TE_{00} and TE_{01} mode confinement gets weaker when the etch depth decreases, and thus the loss increases accordingly. An intuitive illustration of the confined TE_{01} mode is shown in Figure 4.3 for different etch depth configurations. It can be seen that mode is extended out the physical size of the waveguide rib, and the mode extension get larger while the etch depth decreases. The relationship of loss performance versus etch depth for TE_{00} and TE_{01} mode is illustrated in Figure 4.4. For TE_{00} mode, the loss increases slowly while the etch depth changes from 120 nm to 90 nm, and while the etch depth gets less than 90 nm, the loss increases greatly. Besides,

for 90 nm etch depth, the TE_{01} mode becomes very lossy. Thus, we select 90 nm as our design value for etch depth.

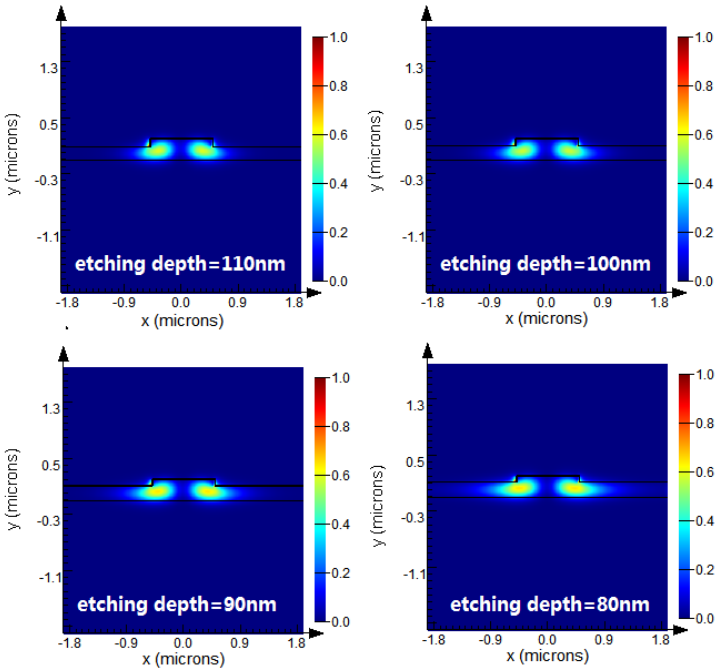

Figure 4.3 TE_{01} mode field while etch depth varies

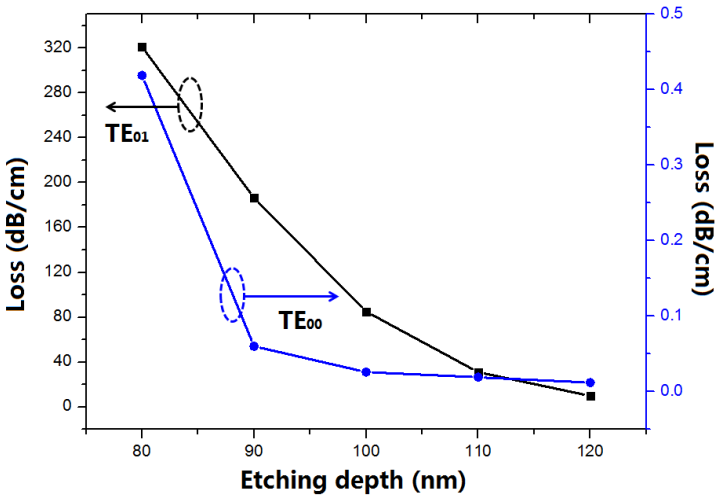

Figure 4.4 Loss performance of TE_{00} and TE_{01} mode versus etch depth

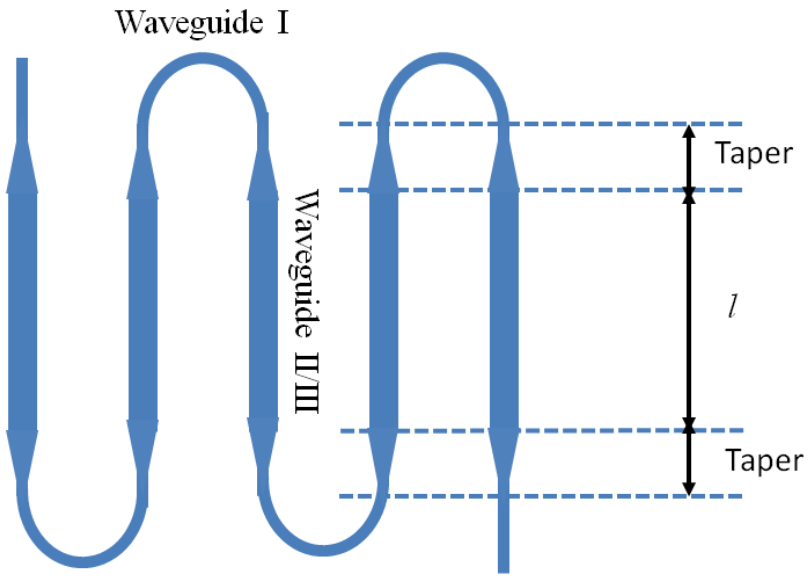

Figure 4.5 Cut back layout of the rib waveguides

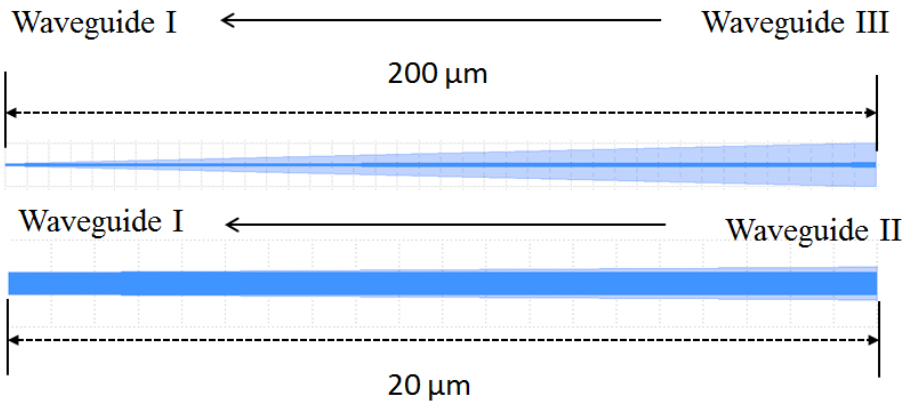

Figure 4.6 Tapers used for delay line design

We have adopted the cut-back method to characterize the loss performance of the two types of rib waveguides. The structure layout is arranged as shown in Figure 4.5. The configuration details of waveguide transition tapers are illustrated in Figure 4.6. For low loss consideration, the length of the taper that links waveguide I and II has been set as 20 µm while that links waveguide I and III has been set as 200 µm. We have varied the waveguide length *l* as 200 µm, 800 µm and 1400 µm and measured the total insertion loss. The measurement result is given in Figure 4.7. Figure 4.7 (a)

shows the result for rib waveguide II. A propagation loss of ~ 2.7 dB/cm is obtained from the slope of the fitting curve. Similarly, Figure 4.7 (b) indicates the propagation loss for rib waveguide III and it can be seen that a low propagation loss of ~ 0.1 dB/cm is achieved. The great difference in loss behavior of waveguide II and waveguide III is attributed to the different level of scattering loss from the sidewall area and electric field (E-field) distribution in both waveguides. From the field distribution shown in Figure 4.1 (b) and (c), it is obvious that waveguide II has larger sidewall area and relatively stronger E-field on the sidewall boundary (although the width of bottom step is deliberately increased to 750 nm), thus introducing larger scattering loss from the etching process induced sidewall roughness. However, for the waveguide III, only the top step has a rough sidewall boundary which is also relatively further away from the mode center due to wider rib width of 1 μm, and this contributes to the much better loss performance as expected.

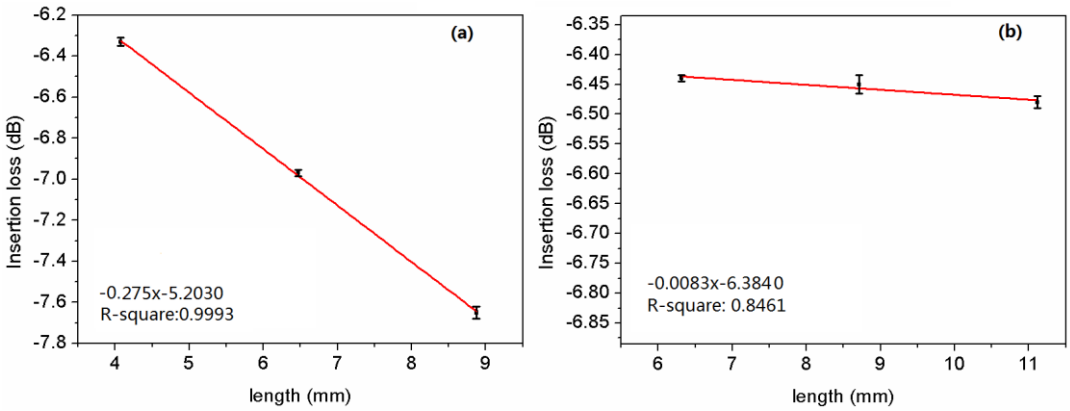

Figure 4.7 The loss performance for (a) rib waveguide II and (b) rib waveguide III.

4.3 Low loss delay line unit design and optimisation

With the three types of waveguide structures given in section 4.2, we design two classes of delay line units named by type S1 and S2 for discussion convenience. Both

S1 and S2 delay lines adopt waveguide I as the bend section, but S1 uses rib waveguide II and S2 uses waveguide III for their straight optical path. The top view of our proposed delay line unit layout is illustrated in Figure 4.8. In our design we vary the structure dimension parameters such as, the track number *N*, internal bend radius *r* and spacing between neighboring tracks *d*, to characterize the delay property of the proposed delay lines.

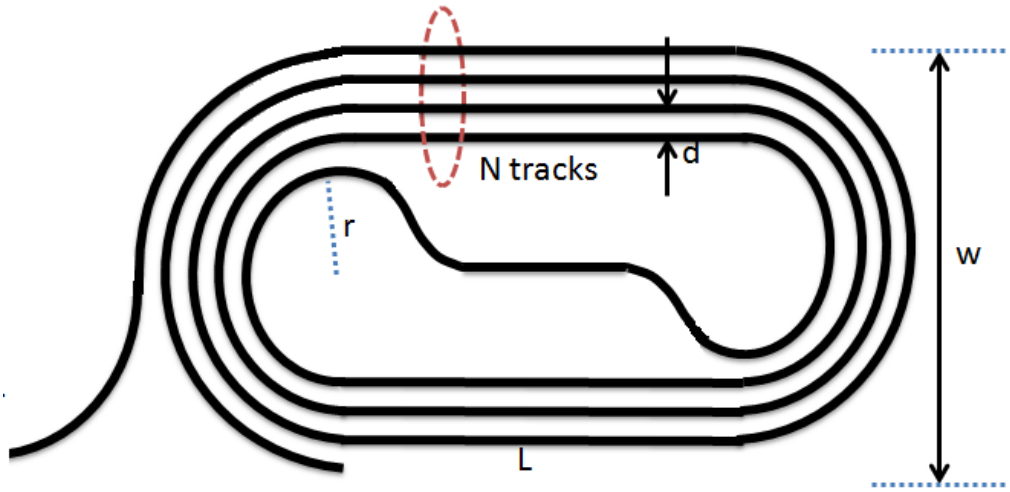

Figure 4.8 Main parameters for the delay line unit structure.

There are some basic length relations and restriction conditions required as proper design considerations. We list all these relations as below and the design problem is expressed as an optimisation model of Eq. (4.1) (length unit in μm):

$$\min : \mathrm{Loss}(N, r, d, L, w_s, w_b)$$

$$s.t. \begin{cases} delay = 50ps; r \geq 10um; \\ d \geq 6um; L \geq 40um(S1); L \geq 400um(S2). \end{cases} \tag{4.1}$$

$$\begin{cases} S\ bend : L_{sb} = 2 \cdot \sqrt{30^2 + [{}^{(2r-d)}\!/_{2}]^2}; straight : L_s = (2N-1) \cdot L + L - 60; \\ bend : L_b = \pi[r + (N-1)d] \,/\, 2 + \pi(r + Nd) \,/\, 2 + [2\pi r + \pi d \cdot (N-1)]N. \end{cases}$$

Where, *N*, *r*, *d* and *L* are the structure dimension parameters which are illustrated in Figure 4.8. The parameters, w_s and w_b are the propagation loss of the straight and

bend waveguides which can be obtained by measurement. The objective is to make the loss of delay line as low as possible. It is to be mentioned that, on the internal track, we have used two S bends to bridge the straight and semi-circle bends and the length of each S bend can be approximated with the hypotenuse length of a rectangle as $30 \times (2r\text{-}d)/2$ μm^2. As for the restriction conditions, a minimum internal radius r of 10 μm is taken for low loss consideration; the spacing d between neighboring track waveguides is selected as 6 μm for good crosstalk isolation. In this case, the direct coupling length is much greater than the straight waveguide length L. Taking type S2 as an example, a more intuitive illustration is given in Figure 4.9. We can observe that the crosstalk is strong for the waveguide spacing of 2 μm, since it is easy for power coupling to happen between these waveguides. For 6 μm spacing, there appears nearly no crosstalk between the waveguides. For type S1 (S2) delay line, the length of straight waveguide L should be larger than 400 μm (40 μm) since the transition taper section is set to 200 μm (20 μm) to guarantee low loss and no high order mode excitation in the transition section. To calculate the total delay of the structure, we should sum the group delay contributed by each section of the delay line unit. The characteristic group delay (per unit distance) of the three types of waveguides is calculated using Lumerical FDTD solutions [2]. For waveguide I, II and III, the characteristic group delay is 13.53, 12.83 and 12.22 μs/km, respectively. Then, the delay restriction has been written in such a way that the sum of the product of the characteristic group delay and individual waveguides length of bend and straight sections is equal to 50 ps. Through analyzing the optimisation model, it is easy to obtain the conclusion that less number of tracks and shorter bend section can exert better loss performance. This is more obvious for type S2 delay lines. The optimisation modeling method can solve sophisticated design cases while more restriction conditions and variations are involved. In this case, the potential optimized

parameters can be determined with the help of some optimisation algorithms like genetic algorithm.

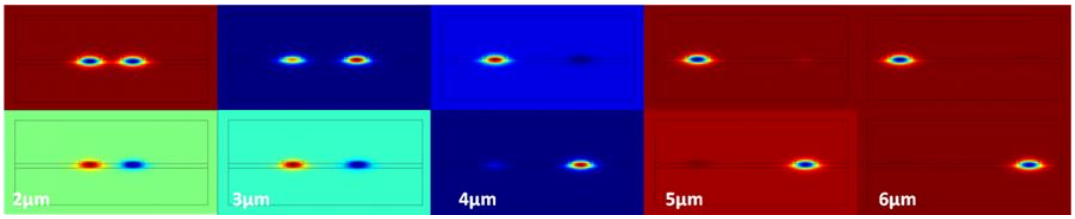

Figure 4.9 Crosstalk between two neighboring waveguides versus spacing from 2 to 6 μm performance.

4.4 Experimental demonstration of low loss 50 picosecond delay line

We fabricated the silicon waveguide based delay line in silicon-on-insulator (SOI) platform through Institute of Micro Electronics (IME) CMOS fabrication process. The fabrication has been done on an 8 inch SOI wafer with a 340 nm top silicon layer thickness and 2 μm buried oxide (BOX) layer. Thermal oxidation is adopted firstly in order to thin down the silicon layer to 300 nm. The device is patterned by DUV photolithography, followed by a two-step silicon reactive ion etching (RIE) down to the BOX layer. To increase the coupling efficiency between lensed fiber and the device, the waveguide ends were terminated with Spot Size Converters (SSC) having a length 200 μm and tip width 180 nm. The whole structure is finally covered by 1.1 μm silicon dioxide (SiO_2) cladding layer. The normal fabrication technologies are used to make the delay line structures, which is compatible with real large-scale production. We have fabricated several different types of delay line units. The microscope photo graph of the structures is shown in Figure 4.10. Two delay line units are labeled as examples to tell the difference between the fabricated type S1 and S2 delay units.

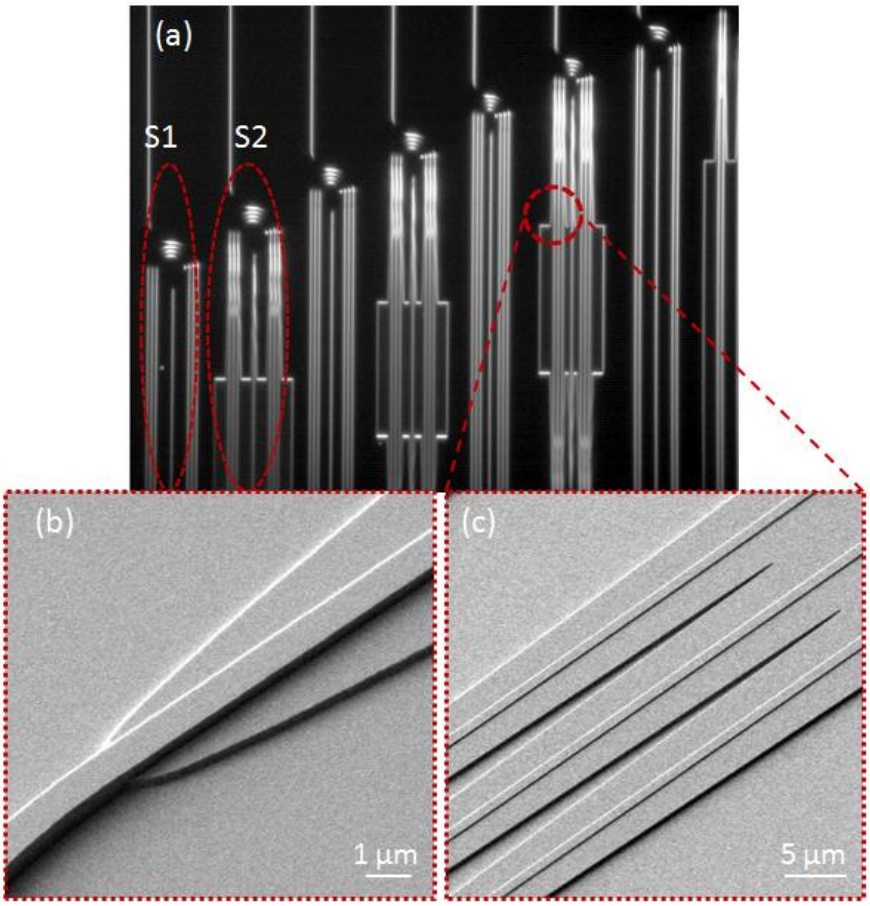

Figure 4.10 Microscope photo graph of the proposed delay line units the structure top view (a) and the details (b) and (c).

The loss performance of the fabricated delay line units has been characterized. The loss measurement setup is shown in Figure 4.11 (a). The polarization controller is adjusted to make the system work at TE polarization. A Power Meter (PM) has been used for the fiber-to-chip alignment and to record the received optical power. The spectral property is characterized by an optical spectrum analyzer (OSA). The different delay line units are labeled as delay line type (S1 or S2) followed by {*N*, *r*, *d*, *L*}. With reference to the fiber to fiber coupling loss, the measured insertion loss and spectral response for several kinds of delay line units are shown in Figure 4.12. Figure 4.12 (a) is the measurement result for delay unit S2 {2, 10 µm, 6 µm, 969.229 µm}. Through a linear fit to the graph between insertion loss versus the number of delay line units, an excess loss of ~0.7 dB per unit is achieved. The inset of Figure 4.12 (a)

shows the recorded spectrum for the delay line with 1, 2 and 3 units. The fringe free spectrum indicates a wideband performance without high order mode excited. Likewise, Figure 4.12 (b) and (c) illustrate the measurement results for delay line S2{3, 10 μm, 6 μm, 619.168 μm} and S1{3, 10 μm, 6 μm, 619.168 μm} with an excess loss of about 1.15 dB per unit and 2 dB per unit, respectively. Note that we have used the same straight waveguide length for type S1 and S2 delay lines due to close characteristic group delays of waveguide II and III. The spectral responses have shown a wideband operation. It is obvious that the type S2 delay units has better loss performance than S1 since they use much lower loss rib waveguide III. For type S2 delay lines, most of loss is introduced by the bend waveguide section. The measurement results also indicate that decreasing the number of tracks (i.e. reduce the length of bend section) will improve the excess loss performance, as predicted by the optimisation model.

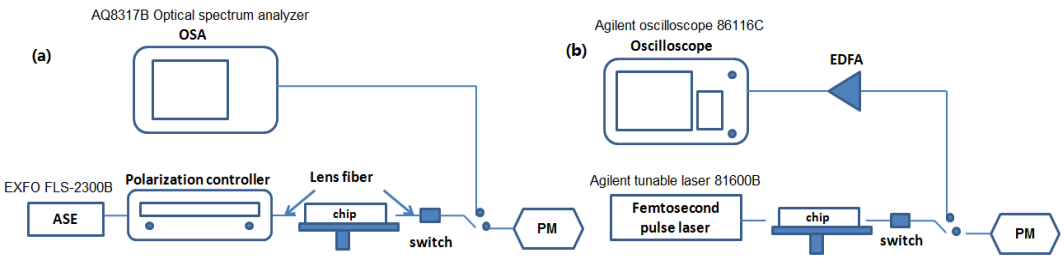

Figure 4.11 (a) Loss measurement setup and (b) Group delay characterization setup.

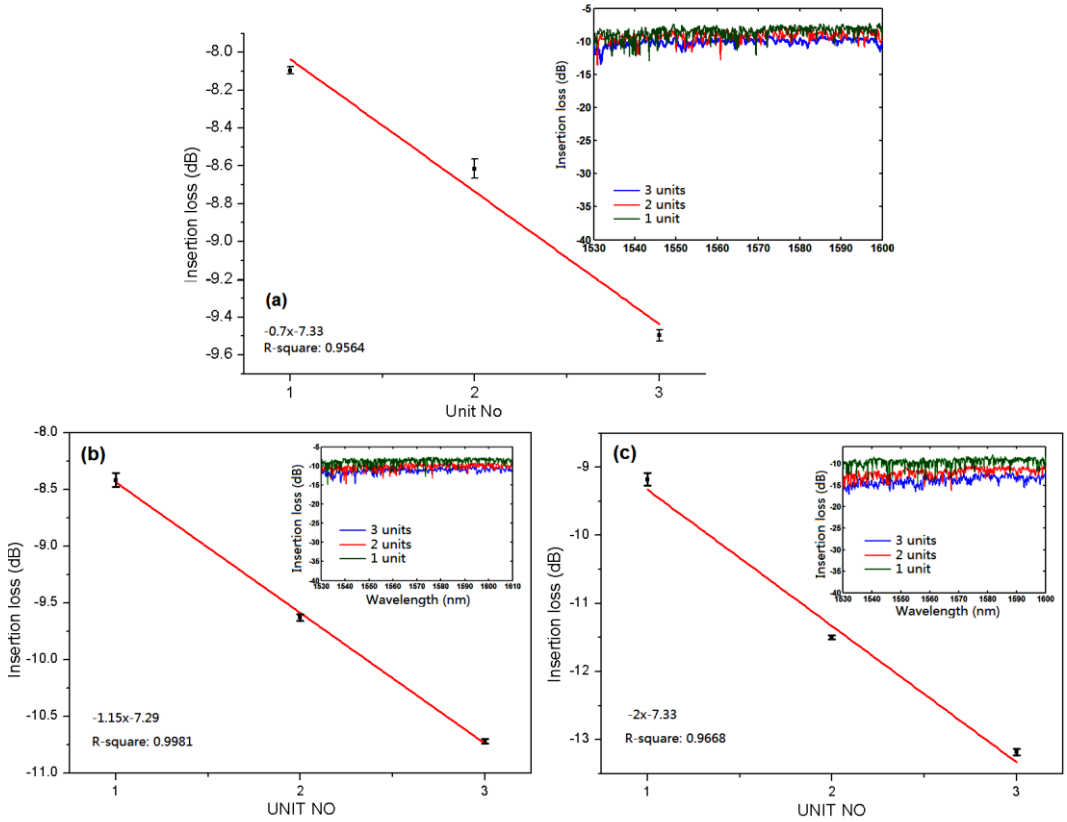

Figure 4.12 Excess loss measurement for several type of delay units (a) S2 {2, 10 µm, 6 µm, 969.229 µm}, (b) S2 {3, 10 µm, 6 µm, 619.168 µm} and (c) S1 {3, 10 µm, 6 µm, 619.168 µm}

Then, we further characterize the delay property of the proposed delay line units using direct time domain method measurements. Group delay is a measure of the time delay of the amplitude envelopes of a signal through transmission media. It is different from phase delay which measures the time delay of phase. The measurement setup is illustrated in Figure 4.11 (b). We have used a femtosecond pulsed laser as light source with a fast optical oscilloscope to detect the amplified pulses from the delay line waveguides with 1, 2 and 3 delay units. Here, power meter is used only for fiber-to-chip alignment. We measured S2 type delay lines for their better loss performance. The measurement results of abovementioned S2 {2, 10 µm, 6 µm, 969.229 µm} and S2 {3, 10 µm, 6 µm, 619.168 µm} delay lines are shown in Figure 4.13. It can be seen that the uniform intervals between two neighboring pulse is around 50 ps. By fitting

the delay measurement results, it is clear that S2 {2, 10 μm, 6 μm, 969.229 μm} gives 50 ps delay and S2 {3, 10 μm, 6 μm, 619.168 μm} introduces about 52 ps delay. The observed delay variation mainly comes from the possible measurement reading error (due to the broadened pulses because of system bandwidth limitation) and the fabrication imperfection such as geometry deformation. We have measured many fabricated delay line samples from two batches of fabrications, and observed that the delay variation is within 3 ps.

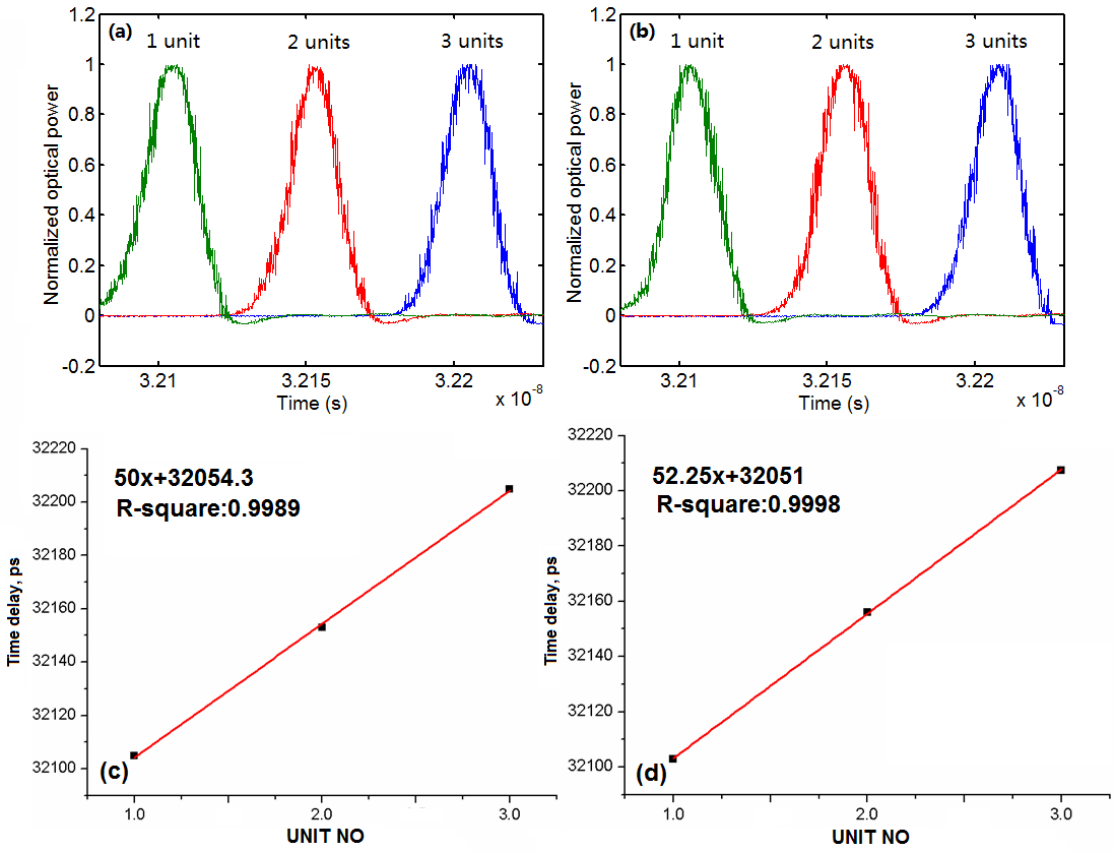

Figure 4.13 Pulse delay measurement for delay units: (a) and (c) for S2 {2, 10 μm, 6 μm, 969.229 μm}; (b) and (d) for S2 {3, 10 μm, 6 μm, 619.168 μm} through 1, 2 and 3 delay units.

4.5 A frequency domain method to measure silicon waveguide group delay

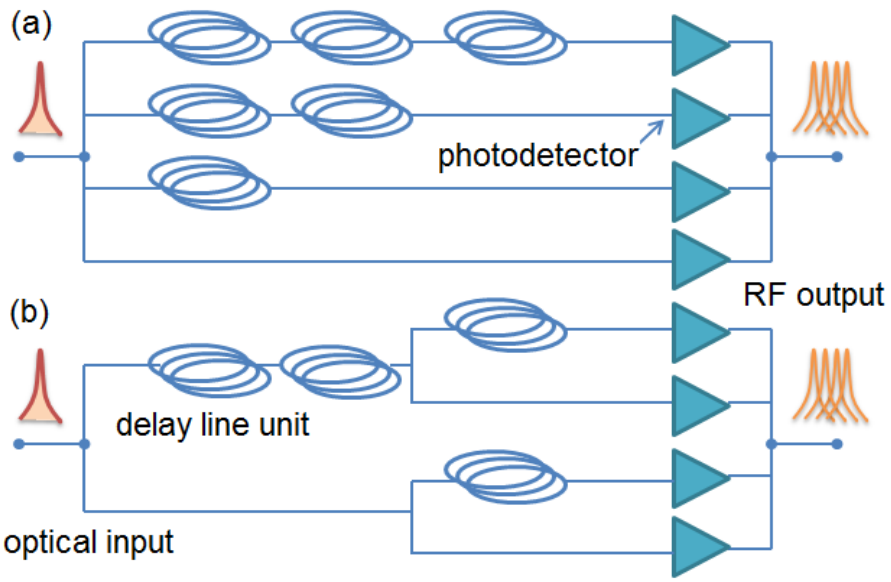

Figure 4.14 The schema illustration (a) original functional schema; (b) an alternative simple schema with less number of delay units.

In our measurement, we not only use the conventional time domain method to measure the group delay of our fabricated delay units, we also adopt a frequency domain method to verify the measurement results. The frequency domain method simplifies the measurement setup and releases the rigorous instrument requirements. Using the method, only common instruments i.e. regular speed modulator, photodetector (PDs) and spectrum analyzer are required to realize the group delay measurement on chip with the high sensitivity and stable operation. Although we are not the first to propose the method [112], we have greatly promoted the method from theoretical aspects to general cases and provided the calculation formula and an accuracy analysis. It is known that the measurement accuracy of the time domain method is limited by the pulse width. This limitation is excluded from the frequency domain method, enabling accurate measurement within the radio frequency (RF)

domain. We theoretically analyzed the working mechanism of the proposed method and experimentally demonstrated the group delay measurement of the silicon waveguide based delay line unit samples.

The proposed group delay measurement schema is shown in Figure 4.14 (a). In the schema, the input signal carried with pulse or harmonic wave is split into branches with the arithmetic series number of delay units/samples, making each branch have different delays. After they experience different delays, the signals are detected by the photodetectors within each branch. Then the detected radio frequency signals coherently superpose in the RF domain due to the group-delay induced phase shift. Thus there will appear specific fringes over the RF response spectrum. The frequency response function $H(f)$ can be expressed as:

$$H(f) = \sum_{n=0}^{N-1} w(n) \cdot \exp(-2\pi i f n T) \qquad (4.2)$$

Where N is the total branch numbers, f is the frequency, T is the group delay of one delay unit, $w(n)$ is the transmission weight of each branch, i.e. the transmission percentage of the total optical power. An optimized schema with fewer delay units/samples are also proposed as shown in the Figure 4.14 (b). Here, we take this schema with four branches as an example for analysis (the case with more branches has similar properties), and we also experimentally measure group delay of a delay line unit with the schema.

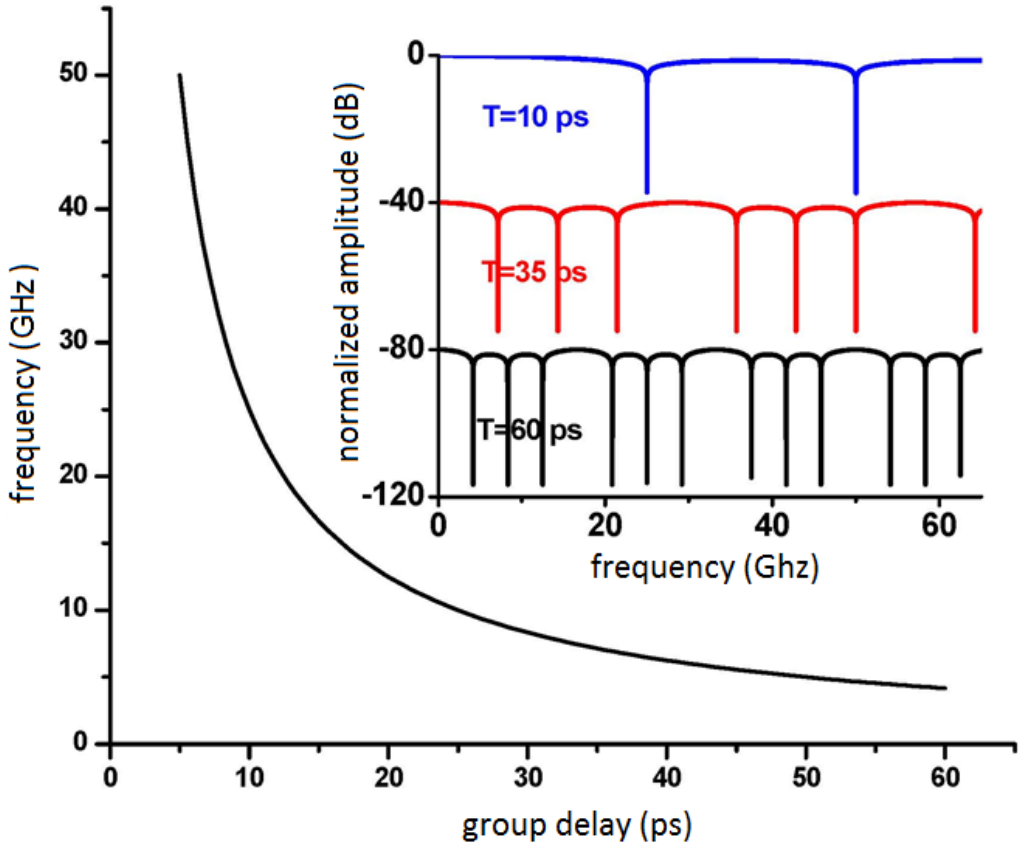

Figure 4.15 First order dip frequency of the response spectra versus the group delay. The inset shows the calculated spectra.

We first analyse the system spectral response under different group delays. In following discussion, the calculation is based on Eq.(4.2) using equal weights for all the branches. As shown in the inset of Figure 4.15, the first order spectral dip appears at different frequency when the group delay changes. Thus, the first order dip frequency can be used to identify the group delay induced by the delay unit. In Figure 4.15, it can be seen that the first order dip frequency decreases when the group delay increases. By fitting the curve using reciprocal equation, we can obtain the exact relationship between the group delay and the first order dip frequency as given in Eq. (4.3), here the delay is considered in the range from 5 ps to 60 ps (we can process the delay in other range in the same way). It should be noted that the fitting equation indicates the relationship between the group delay in ps and the first order dip

frequency in GHz. This equation is critical for the group delay calculation as well as measurement sensitivity and error analysis.

$$T = 250 / f \tag{4.3}$$

As shown in Figure 4.15, when the delay unit has a less delay, the system can achieves a better measurement sensitivity, which is defined as the first order dip frequency shift according to 1 ps change in delay. Based on the Eq.(4.3), we can calculate the first order dip frequency shift sensitivities at different delay values, for example, the sensitivity is ~2.5 GHz/ps at 10 ps delay, ~0.4 GHz/ps at 25 ps delay and ~0.1 GHz/ps at 50 ps delay. Although the first order dip frequency shift sensitivity is greatly reduced at large delay values, we still can achieve high measurement sensitivity by using the high order dip frequency. In our schema, taking 60 ps delay as an example, its first order dip frequency shift sensitivity is ~0.069 GHz/ps, and its second order and third order dip frequency shift sensitivities increase to ~0.14 GHz/ps and ~0.21 GHz/ps, respectively. High order dip frequency can be used to increase the measurement sensitivity. However, if the high order dip frequency exceeds the detection range of photodetectors and RF spectrum analyzers, then we need to use much expensive instruments with higher working frequency to do the measurement. Provided that the high order dip doesn't appear in high frequency, here taking 60 ps delay as an example, the second order and third order dips appear below 15 GHz as shown in the inset of Figure 4.15, therefore it doesn't need to use costly high frequency photodetectors or RF spectrum analyzer to do the measurement. Considering that the spectral response properties in the system and the resolution of common spectrum analyzer (1 MHz), the proposed method can achieve the sub-picosecond delay accuracy or even better.

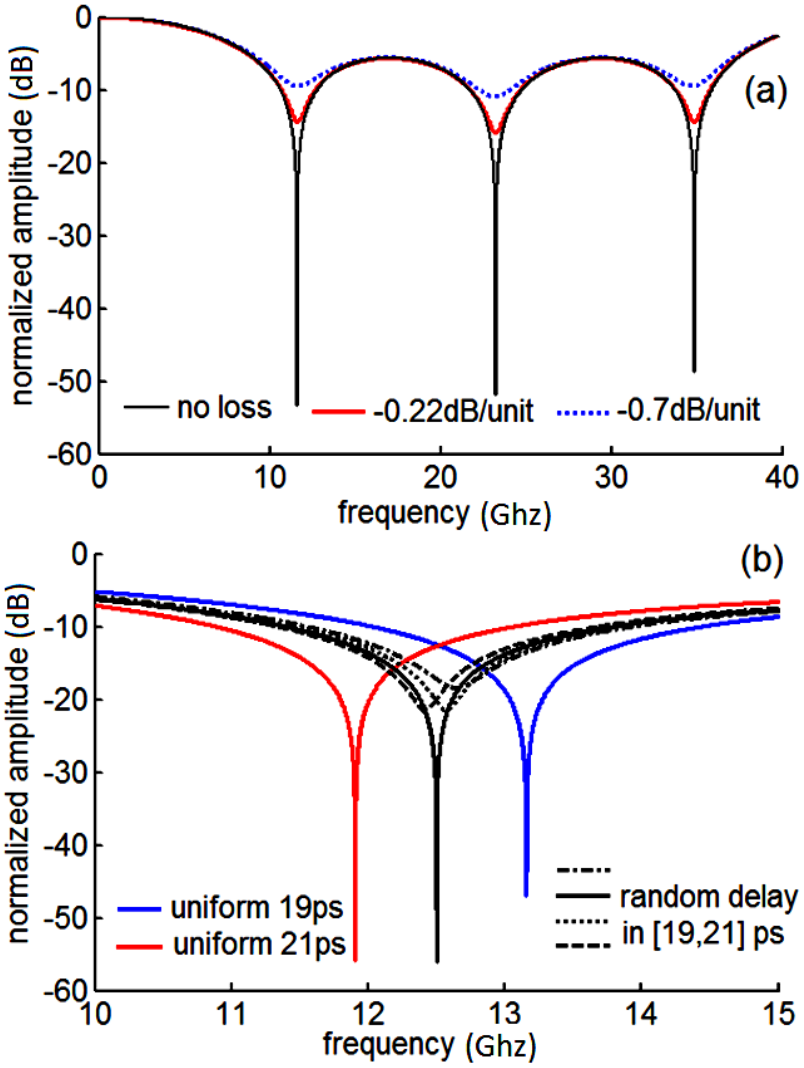

Figure 4.16 Spectral response under (a) different loss and (b) non-uniform delay

In real systems, the loss and non-uniformity of the delay units are inevitable, thus we investigate how the loss and non-uniformity influence the performance of the proposed methods. To study the effect of loss, we set the delay units with a constant delay of 21.5 ps as an example, and vary the loss of the delay unit i.e. 0.7 dB per unit (85% transmission), 0.22 dB per unit (95% transmission) and zero loss (with equal transmission weight). As shown in Figure 4.16 (a), when the loss increases, the amplitude of the dip decreases, but the dip frequency keeps constant. This feature can be understood that in the schema the delay-units induced loss only affects the spectral amplitude, and the dip frequency is only determined by the delay-unit induced delay.

Thus, regardless of how much loss the delay unit induces, the group delay of the samples can be achieved from the first order dip frequency. It is even unnecessary to obtain the whole response spectrum as long as the dip frequency position is found. Since the loss has no influence on the dip frequency of the response spectrum, we can use the equal transmission weight as the reference to clearly identify the first order dip frequency in the real calibration (but to fit the spectrum curve is a more accurate way which can reduce the possible reading error). To study the non-uniformity induced influence, we set the delay units with random delays distributed between 19 ps and 21 ps. In Figure 4.16 (b), it can be seen that the obtained dip frequency always drops in the range between the two dip frequencies obtained when each delay units have the uniform delays of 19 ps and 21 ps. It means that the proposed method actually gives the middle delay value when the delay units have variations in performance. It is therefore reasonable to reflect the real delay behavior of the set of delay units. It is worthy to mention that the frequency domain method can be also used to characterize the group dispersion of a structure. The group dispersion can be achieved from the dip frequency changes when the optical carrier wavelength (or using multi-wavelength carriers) is varied. Meanwhile, the measurement resolution can be increased by using the high order dip frequency. In addition, the schema can be flexibly configured according to the specifications of the available instruments. For instance, if the spectrum analyser cannot function well at the high frequency range, we can cascade more number of delay units as a new encapsulated unit in the schema, enabling the group delay measurement in the low frequency range. Finally, for the case that the to-be-measured delay units have large loss, the low contrast of the spectral dip (as shown in Figure 4.16 (a)) may affect the measurement reading. A feasible solution is to add a power amplifier at each branch to compensate the loss and achieve uniform weight to exert high contrast dip for easy reading and reduce the possible observation error.

The frequency domain group delay measurement setup is illustrated in Figure 4.17. The optical carrier is a continuous wave laser at 1.55 μm wavelength modulated by the sweep harmonic RF signal. The modulated optical signal couples into and travels through the delay structure on the chip and then is collected by the photodetectors in RF domain, finally the detected RF signal is combined and analysed by the spectrum analyser. In our measurement, the on-chip photodetector array proposed in Chapter 6 is adopted to collect optical signals, but to use common off-chip photodetectors is also applicable for the proposed measurement approach. Here, one set of delay line units designed in the section 4.3 are used for measurement. We use the time domain method to directly measure the optical group delay of the delay line unit and the result is ~ 48.25 ps.

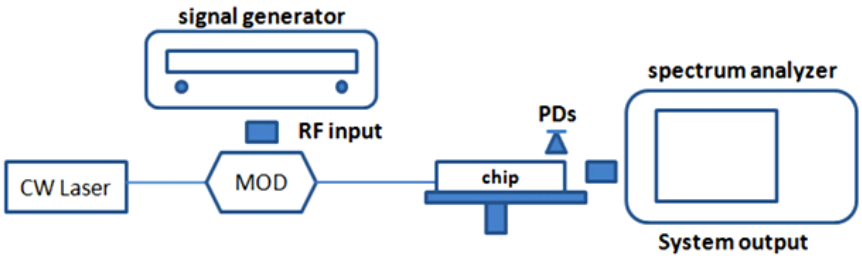

Figure 4.17 Experiment setup for the group delay measurement

Then, we do the measurement using the proposed frequency domain method. The measurement and simulation results are shown in Figure 4.18. The experimental result shows that the dip frequency locates at ~ 5.22 GHz as shown in the blue solid line in Figure 4.18. Based on Eq.(4.3), we can calculate the unit delay is ~47.9 ps, which is consistent with the result obtained by the time domain method in the sub-picosecond scale. The small variation between the time domain method and frequency domain method mainly comes from the possible measurement reading error and the inherent fabrication variation of the delay line samples. For calibration, we simulate the system

response based on Eq.(4.2). The simulation results with and without consideration of system loss (such as the delay unit loss, the bandwidth of RF cables and photodetectors) are shown in the red dashed line and dotted line in Figure 4.18, respectively. The experimental result is consistent with the simulation result. Here, it is worthy to mention that to fit the curve shape is a better way to do the calibration in order to reduce the observation error.

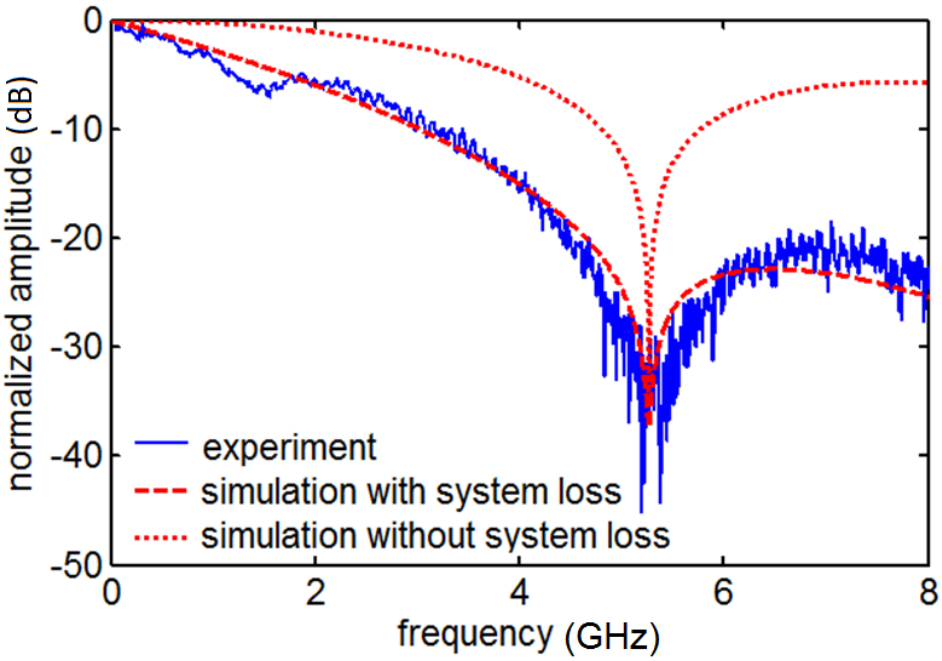

Figure 4.18 Measured spectral response and simulation results using the frequency domain method.

4.6 Summary

In summary of this Chapter, we have designed and demonstrated several 50 ps delay line units on a 300 nm silicon platform. The general approaches and critical considerations are summarized for silicon waveguide based passive delay line design and optimisation. Both the loss and delay performances have been characterized. We have demonstrated a low propagation loss of 0.7 dB per unit for 50 ps delay line unit. We have also improved a frequency domain method for the optical group delay

measurement. The working principle is theoretically analyzed and a demonstration of the frequency domain method is implemented to measure the silicon waveguide based delay line unit. The measurement result matches well with the theoretical prediction, and has a good agreement with the direct time domain method.

Table 3 ***Benchmarks for silicon rib waveguides***

waveguide	Excess loss	Waveguide width	Study approach
Oracle Labs, Oracle[28]	0.026 dB/cm	width: 3 μm	experiment
Our work, IME	0.08 dB/cm	width: 1 μm	experiment

Chapter 5 COMPACT LOW LOSS POWER SPLITTER DESIGN ON SILICON PHOTONICS

5.1 Introduction

Optical splitter is one of the critical components which are widely used in integrated Silicon-on-insulator (SOI) photonic platform. Many kinds of structures including Y-junction [41], [113], directional coupler [114] and multimode interference (MMI) waveguide [4], [43], [44] can be used to achieve 3 dB power splitting. Y-junction splitters have the most compact size and are polarization insensitive, but their sharp junction makes fabrication impractical – large scattering losses are common results of the limited etching resolution. On the other hand, we observe that another limitation in cascaded Y-junction splitters with multimode waveguide input/output is that unwanted high order modes are often excited, resulting in intermodal interference and narrow system bandwidth. Recently, Y. Zhang *et al*. improved the loss performance of Y-junction splitters to 0.28 dB by modifying the junction shape [41]. For directional couplers, they are normally used to design polarization splitters [45]–[47]. MMI splitters based on self-imaging effect are popular choice of beam splitting because of their superior properties in loss and large fabrication tolerance, etc. Till now, the best reported excess loss of MMI splitter reaches around 0.1 dB for TE polarization [4]. However, without proper design, MMI splitters can be heavily polarization dependent. Moreover, the very large footprint of multimode section also limits their practical application in densely integrated system. Tapered MMI splitters are proposed to decrease the device size but they bring trade-off with the loss performance [115].

In this Chapter, we design a MMI splitter by introducing a tiny multimode area to modify the field distribution so that the optical paths are aligned with the output branches for both TE and TE modes. This design can overcome the fabrication and efficiency limitations in a Y-splitter while maintaining the compactness and absence of high order mode excitation in the output multimode waveguides. We propose the rules to determine the minimum width of the multimode core waveguide in low loss performance region of MMI splitters and experimentally demonstrate the proposed polarization insensitive 3 dB splitter, and report a low excess loss over a fringe free transmission spectrum.

5.2 Design for the most compact polarization insensitive multimode interference splitter in low loss performance range

5.2.1 Fringes in Y-junction splitter with multimode waveguide

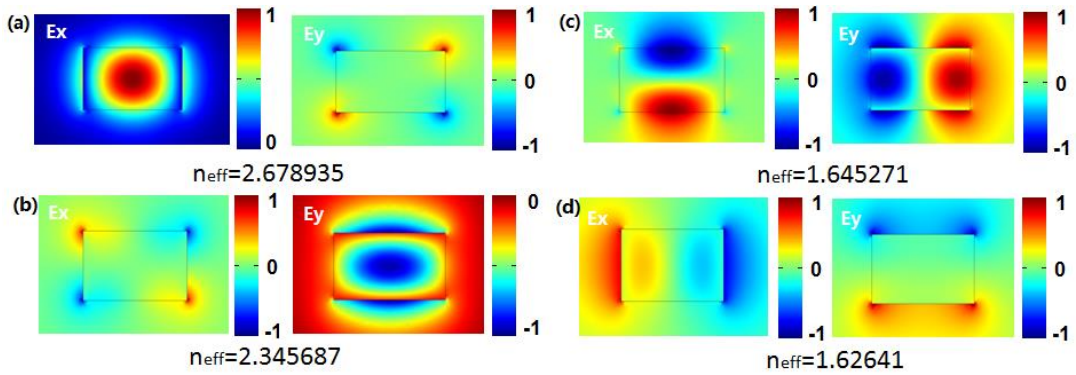

Figure 5.1 The supported modes in 500 nm × 300 nm silicon channel waveguide: (a) fundamental TE mode, (b) fundamental TM mode, (c) and (d) higher order hybrid modes

Normally, most applications require single mode waveguides as signal carrier. However, for some specific applications such as high speed multi-channel communication, multimode waveguide are required. However, we have experimentally observed that fringes exist in the output spectrum while Y-splitter is

applied to achieve power splitting for multimode waveguide input/output. This phenomenon indicates high order modes are excited in the waveguide and limits the operation to very narrow bandwidth. In our design, we have used a silicon waveguide with width and thickness of 500 nm and 300 nm, respectively. The waveguide layer is sitting on the BOX layer and covered with SiO_2 cladding layer. The waveguide configuration is also adopted for the integrated filter project stated in Chapter 6. The waveguide mainly supports the fundamental TE and TM modes; but it also supports two higher order modes which are shown in the Finite Element Method (FEM) simulation results in Figure 5.1. The mode field is calculated using COMSOL Multiphysics software[1]. In the device design, we have varied the bending radius(r) of the output waveguide branches as 20 μm (YI), 10 μm (YII) and 5 μm (YIII) to tune the splitting angle of the Y-junction, as shown in Figure 5.2. For each type structures, five splitters are cascaded to characterize the performance. The fabrication process of this group of Y-splitters is described in section 5.3. Figure 5.2 (a), (b) and (c) show the measured spectral behavior of each port of the three types of cascaded Y-junction splitters. From port p2 to p5, it is obvious that there exist periodic fringes over the spectrum. This is because the non-ideal branch point due to the limited etching resolution excites high order modes (i.e. the tangential wavevector component of the fundamental mode equals to the wavevector of higher order mode) which further interference with the fundamental mode and finally merge at the next Y-junction splitter. It can be observed that the fringe periodicity, i.e. free spectral range (FSR) increases with the decrease of the distance between two neighboring splitters. In Figure 5.2, the measured fringe FSR is around 20 nm, 25 nm and 28 nm for the splitter type YI, YII and YIII, respectively. Based on the interference principle, the fringe FSR, $\Delta\lambda$ can be estimated using the equation $\Delta\lambda = 1.552/(\Delta n_{\text{eff}} \cdot L)$, where Δn_{eff} is the effective index difference between the fundamental mode and higher order

modes, *L* is the transmission spacing length, i.e. the distance between two neighboring Y-junction splitters. The calculated FSR for the cascaded Y-junctions YI, YII and YIII is 21 nm, 24.5 nm and 26.8 nm, which are in good agreement with the measurement results. The observed spectral fringes make the Y-junction splitter applicable for only a very narrow bandwidth. The power splitting is not uniform for nearly the entire wavelength range of interest.

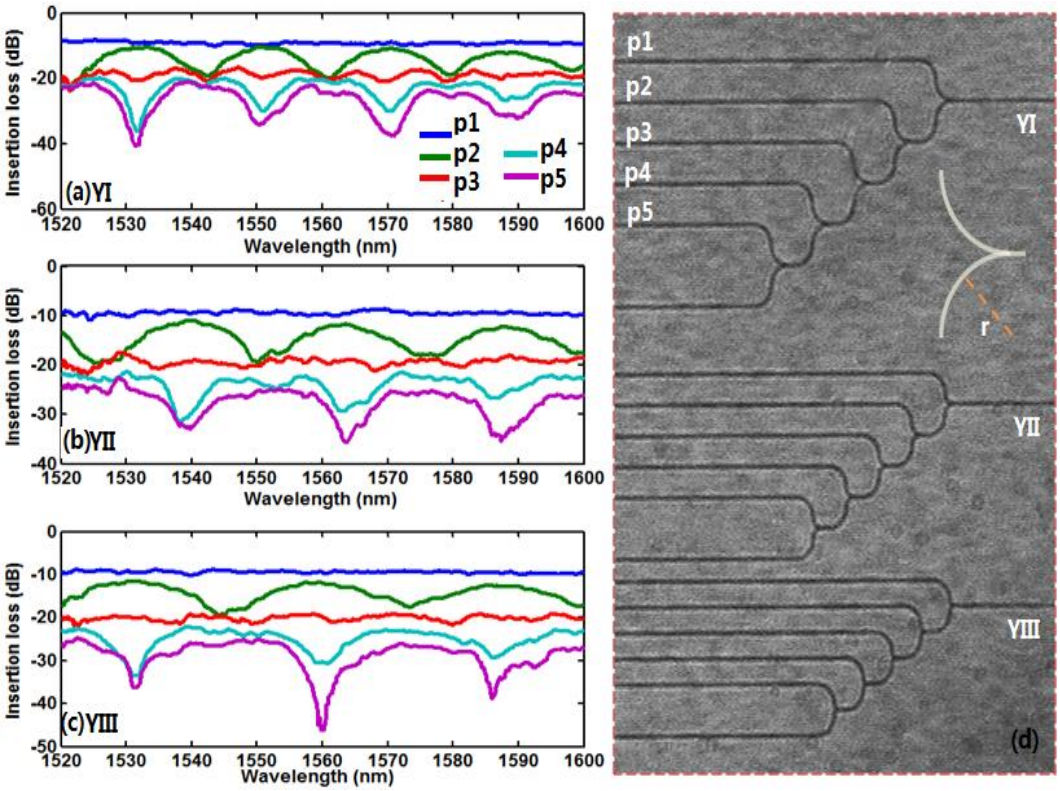

Figure 5.2 The spectrum of the cascaded Y-junction splitters (a) YI, (b) YII and (c) YIII; (d) The microscope picture of the three types of Y-junction splitters.

5.2.2 Multi-mode interference based on self-imaging principle

Before introducing our proposed MMI splitter design, we first briefly discuss the self-imaging mechanism of multi-mode interference and the required conditions to achieve polarization insensitive power splitting with MMI structures. Figure 5.3 illustrates the

schematic main parameters of a 1-to-*N* MMI coupler. The multimode core section has rectangle geometry of width W_M, height h and length L_M. The material refractive index of the multimode core is n_M. The input and output waveguides have the same width W_w, and a taper section can be applied at the joint in order to reduce the reflection to some degree[116]. In SOI-based design, the entire device is normally sitting on the BOX layer and covered with a layer of SiO_2 cladding. The cross-section parameters - height h and width W_M directly determine the dispersion relation of the multimode waveguide. The length L_M should be adjusted for application of specific output number according to self-imaging theory[117]. These parameters are crucial for the device performance.

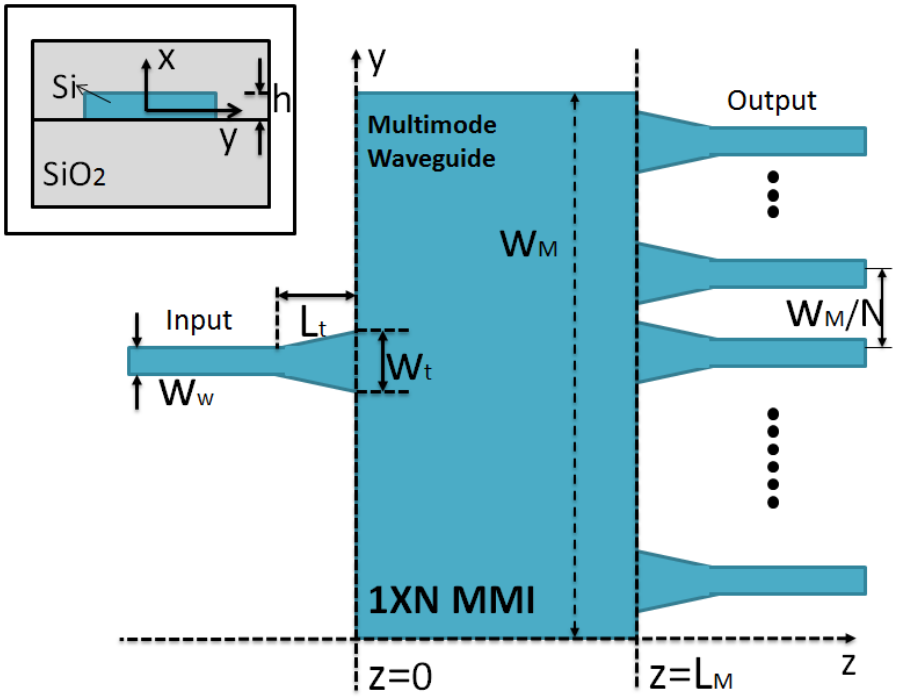

Figure 5.3 Schematic main parameters of a 1-to-*N* MMI coupler

We start from the dispersion relation to present the operation principle of MMI splitters. Several important considerations in design of a polarization insensitive MMI splitter and optimisation of its footprint are also discussed. In the multimode section, the propagation constant β_m of the m^{th} mode is related to the lateral wavenumber k_{ym}

and the refractive index n_M of MMI core by the dispersion equation (5.1) [117]. Eq.(5.1) is adapter to both TE and TM mode.

$$\beta_m = k_0 n_M \sqrt{1 - k_{ym}^2 / k_0^2 n_M^2} \qquad (5.1)$$

Where the lateral wavenumber is $k_{ym} = (m+1)\pi/W_{em}$ for mode m and $k_0 = 2\pi/\lambda_0$, W_{em} is the m^{th} mode lateral effective width which takes penetration depth (due to Goos-Hahnchen shift) into account at waveguide boundaries. If approximating W_{em} with W_{e0} and expanding the square root in Eq.(5.1) by only retaining the first order term, the propagation constant spacing can be written as $\beta_0 - \beta_m = m(m+2)/L_\pi$. Here, $L_\pi = \pi/(\beta_0 - \beta_1)$ is the beat length. For the 1-to-N MMI splitter structure in Figure 5.3, the imaging is excited by symmetric interference, and in this case, the N-fold images for TE and TM mode are obtained at distances[117]:

$$L_{MMI}^i = \frac{p_i}{N}\left(\frac{3L_\pi^i}{4}\right) \qquad (5.2)$$

p is a positive integer which indicates the imaging periodicity along z, i stands for TE or TM mode. In order to achieve polarization insensitive MMI device, we should make the N-fold image appear at the same distance for TE and TM modes[118], [119], so we have

$$p_{TE} L_\pi^{TE} = p_{TM} L_\pi^{TM} \qquad (5.3)$$

Eq.(5.3) is the condition for design of polarization insensitive MMI. Here, p_{TE} and p_{TM} should select small values for compact device size. Normally, the most compact design will be achieved when $p_{TE} = p_{TM} = 1$. This is also practical choice for common silicon waveguide dimensions.

There are several important considerations for optimisation of the loss performance as well as the device size. The resolution and contrast of the image determines the uniformity and loss behavior of MMI coupler. A high-quality image is formed when the multimode waveguide can support enough number of excited modes and the phase

differences between any two of them are exactly multiples of 2π. However, this should not be concluded that more excited modes supported by the multimode core can achieve better power splitting performance. In addition, the image plane distance calculated by Eq.(5.2) is not accurate owing to approximation in the derivation process, which actually introduces phase errors[117], [120], so we should correct the calculated length of multimode section according to Eq.(5.2) and optimize the length figure by simulation. Besides, to adjust the access waveguide width can also improve optical power collection, that is, a taper section can be applied for input and output waveguides for better power collection. For a MMI splitter, shorter beat length leads to smaller device length, which can obtain a smaller W_{MMI}. And in this case, a larger propagation constant difference β_0-β_1 is required. However, W_{MMI} cannot be too small with the consideration of fabrication resolution and loss performance.

5.2.3 Proposed splitter design and optimisation method

Based on the theoretical discussion in section 5.2.2, we consider modifying the field distribution at the branch point of Y-junction by introducing a small multimode area in order to remove the periodic fringes in the spectrum. The input and output waveguides have the same dimensions of 500 nm × 300 nm as the aforementioned Y-junction splitter cases. The schematic main parameters of the proposed splitter are shown in Figure 5.4 (g). With the added multimode section, the splitter input optical power will excite all the supported symmetric modes in the multimode area, i.e. TE_i/TM_i modes, $i = 0, 2, \cdots, 2n$, the subscript i indicates the number of field zero point along waveguide lateral direction, n is dependent on the width of the multimode waveguide section [117], [120]. Unlike the conventional large size MMI splitter, in our design, we select the width of the multimode region (W_M) to make it only support

the two lowest modes i.e. TE_0/TM_0 and TE_2/TM_2 modes. To satisfy this condition, the width value lies in the range of 1.49 μm to 1.95 μm. Through FDTD simulations, we observe that the widths in this range are satisfactory to design ultra-low loss splitter. However, the excess loss will increase for the width below ~1.5 μm.

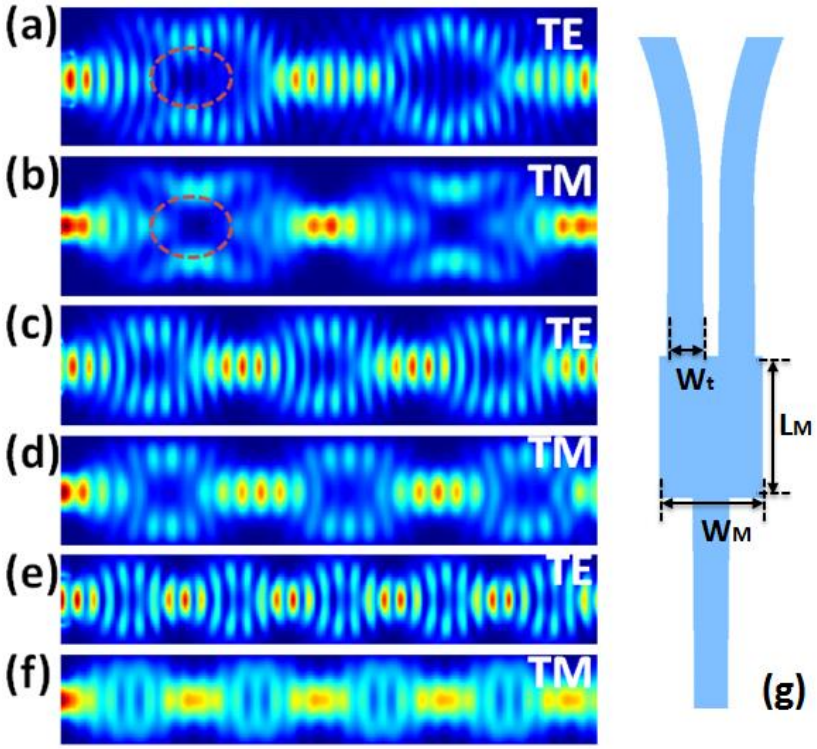

Figure 5.4 E-intensity field distribution for TE and TM polarization (top view) along the multimode section with different width. (a) and (b) for width W_M equals to 1.5 μm; (c) and (d) for width W_M equals to 1.25 μm; (e) and (f) for width WM equals to 1 μm. (g) The splitter schematic main parameters.

As an intuitive illustration, we take a long multimode section to show the field distribution for TE and TM polarization at different width configurations of W_M=1.5 μm, 1.25 μm and 1 μm. Figure 5.4 (a) and (b) illustrates the results for W_M = 1.5 μm which are right in the range to excite the lowest two modes. It can be seen that the two-fold power centers can be clearly formed with good resolution and contrast for both TE and TM modes. The low E-field in the cycled area will reduce the scattering

loss, allowing the power to be smoothly divided into two branches. From Figure 5.4(a)-(f), the splitting quality decreases with the reduction of the width of multimode area. It is difficult to find two-fold power centers in the case of W_M = 1 μm as shown in Figure 5.4(e) and (f).

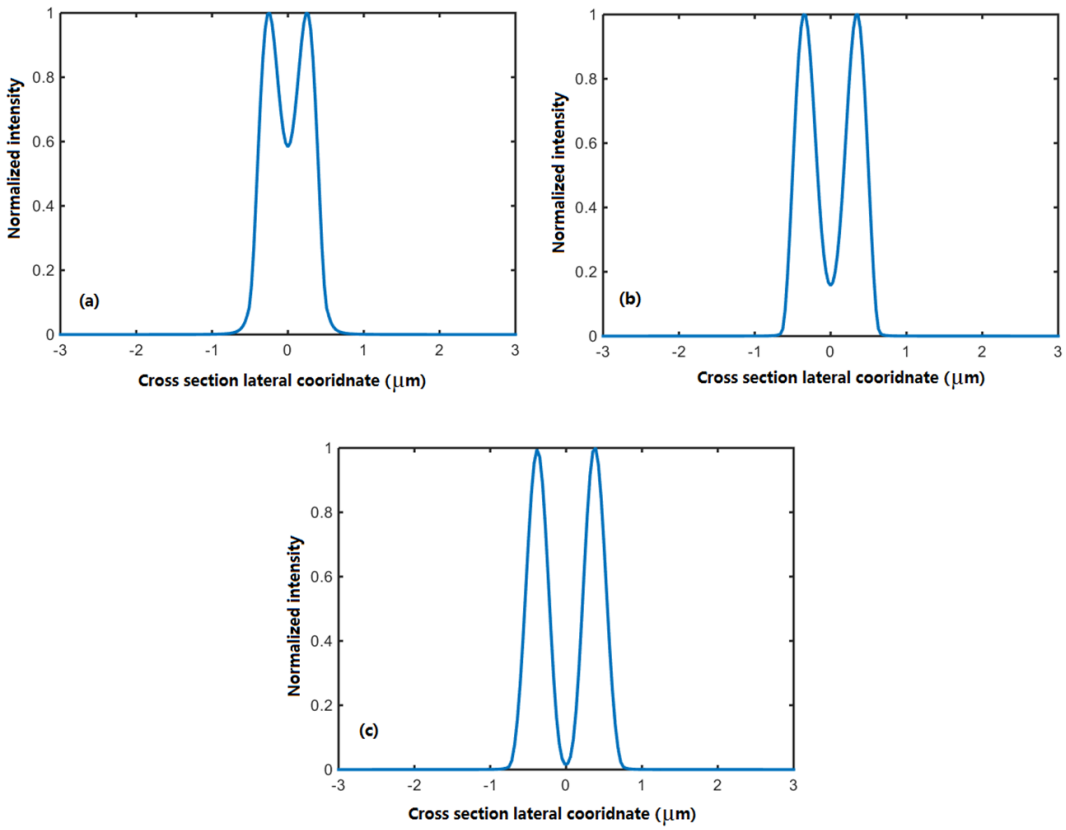

Figure 5.5 Intensity distribution on the image plane (a) multimode core width of 1 μm (b) multimode core width of 1.25 μm (c) multimode core width of 1.5 μm

In order to quantitatively explain the quality of the output two fold power images, we introduce "intensity contrast" index which is defined as I_{image}/I_{inter}, I_{image} is the field intensity of the image center and I_{inter} is the intensity of destructive field between images. "Intensity contrast" can be a useful parameter in optimisation of the MMI dimensions. High intensity contrast allows for low scattering loss and also brings tolerance to fabrication. Corresponding to Figure 5.4, the intensity contrast is

calculated as 1.7130 for 1 μm core width, 6.3669 for 1.25 μm and 60.4606 for 1.5 μm core width. The core width of 1.5 μm allows for a much better intensity contrast. The intensity distribution versus spatial coordinate in lateral direction of waveguide cross section is illustrated for the three cases in Figure 5.5, which obviously indicates the intensity contrast. For general 1-to-*N* splitter design, it can also find the corresponding minimum width which allows for low loss performance. From Figure 5.4 (a) and (b), it is obvious that the two-fold power centers appear at almost the same plane for TE and TM polarization. It means that this configuration can be used to achieve polarization insensitive power splitting.

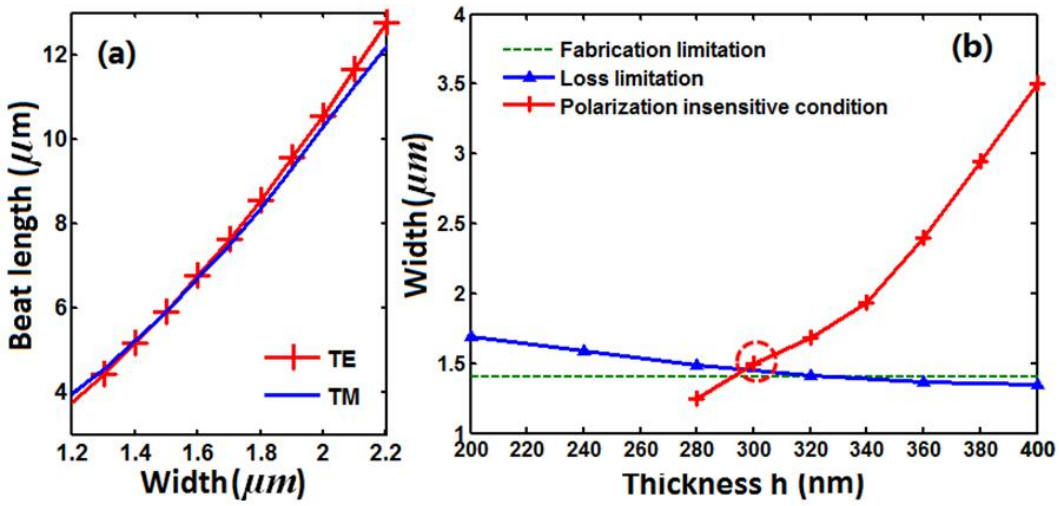

Figure 5.6 (a) TE and TM beat length versus the width of multimode section; (b) The fabrication and loss limitation and the polarization insensitive condition

We theoretically verify this according to polarization insensitive condition for multimode waveguide, i.e. TE and TM modes can share equal beating length [118], [119]. The beat length of TE and TM mode is illustrated as a function of width in Figure 5.6 (a). The equal beat length for both polarizations is achieved with W_M around 1.5 μm. We can also observe that the difference in beat length for TE and TM modes is not very sensitive to variation of width in this design, providing good

tolerance. In addition, the width value of 1.5 μm is also large enough to conquer the fabrication limitation by the etching resolution (As the deep ultra-violet (DUV), 248 nm photolithography is adopted with minimum feature size of 200 nm, so the multimode width needs to be at least 1.4 μm).

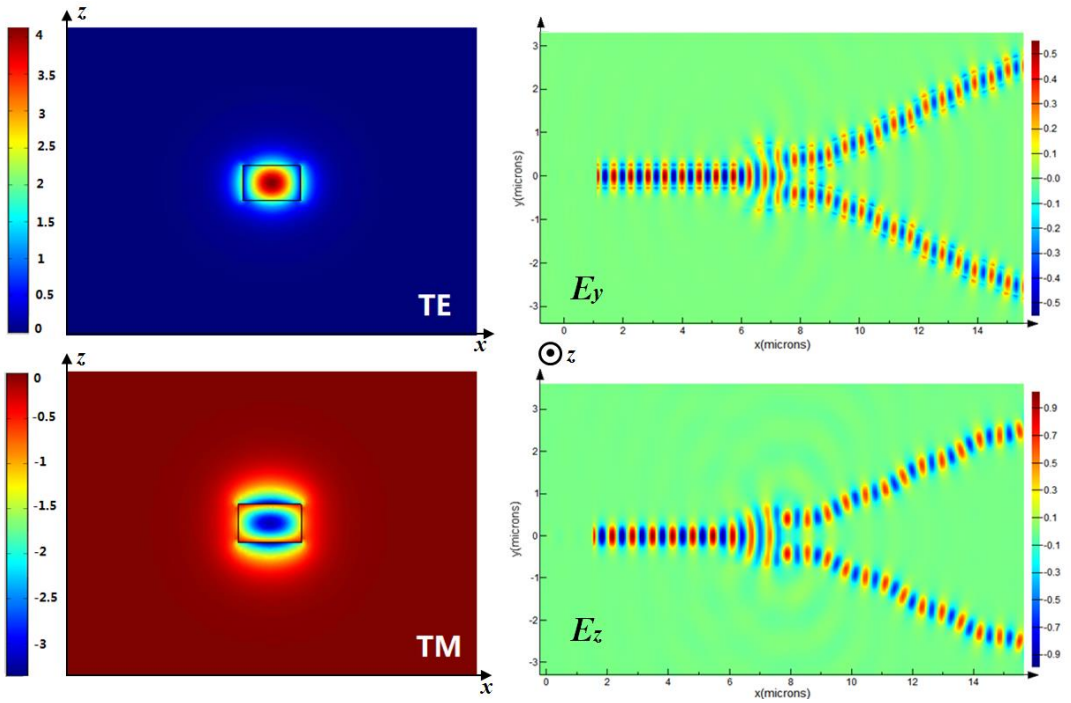

Figure 5.7 Simulation of 1-to-2 MMI splitter for TE and TM modes

As a matter of fact, this design is also the most compact 3 dB design which can simultaneously satisfy the fabrication limitation, loss limitation (i.e. the minimum width value that can exert two-fold clear power centers) and polarization insensitive condition, provided that the thickness of the multimode section is also taken into account for optimisation. The result is shown in Figure 5.6 (b). In Figure 5.6 (b), only the values above the fabrication and loss limitation curves can be used for a good design. It can be seen that the most compact design can be achieved with h = 300 nm and W_M =1.5 μm. In this case, the corresponding multimode area length L_M is 1.8 μm optimized by numerical calculation using Lumerical FDTD solutions [2]. With the

proposed design, the power distribution simulations of the MMI splitter for TE and TM mode are illustrated in Figure 5.7.

5.3 Experimental demonstration of MMI splitter and discussion

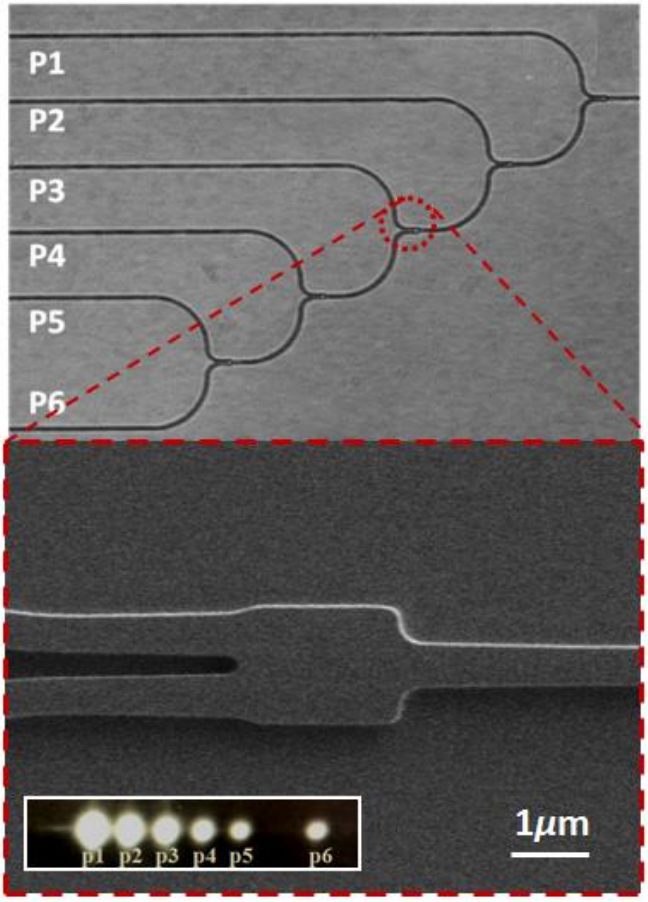

Figure 5.8 The microscope photo graph of the proposed splitters. Inset: the optical image captured from the output waveguides

We fabricated the polarization insensitive splitter in silicon-on-insulator (SOI) platform through the Institute of Micro Electronics (IME) CMOS fabrication process. The fabrication is done on an 8 inch SOI wafer with a 340 nm top silicon layer thickness and 2 μm buried oxide (BOX) layer. Thermal oxidation is adopted firstly in order to thin down the silicon layer to 300 nm. The device is patterned by DUV photolithography, followed by silicon reactive ion etching (RIE) down to the BOX layer. To increase the coupling efficiency between lensed fibre and the device, the

waveguide ends were terminated with Spot Size Converters (SSC) having a length 200 µm and tip width 180 nm. The whole structure is finally covered by 1.1 µm silicon dioxide (SiO_2) cladding layer. The microscope photo graph of the fabricated structures is shown in Figure 5.8. Five splitters are cascaded in order to measure the splitter excess loss. It can be seen that the proposed splitters have almost the same size as Y-junction splitter. The inset shows the optical image captured from the output waveguides.

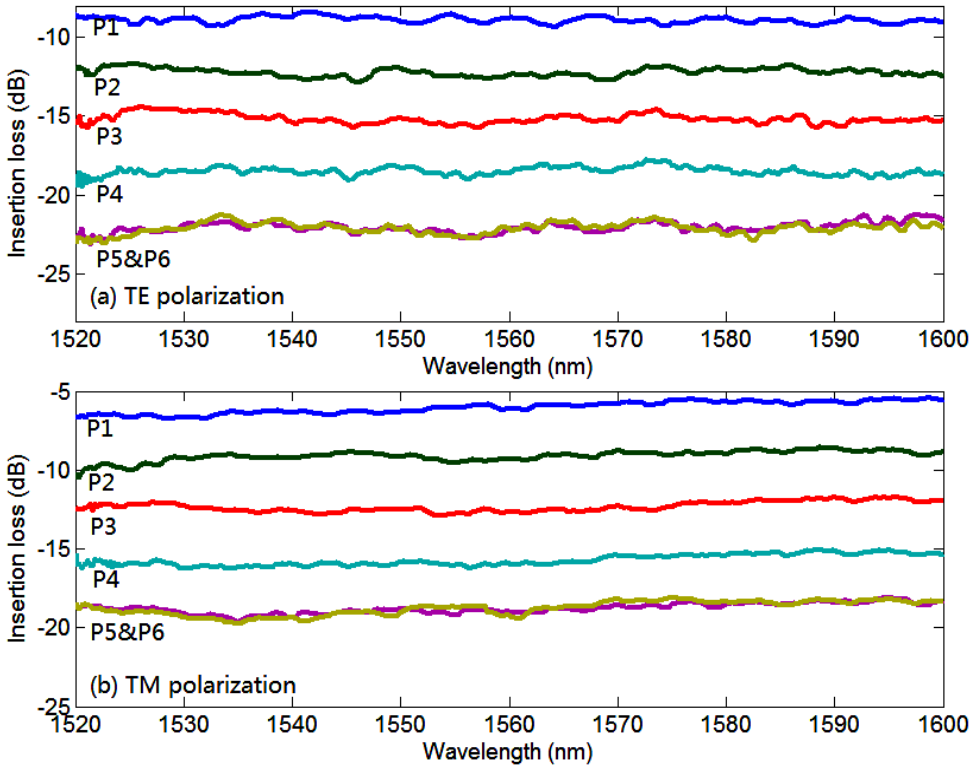

Figure 5.9 Spectrum at each output waveguide for (a) TE and (b) TM polarization light from amplified spontaneous emission (ASE) source referring to fiber to fiber coupling loss

Referring to the lensed fiber to fiber coupling loss, the measured insertion loss at each output waveguide for TE and TM mode is given in Figure 5.9 (a) and (b), respectively. When compared to the Y-junction splitter, the spectrum measured at each port of the proposed splitter is a smooth curve without any fringes from

wavelength 1520 nm to 1600 nm, which offers wide operation bandwidth. In Figure 5.9, as for the different insertion loss for TE/TM modes, it should be noted that the insertion loss includes the fiber-to-chip facet coupling losses, splitter excess loss and waveguide propagation loss. Splitter excess loss indicates the splitter performance, which is defined as the amount of light lost in the splitter beyond that inherent 3 dB splitting to output waveguides. Although the MMI splitter works polarization insensitively, the waveguide propagation loss and fiber to waveguide inverse taper coupling loss are polarization dependent, thus the total insertion losses for TE and TM polarization are different.

We linearly fit the insertion loss of each output ports to calculate the excess loss of the designed splitter. The fitting results are shown in Figure 5.10 (a) for TE polarization, Figure 5.10 (b) for TM polarization and Figure 5.10 (c) for unpolarized light. The slope of the linear formula is the excess loss plus the 3 dB beam-splitting drop, and the interception mainly reflects the fiber-to-chip facet coupling loss. The excess loss is 0.11 dB for TE polarization, 0.18 dB for TM polarization and 0.14 dB for unpolarized light. To the best of our knowledge, this is the best experimental result for polarization insensitive splitter till now. The access width of the input and output waveguides is also optimized to obtain the optimum performance in our design. Figure 5.10 (d) illustrates the relationship of splitter excess loss versus the access taper width W_t. It can be seen that the optimum loss performance is obtained while W_t = 540 nm. There exists some difference between the measurement and simulation values, which mainly comes from the fabrication variation like the geometry deformation and round edges etc. Although our proposed splitter has tiny footprint, the device has good fabrication tolerance. In our study, we find that only 0.1 dB extra

loss is introduced by ± 100 nm variation in multimode area length or by ± 20 nm variation in its width.

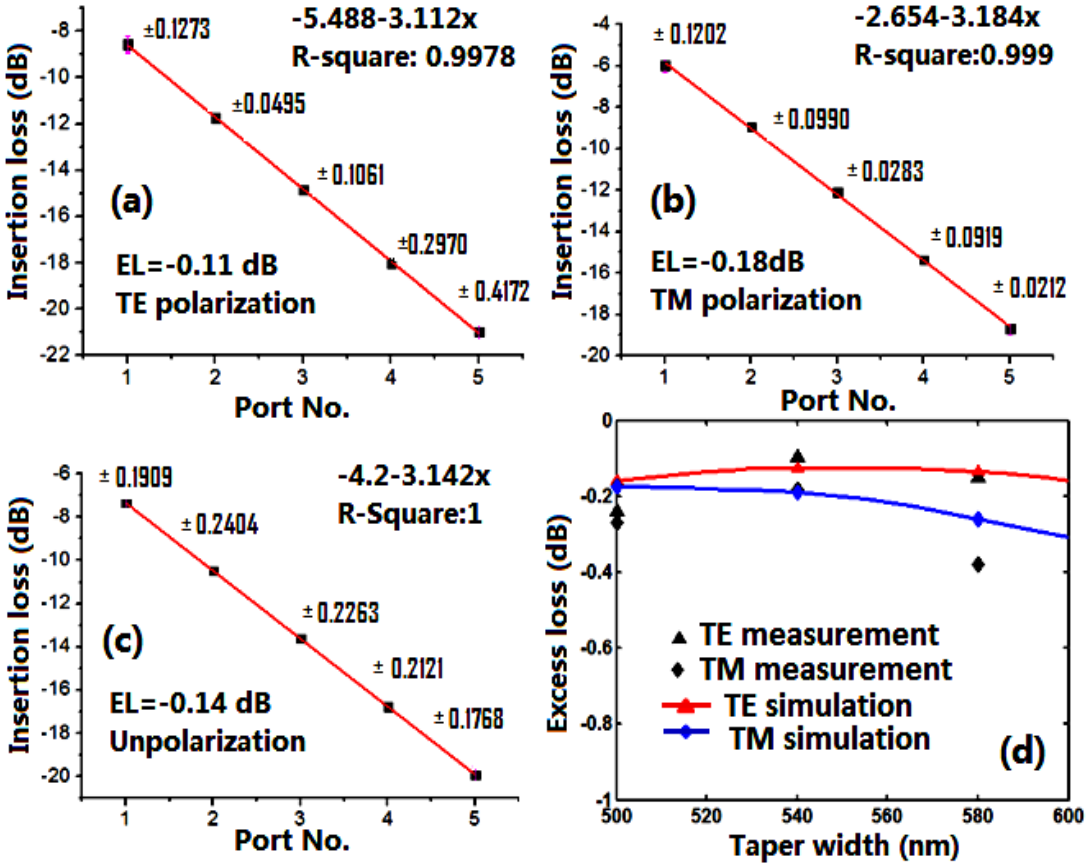

Figure 5.10 The measured insertion loss from the output ports for (a) TE polarization, (b) TM polarization and (c) unpolarized light at 1.55 μm wavelength; (d) The relationship of splitter excess loss versus taper width.

5.4 Summary

To summarize, we have designed and experimentally demonstrated an ultra-compact low loss MMI 3-dB power splitter. The design has all the merits of Y junction such as polarization insensitivity and ultra-compact size, and it also solves the problems of periodic fringes introduced by Y-junction in multimode waveguide applications. The device footprint takes only 1.5 × 1.8 μm^2. The excess losses for TE and TM mode are

0.11 dB and 0.18 dB, respectively. This is expected to be a practical power splitter design on SOI platform for large scale photonics integration.

Table 4 *Benchmark for the MMI splitters*

1-to-2 MMI	Excess Loss(dB)	Polarization	Compactness (width, length)	Study approach
Zhejiang Univ.[118]	Over 0.2 dB for both TE and TM modes	polarization insensitive	3.86 μm, 15.3 μm	simulation
City Univ. of Hong Kong[119]	TE:0.26 dB; TM:0.3 dB	polarization insensitive	3.78 μm, 16.64 μm	simulation
Bucknell Univ.[121]	0.5 dB for both TE and TM modes	polarization insensitive	4 μm, 16.7 μm	simulation
IMEC[122]	0.3 dB	TE	3 μm, 7.6 μm	experiment
IMEC[26]	Below 0.2 dB	TE	3 μm, 9.8 μm	experiment
Our work, at IME	TE:0.112 dB; TM:0.184 dB	polarization insensitive	1.49 μm, 1.9 μm	experiment

Chapter 6 SPECTRUM RECONFIGURABLE PHOTONIC MICROWAVE FILTER USING SILICON PHOTONIC TECHNIQUES

6.1 Introduction

Based on the work described in Chapter 3, 4 and 5, we have already obtained the grating couplers for fiber-to-chip excitation, low loss 50 ps delay line units and the compact low loss power splitters. This Chapter describes the integration of these components with variable optical attenuators (VOA) and photodetectors (PD) array to realize a spectrum reconfigurable microwave finite impulse response (FIR) filter. The working mechanism of FIR filter will be introduced and a feasible schema is proposed on silicon photonics platform. The design schema combines the advantages of both the fiber and on-chip sub-systems. The whole testing system and measurement results are discussed.

6.2 Research background

Microwave filters allow for selective transmission of input signals, so that signals are either transmitted through passbands or blocked in stopbands. Microwave filtering has been widely used in wideband radio frequency (RF) receivers, radio-over-fiber, satellite communications and military applications[123] etc. Most of the microwave filtering is realized using electronics. The typical configuration of electric microwave/RF filters is shown in Figure 6.1(a). However, electrical microwave/RF filters have major challenges such as electromagnetic interference issues with long delay lines, bandwidth limitation (only a few GHz), high power consumption, and

poor re-configurability[124]. Therefore, there is a trade-off among the size, re-configurability and signal speed for electric microwave/RF filters.

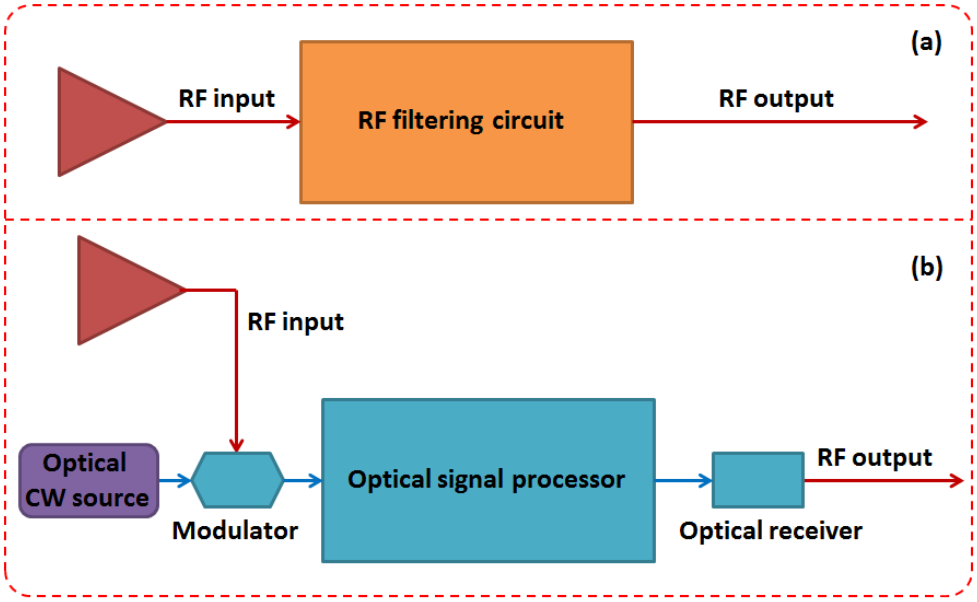

Figure 6.1 (a) Configuration of traditional electric microwave filters; (b) Configuration of microwave photonic filters

Microwave photonic filters (MPFs) were proposed with the aim of carrying equivalent tasks as electric microwave filters, and they enjoy the advantages of low loss wide bandwidth operation and immunity to electromagnetic interference (EMI) [124]–[126]. A general configuration of MPFs is illustrated in Figure 6.1 (b). Compared with the electric microwave filters, it can be seen that the RF filtering circuit is replaced by an optical signal processer, and both electric (red line) and optical (blue line) links exist in the system. For MPFs, RF signal is first modulated on an optical carrier by the modulator, and after specific optical processing, the optical signals are converted back in the RF domain by the optical receiver, and the system response is mainly determined by the optical signal processer. Extensive researches have been devoted to microwave photonic (MWP) filtering using fiber optics with discrete components [127]–[129]. Various kinds of MWP filters have been proposed and demonstrated.

However, most of these MWP filters usually adopt multiple laser sources with different wavelengths in order to realize multi-tap filters. This results in extremely high cost. Furthermore, the whole system is quite bulky since a great number of discrete components are incorporated in order to build a filtering system.

Silicon photonics as one of the emerging technology has been attracting a lot of research interest due to the mature fabrication process, easy integration with microelectronics, etc. It is therefore possible to integrate such components for highly reconfigurable high-order MWP filters with compact footprint and significantly reduced cost. Several groups have demonstrated MWP filters using silicon photonics [130]–[132]. However, due to the relative high optical loss of the silicon waveguide and the serial cascading system, the maximum demonstrated MWP filter is only 4-tap [133], [134], thus significantly limiting the filtering performance.

In order to solve this problem and enhance the filtering performance, we aim to develop a multi-tap microwave photonic FIR filter with re-configurability using silicon integrated photonics. We propose a novel finite impulse response filter system using hybrid optical and silicon waveguide delay lines. We adopt cascaded two-stage N x M taps FIR filter, which provides flexibility by using different time delay schemes. We propose, for the first time, an integrated MWP FIR filter by using both optical fibers for low-loss long optical delay and on-chip silicon waveguides for short delay. The low loss property of the fiber sub-system and the high integration and compactness of the on-chip sub-system make it possible to realize high order MWP filters.

In the Chapter 3, 4 and 5, silicon photonic building blocks including optical delay lines, and input/output coupling system and power splitters have been developed.

Here, these components will be integrated with two sets of variable optical attenuators (VOA) and photodetectors to make the MWP FIR filter. Three rounds of fabrications have been done in this work. The performance of individual components is tested in the first two rounds, while the final round is dedicated to integrating all components into a filter. The VOA and each single PD design adopt the Institute of Micro Electronics (IME) typical design on 220 nm platform. Yet we set variations for the critical parameters in mask layout design and experimentally optimize their behaviors on a 300 nm platform based on measurement and result analysis. In this work, our proposed FIR filter only adopts positive branch coefficients. The design of traveling wave electrode PD array doesn't consider achieving the functionality of individually controllable phase for each PD, such as reversing the ground and signal electrodes to obtain negative voltage, to avoid design complexities. The major objective of this work is to verify the feasibility of the proposed hybrid design schema, to demonstrate high order (we demonstrate the filters of up to 16 taps) MWP FIR filter with spectrum re-configurablility and to establish the experience of system design, integration and calibration. This work is an essential basis for the high order FIR filter design with both positive and negative coefficients in the future development.

6.3 Brief discussion on the working principle of finite impulse response filter

The theoretical model of finite impulse response filters is shown in Figure 6.2. The input signal splits into several branches with the arithmetic series number of delay units; for each branch, a branch weight b_i is introduced, and the signals from each branch are finally summed as output. In order to calculate the system response, we

can set the input signal as unit impulse signal. Thus, the system response in time domain can be expressed as:

$$Y = \sum_{i=0}^{M-1} b_i \delta(t - iT) \tag{6.1}$$

Where b_i is each branch coefficient and $\delta(t)$ is unit impulse signal. Here, we consider that the first output impulse posits at zero point in time axis. If the profile of the coefficient b_i, which can be viewed as a discrete function of $b(iT)$ in time axis, is a cardinal sine function, then the corresponding frequency response is a filter response (or say, gate response). The value of time delay T is mainly determined by desirable filtering spectral response. Nyquist–Shannon sampling theorem is the principle to guide how to select the time delay[135]. If the maximum operating frequency of desired filter is B, then the of time delay T should be designed as $T \leq 1/(2B)$. Based on this consideration, the equation can be written as:

$$Y = \sum_{i=0}^{M-1} b(iT) \delta(t - iT) \tag{6.2}$$

Thus, we do the Fourier transform of the Eq.(6.2) above to obtain the system response in frequency domain. The corresponding Matlab code to calculate the system response is given in APPENDIX A. In this code, the delay T of each delay unit can be individually set. Since our system uses a combined delay of the off-chip fibers and on-chip silicon waveguides (this will be discussed in details in next section), to set the unit delay independently allows for flexible system calibration and convenient verification of the measurement results during experiment.

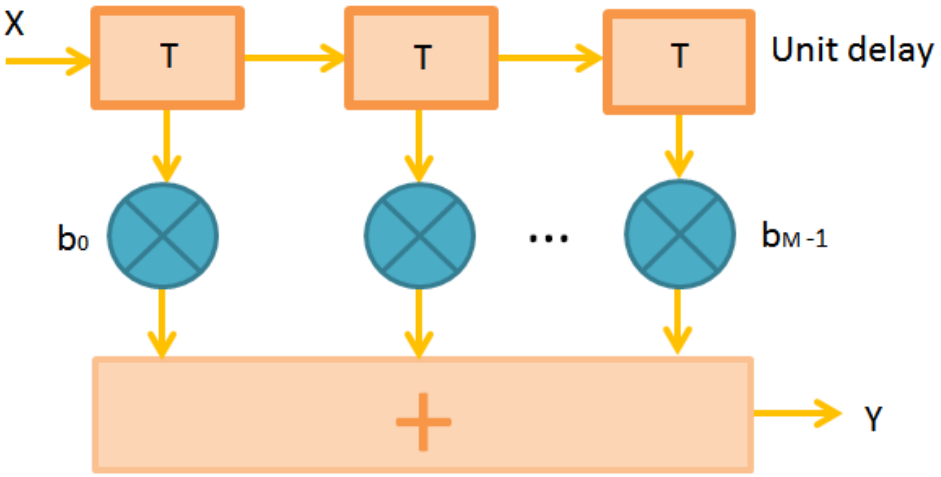

Figure 6.2 The theoretical model of a *M*-tap FIR filter

Based on the discussion above, several simulation results are given in the following group of figures for different tap number of FIR filters. In Figure 6.3, the S21 behavior of different tap FIR filters using hamming window with both positive and negative branch coefficients are illustrated for 4 tap, 8 tap, 16 tap and 64 tap FIR filters with 8 GHz passband. S21 is forward transmission coefficient which represents the received output power relative to the power input. It can be seen that using the design with more taps will provide better filtering effect i.e. better passband and filter attenuation. The filter attenuation for 64 tap configuration can achieve around 35 dB, but for fewer tap configurations, the filter attenuation will decrease accordingly. Thus, it is obvious that high order FIR filter designs bring better performance and is a more practical configuration for real world systems.

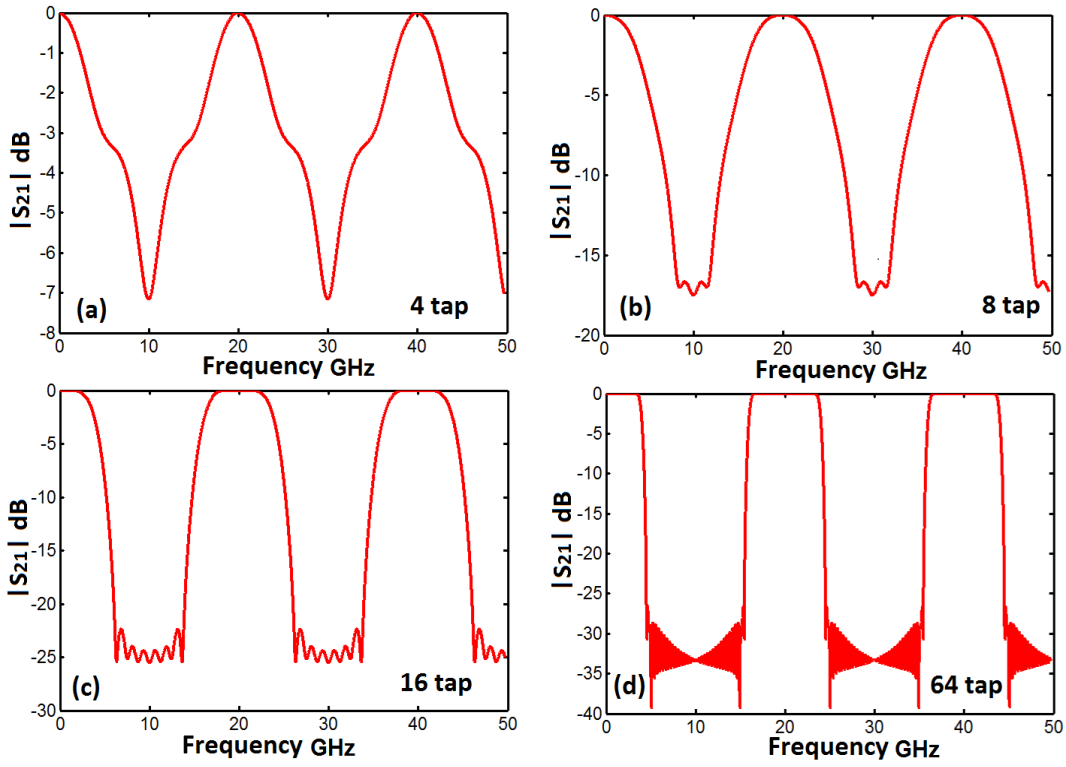

Figure 6.3 The S21 behavior of different tap FIR filters using hamming window with both positive and negative branch coefficients. (a) 4 tap; (b) 8 tap; (c) 16 tap; (d) 64 tap

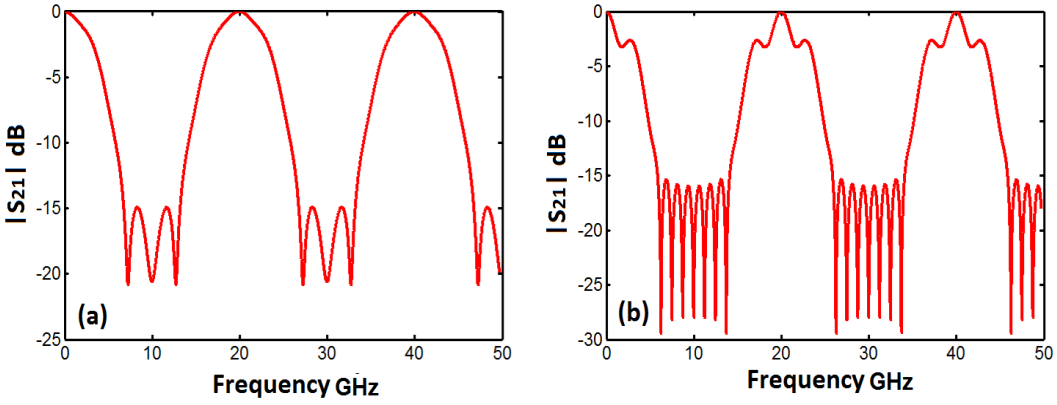

Figure 6.4 The S21 behavior of 16 tap FIR filters with only positive coefficients by (a) setting negative coefficient as 0 and (b) adding a constant to all the branch coefficients to achieve all positive coefficients

In order to intuitively illustrate the dependency of the filtering spectrum on the sign of branch coefficients, we take 16 tap filters with only positive coefficients as an example to simulate the S21 spectral response by setting negative coefficient as 0 and adding a constant to all the branch coefficients to achieve all positive coefficients. The simulation results are given in Figure 6.4. We can observe that the filtering effects get worse compared with Figure 6.3 (c). As in this project, our target is to prove that the design schema allows realizing high order filters, thus we only adopt all positive coefficient configuration. The filter design with both positive and negative coefficients would be a necessary extension in the future implementation for practical system. The brief idea for this part work is stated in Chapter 7.

6.4 An integrated schema of finite impulse response microwave photonic filter on silicon photonics platform

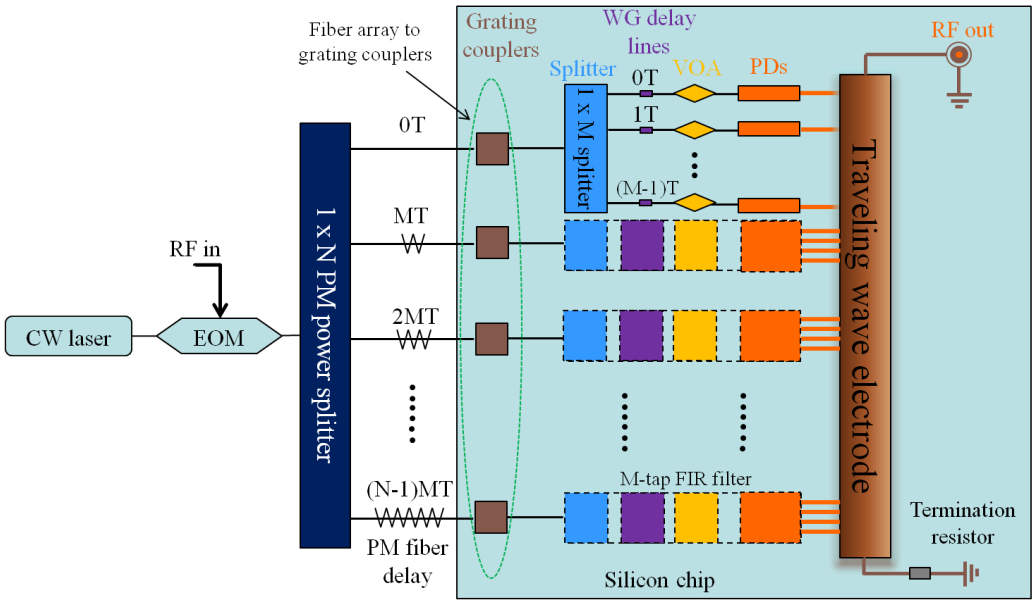

Figure 6.5 Proposed microwave FIR filter with ($N \times M$) taps using silicon CMOS photonics.

Figure 6.5 shows the implementation schematic with all the necessary building blocks. We combine both optical fibers for off-chip long delays and silicon waveguides for on-chip short delays in order to minimize the link optical loss. The laser source is modulated with the RF signal by an off-chip electro-optical (EO) transducer, also known as the Mach-Zehnder EO modulator. Its output is then split by an optical polarization-maintaining (PM) splitter into *N* channels and each individual channel is delayed via a fiber by a multiple of the FIR inter-tap delay, *T*. Each light channel is coupled into customized silicon photonics chip via fiber array coupling to on-chip grating couplers, followed by further power division into *M* channels and delayed by on-chip optical delay lines using silicon waveguides. The variable optical attenuators are used to adjust the amplitudes of the channel light. At the terminal end of all the sub-divided channels, the signals are detected by an integrated photodetector array (in total *N* x *M* PDs) and reconverted back to electrical signals. These electrical signals are finally summed up via a connecting traveling wave electrode.

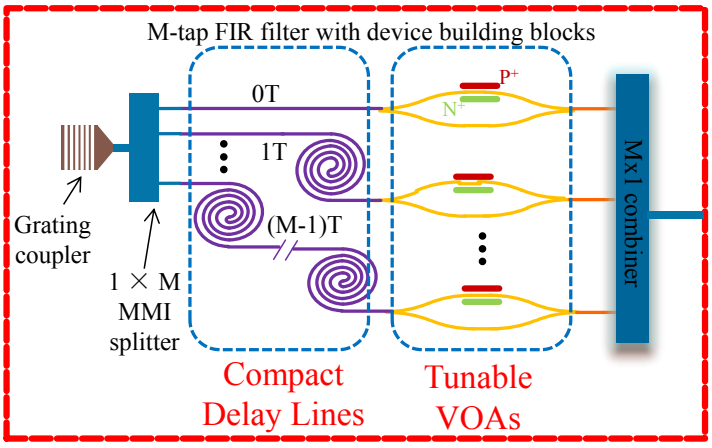

Figure 6.6 The schematics of an *M*-tap FIR filter with all the device building blocks in the silicon chip, including a grating coupler, 1 × *M* MMI splitter, waveguide delay lines, MZI EO VOAs, waveguide Ge PDs and a traveling wave electrode.

Figure 6.6 shows the subsystem FIR filter implementation scheme using silicon photonics. The light can be coupled into the silicon chip via grating coupler and divided into M channels by a $1 \times M$ splitter or cascaded 1×2 splitters. The light in each channel is then delayed by different optical delay lines using silicon waveguides, with an inter-tap delay of T. The amplitudes of the optical signals are adjusted by electro-optical tunable MZI VOAs and detected by photodetectors. The electrical signals are finally collected by a traveling wave electrode. In our practical implementation of the FIR filter, we set that M equals 4, and then for N fiber channels before the system on chip, we can make $4N$-taps FIR filter.

6.5 High efficient variable optical attenuator (VOA) and large bandwidth and high power handling traveling-wave photodetector array (TWPDA)

In this section, we introduce another two critical functional components, VOA and PD array, in the FIR filter system. The design of VOA and single PD are mainly based on the built-in component library of the Institute of Micro Electronics (IME), and are fabricated by the project collaborators at IME. We vary the dimension parameters and optimize the design experimentally in the first two rounds of fabrication and characterization during the project. In order to collect optical power from multi-channels, a novel design of travelling-wave photodetector array is proposed. We measure and characterize all the proposed components. The properties of these components will be discussed in detail in this section.

We first discuss the VOA design. Two different types of VOAs, i.e., the MZI-based and PIN-based structures, are proposed for the system. The light attenuation of the MZI-based VOA is based on the phase change induced destructive interference, while

the PIN-based VOA is based on the carrier injection effect induced loss. In general, PIN-based VOA is with the advantage of simple structure, low power consumption, and high attenuation ratio. Thus, we mainly focus on the PIN-based VOA. Figure 6.7 (a) and (b) show the design layouts. For PIN VOA, lateral PIN diode is adopted in order to inject the carriers into the waveguide region to induce optical loss for the intensity attenuation. For MZI VOA, a TiN heater is integrated for thermo-optical tunability in order to avoid additional loss. Figure 6.8 (a) and (b) show the measured optical response for PIN and MZI VOAs upon voltage supply, with different designed lengths. For PIN VOA, the intensity monotonously decreases as the increase of the supplied voltage. The longer the PIN diode length is, the higher efficiency of the intensity attenuation is. In contrast, the intensity response of the MZI VOA shows oscillation upon the supplied voltages due to the optical interference, and then it is not easy for practical operation. Thus, PIN diode VOA is suggested for the filter design. Furthermore, the PIN diode VOA shows much lower voltage, comparing to the MZI VOA, which results in low electrical power consumption. The electrical power consumptions for both PIN and MZI VOAs are shown in Figure 6.8 (c) and (d).

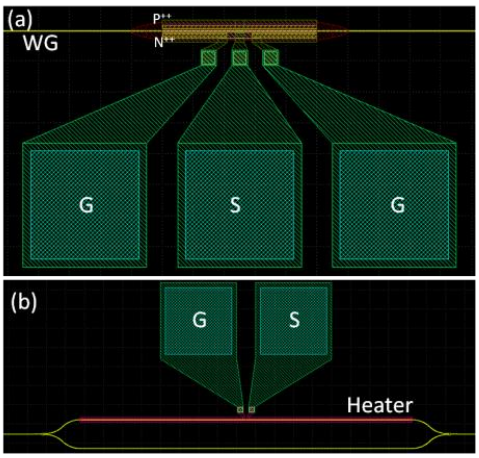

Figure 6.7 The design layouts of (a) the electro-optical tunable PIN-diode VOA, and (b) the thermo-optical tunable MZI VOA.

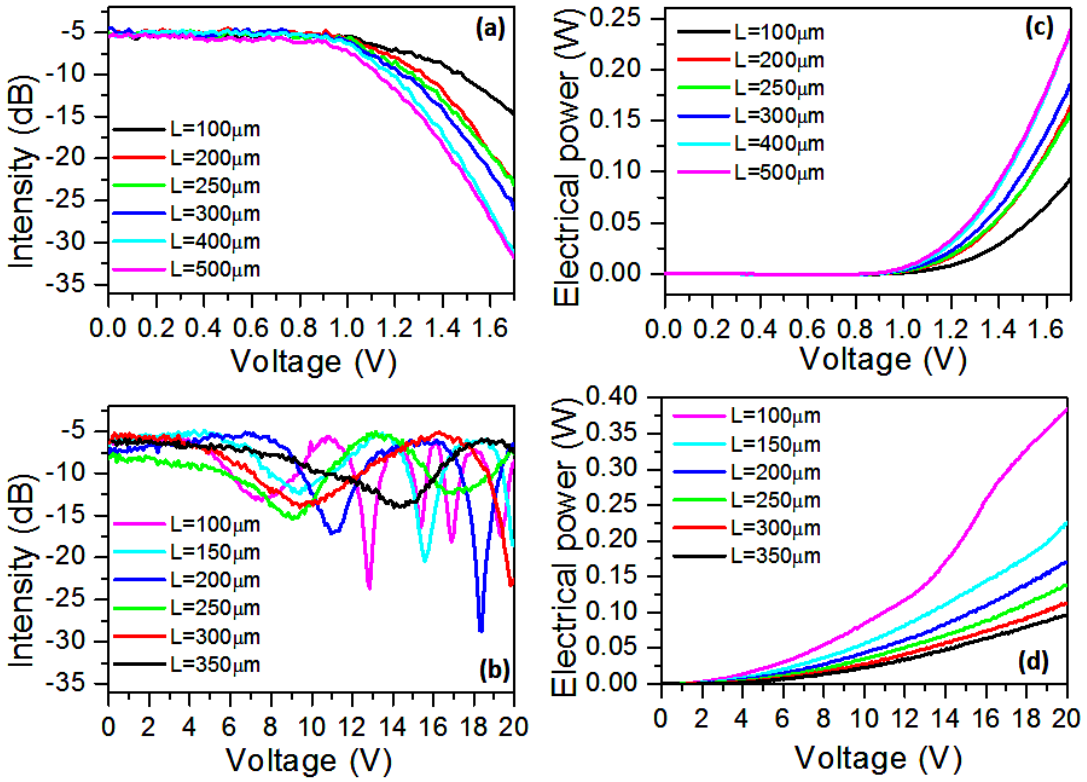

Figure 6.8 The measured optical responses upon voltage supplies for (a) the PIN VOA, and (b) the MZI VOA with different lengths. The measured electrical power consumption for (c) the PIN VOA, and (d) the MZI VOA with different lengths.

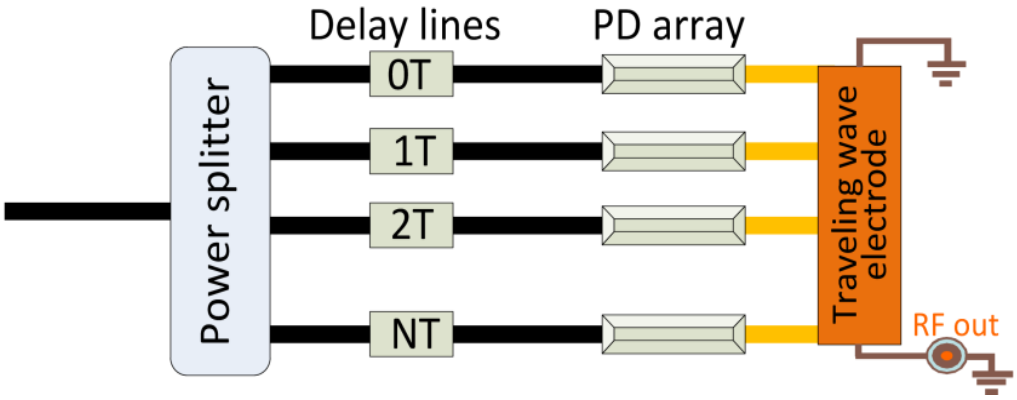

Figure 6.9 The block design of the parallel-fed travelling-wave photodetector array.

Then, we discuss the design of travelling-wave photodetector array (TWPDA)[136]. In this work, the first silicon-based parallel-fed travelling-wave photodetector array

has been demonstrated by our IME partner. The impedance-matched travelling-wave electrode is designed with considering the loading effect. The demonstrated up to 4-channel TWPDAs show more than 10GHz 3-dB bandwidths and responsivity of ~0.75A/W.

Figure 6.9 shows the block design of the parallel-fed TWPDA. The input light is first split into multiple parallel channels, e.g. *N* channels here, by using low-loss MMI splitter. The light in each of the channel is separately detected by individual high-speed photodetector. The photocurrent is then collected by using large bandwidth impedance-matched travelling-wave electrode in order to maintain the high-speed operation. Furthermore, the optical delay lines are adopted in each optical channel in order to balance the electrical phase delay.

We adopt high-speed Germanium (Ge) photodetectors for the light detection. In order for easy design and layout of the impedance-matched travelling-wave electrode, we adopt dual-metal layers, as shown in the zoom-in view of Figure 6.10. The bottom metal layer is the connection to individual Ge photodetector, while the top metal layer is the impedance-match travelling-wave electrode. We design the impedance-matched travelling-wave electrode with considering the periodic photodetector loading effect. For a symmetric GSG travelling-wave electrode design with 6 μm signal metal width and 4 μm gap separations, the calculated electrical phase velocity is ~ 7.5×107 m/s. The Ge photodetector is designed with 5 μm × 30 μm dimensions, and the periodicity is 25 μm. For all the travelling-wave electrode design, the ground metal widths are 100 μm. Thus, based on the calculated electrical phase velocity, we design the waveguide-based optical delay lines with unit delay of 0.3 ps, which corresponds to the waveguide length of around 25 μm, assuming the group index of around 4 for the silicon waveguide.

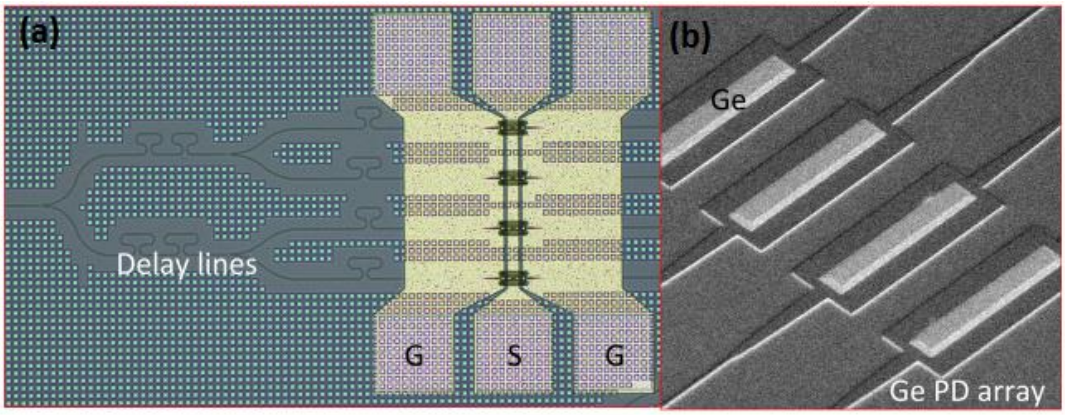

Figure 6.10 (a) Optical microscope of the fabricated 4-TWPDA. (b) The SEM of the Ge photodetector array right after the Ge growth.

Figure 6.10 (a) shows the optical microscope of a 4-TWPDA based on the design described previously. We design and fabricate 1-, 2-, and 4-TWPDAs in the same silicon chip with the identical designs. The waveguide width is 500 nm and the Ge PD is designed with dimension of 5 μm in width and 30 μm in length. The Ge PD periodicity is designed to be 25 μm, with the optical delay line difference between adjacent channels of 25 μm, in order for velocity matching between optical and electrical signals. Figure 6.10 (b) shows the SEM of the Ge photodetector array before the insulating oxide cladding and metallization.

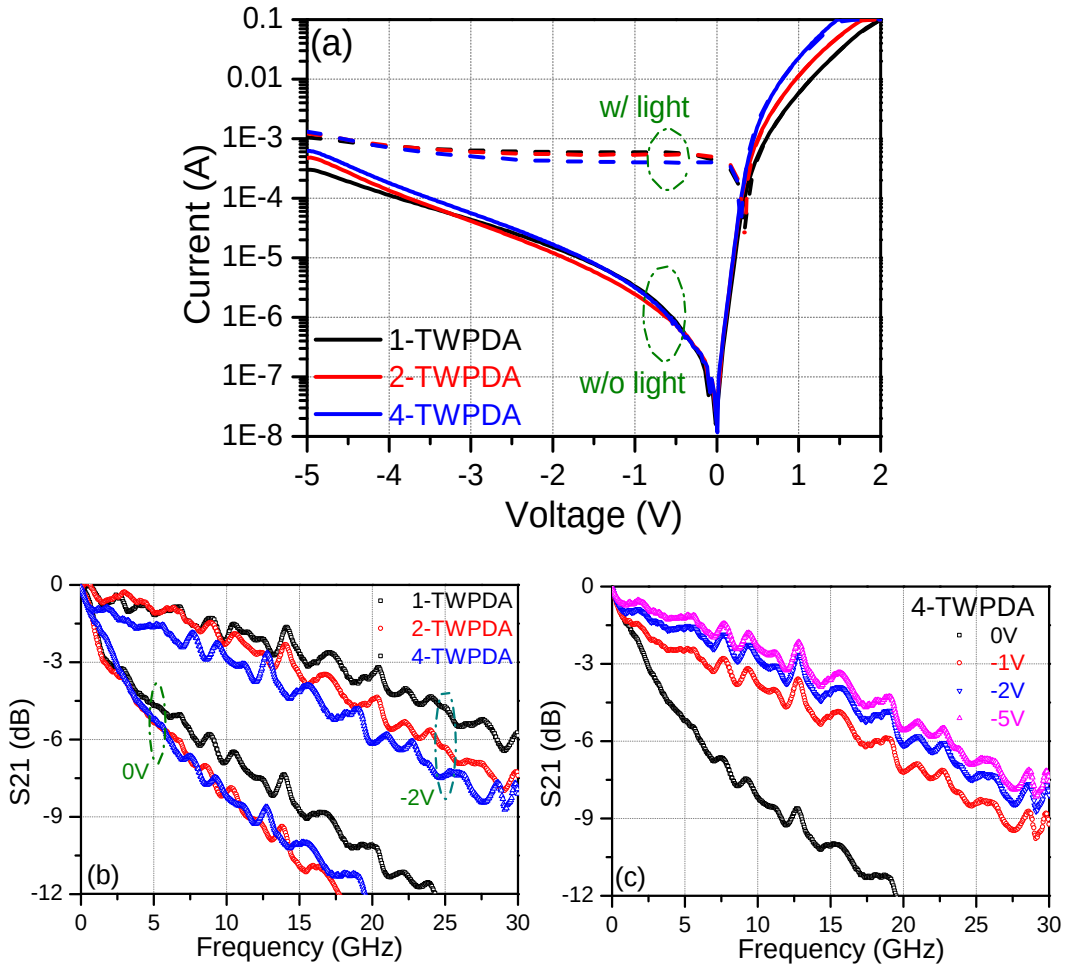

Figure 6.11 (a) Measured IV curves with and without light input; (b) Measured 3-dB bandwidth for 1-, 2-, and 4-TWPDA at 0 V and -2 V bias. (c) Measured 3-dB bandwidth for 4-TWPDA at different biased voltages.

We characterize the electrical performance of the TWPDAs by measuring the current-voltage response. Figure 6.11 (a) shows the measurement results with and without light input for 1-, 2-, and 4-TWPDAs. The dark current at -1 V bias is ~ 3 μA for all three types of TWPDAs. In contrast, with a laser output of 5 dBm at 1550 nm, the photocurrent at -1 V bias increases to ~ 0.55 mA. We mention that the optical insertion loss, including the system loss, the coupling loss, and the waveguide propagation loss, is ~ 6.8 dB before the light is absorbed by the photodetector. With varied input light intensity, we extract the responsivity of ~ 0.75 A/W.

We also measured the opto-electrical response of such TWPDAs by measuring the S21 parameter using a vector network analyzer (VNA). Figure 6.11 (b) shows the normalized S21 for 1-, 2-, and 4-TWPDA upon 0V and -2V bias voltages. In Figure 6.11, the 3-dB bandwidths at 0V are ~ 2.5 GHz. Upon -2V bias, the 3-dB bandwidth for 1-TWPDA is ~16 GHz, while decreasing to ~14 GHz and ~12 GHz for 2-, and 4-TWPDAs. An applied reverse bias voltage enlarges the space charge region and thus reduces the junction capacitance. That is why increase of the 3 dB bandwidth can be observed while reverse bias increases. The photodetector number increase will lead to increasing the lumped capacity arising from the parallel design, and thus causing decrease of 3dB bandwidth of TWPDAs. The RC effect limits the bandwidth performance.

In addition, Figure 6.11 (c) shows the normalized S21 for 4-TWPDA upon different voltage supplies. As the reverse biased voltage increases, the 3-dB bandwidth increases. The 3-dB bandwidth at -5V biased voltage is 13 GHz. However, the dark current at -5 V is as high as 0.5 mA (dark current is noise electric current that flows through PD when no photons are entering the device), which is not suitable for practical applications.

6.6 Demonstration of up to 16 tap microwave photonic filter and measurement discussion

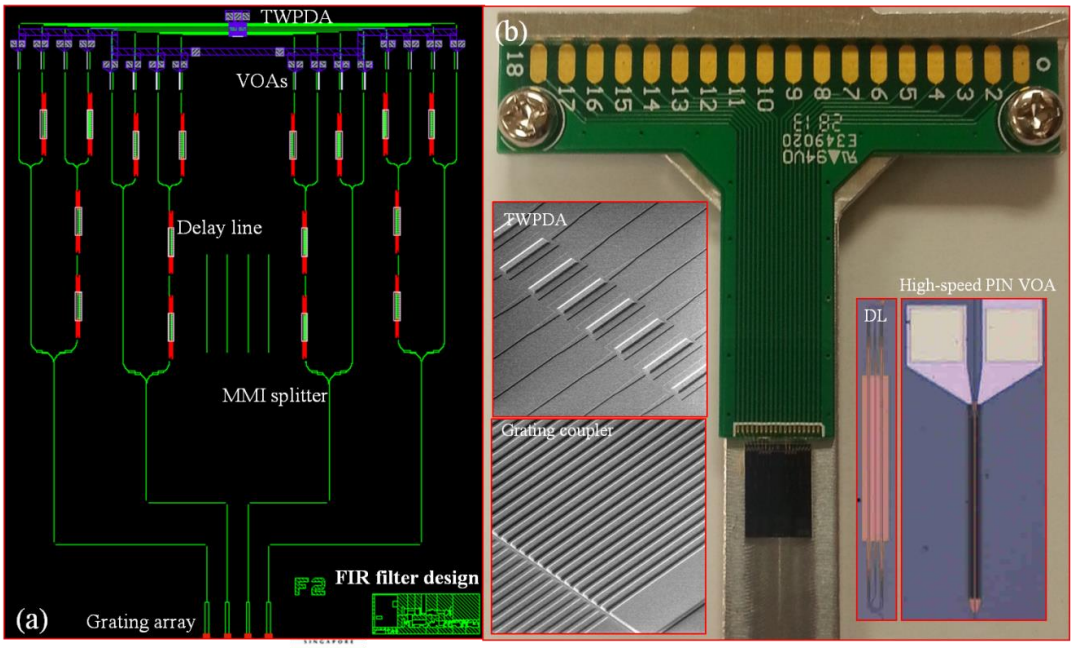

Figure 6.12 Design layout of a 16-tap microwave FIR filter, including grating coupler array, multiple delay lines, PIN VOAs, and the 8 channel TWPDA.

After introducing the individual components, we discuss the whole FIR filter implementation and the system measurement and characterization in this section. Figure 6.12 (a) shows the mask design of the proposed 16 tap FIR filter, and the fabricated filter sample is shown in Figure 6.12 (b). We can observe that the design layout of a 16-tap microwave FIR filter includes grating coupler array, multiple delay lines, PIN VOAs, and the 8 channel TWPDA. Here, the grating coupler stated in section 3.7, the delay line S2 presented in Chapter 4 and the MMI splitter discussed in Chapter 5 are used for the filter design. Based on the layout design, we have demonstrated 8 tap (i.e. only excite two grating couplers as inputs) and 16 tap FIR filters. The filter spectrum is reconfigurable with variation of the off-chip fiber delay

and the branch weight through tuning the supplied voltages on VOAs (all these operations change the filter system coefficient parameters). The effect includes shaping the spectral fringe profile, changing the dip frequency and depth.

The characterization setup is illustrated in Figure 6.13 (blue links are RF path and red links are optical path). The optical signal at 1.55 μm comes out from a CW laser and is modulated by a RF signal generated by a signal generator (In the schema, VNA is used to replace the signal generator and SSA to characterize the spectrum). Then, the signal is amplified by EDFA and enters into 1 by 4 fiber splitters, and the 4 channel signals experience arithmetic sequence delays for each branch and then go into a 4 channel fiber array. The output signals from fiber array are coupled into the chip components by grating array and detected by the PD array to form the RF signal which is collected by the RF probe and then measured by the SSA (or VNA).

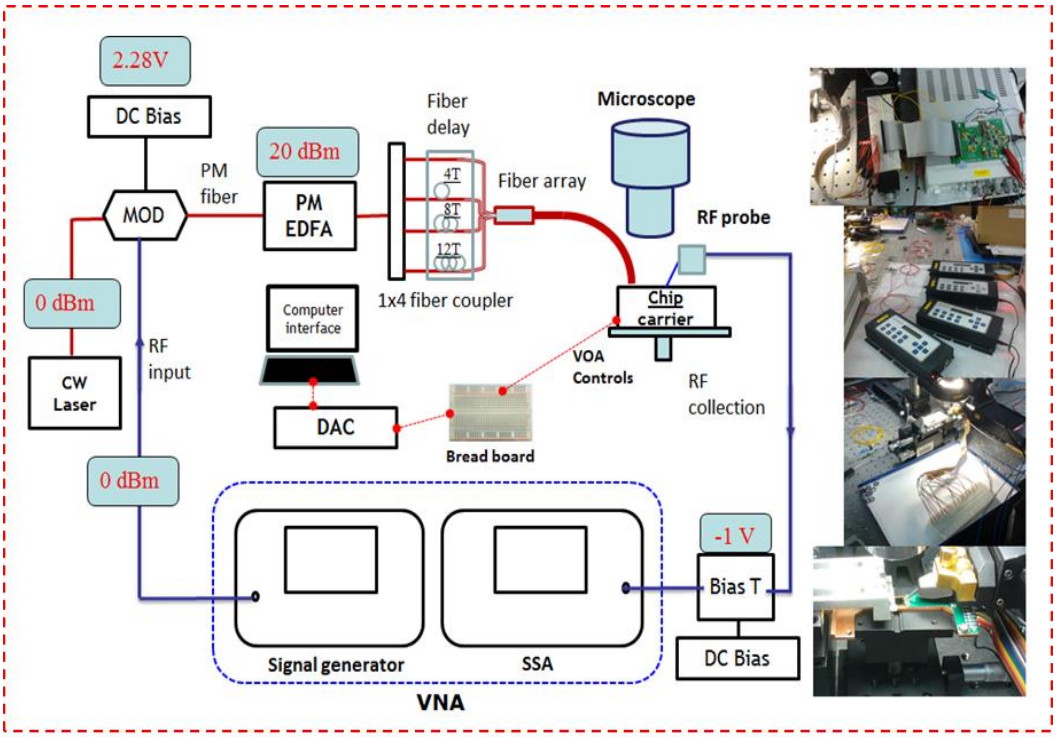

Figure 6.13 The characterization setup for the proposed FIR filter.

Figure 6.14 indicates the experimental spectrum achieved on 8-tap FIR filters along with the simulation results. For 8 tap FIR filter, we only excite two grating coupler inputs. While setting the off-chip fiber delay with large difference of around 4.8 ns for the two inputs, we can obtain the corresponding spectrum with dense fringes shown in Figure 6.14 (a). The result is reasonable as larger delay difference introduced for each branch will produce the spectral response with denser fringes. In order to calibrate the off-chip delay difference as 182 ps i.e. four times the on-chip delay (45.5 ps, here the whole waveguide delay rather than the delay only induced by the delay line units is considered), we first adjust the off-chip fiber delay to make the spectrum with only one dip at around 5 GHz, and the spectrum is the same as the one we give in Figure 4.18 of Chapter 4. When we obtain the single dip spectrum, it means that the off-chip fiber delay for the two inputs has the same value. Then, we further to increase one fiber branch delay by 182 ps to achieve the uniform delay (45.5 ps) for each tap on chip. This operation is very important for off-chip fiber delay calibration, and it is also used for 16 tap FIR filter measurement. By tuning the VOAs voltages, we can obtain bandpass filtering effect given in Figure 6.14 (b) and low pass filtering effect shown in Figure 6.14 (c). The theoretical simulation results are provided correspondingly. It can be seen that all the measurement results is matched with the corresponding theoretical results.

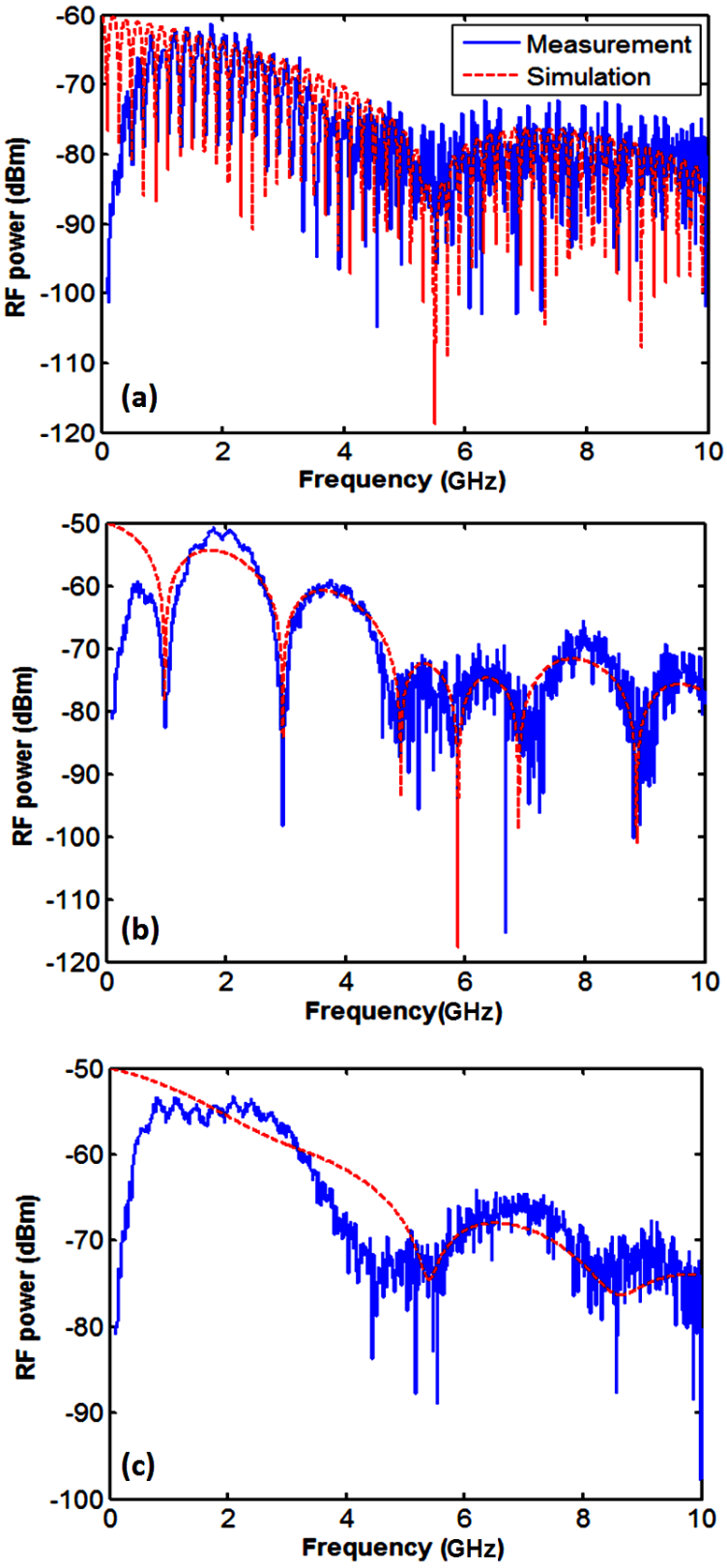

Figure 6.14 Reconfigurablility of the demonstrated 8-tap FIR filter upon variation of the tap weights through the intensity change using the VOAs.

For 16 tap filter demonstration, we excite all the four grating coupler inputs. For the measurement, we first calibrate the off-chip fiber delay as an arithmetic sequence with 182 ps difference between neighbor fibers using the aforementioned method, then, we applied the voltages on VOAs to tune the filter response. The low pass and band pass filtering effects are achieved for the 16 tap FIR filter, and the corresponding results are illustrated in Figure 6.15 (a) and (b), respectively. The simulation results are also shown in the figures.

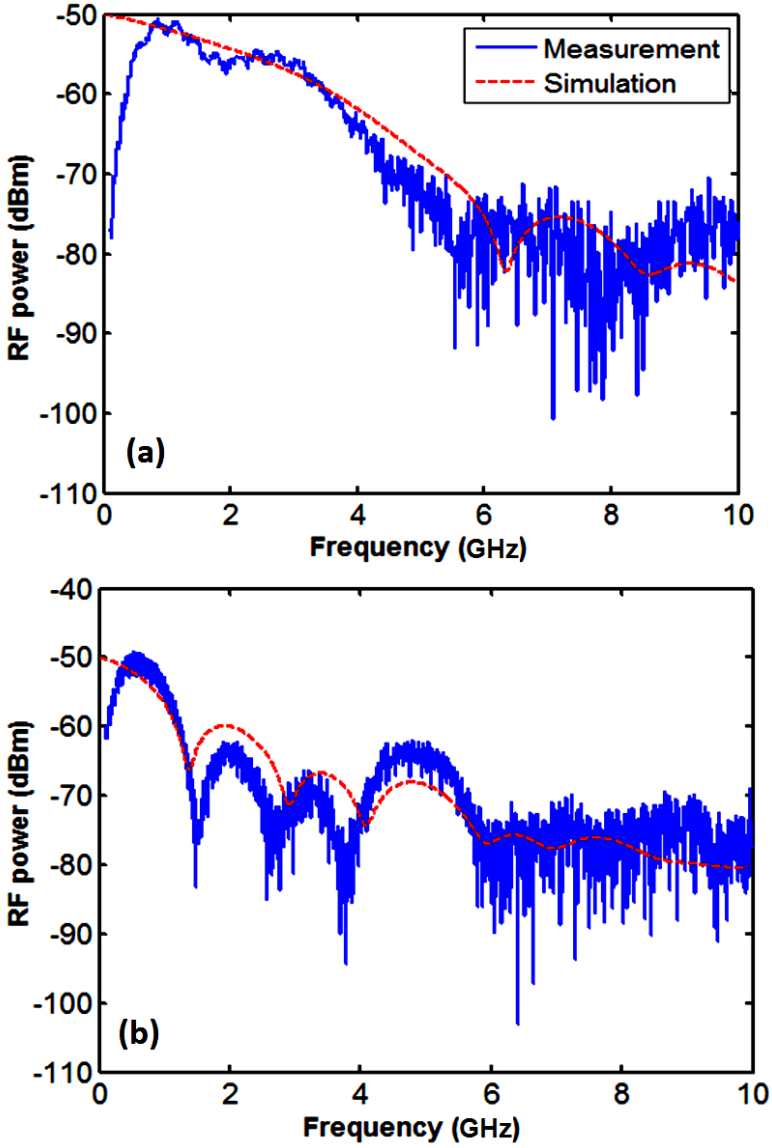

Figure 6.15 Low pass (a) and band pass (b) filtering of the demonstrated 16-tap FIR filter

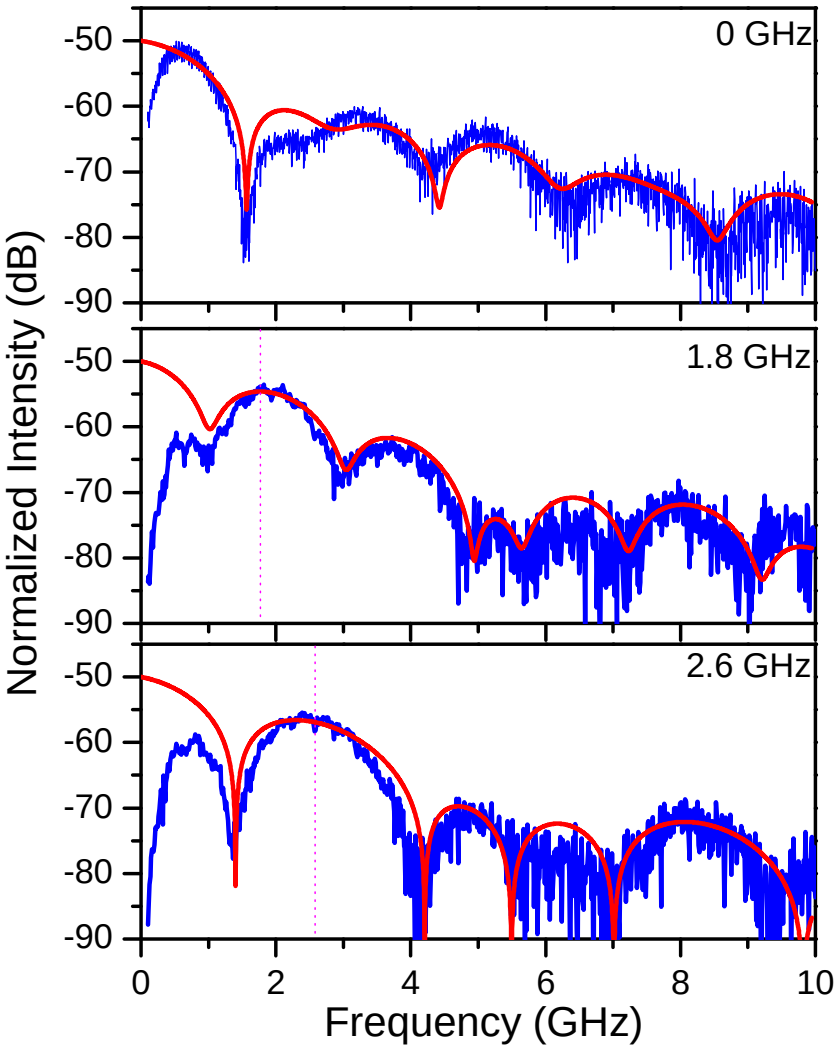

Figure 6.16 Re-configurability of the demonstrated 16-tap FIR filter upon variation of the tap weights through the intensity change using the VOAs.

More measurements are carried out for the 16 tap FIR filter by varying the voltage supplied in the VOAs to achieve the bandpass shifting effect, and a group of spectrum results are given in Figure 6.16. It can be seen that the pass band is at 0 GHz, 1.8 GHz and 2.6 GHz in these cases. The supplied voltage on each tap are given as follows: [1.43, 1.69, 1.65, 1.60, 1.60, 1.14, 1.30, 1.30, 1.65, 1.60, 1.43, 1.65, 1.65, 1.12, 1.43, 1.60] V, [1.20, 1.13, 1.32, 1.12, 1.59, 1.54, 1.47, 1.37, 1.12, 1.13, 1.31, 1.20, 1.00, 1.00, 1.00, 1.00] V, and [1.12, 1.13, 1.12, 1.12, 1.20, 1.40, 1.30, 1.20, 1.12, 1.13, 1.12, 1.12, 0.72, 0.60, 0.72, 0.70] V. The adjustment of VOA voltages is composed of several steps in practical operations. The first step is to characterize the

properties of VOA and obtain the relationship between power attenuation and the corresponding applied voltage. The second step is to plot voltage as a function of attenuation and fit it using a polynomial equation, which can be used to calculate the required voltages for desirable power attenuation in each branch in order to satisfy target branch weight distribution. Due to the fabrication variation of VOAs and loss contributed by the delay units, the voltage applied on each VOA should be further tuned individually to obtain the desirable spectrum. It should be noted that there is always a dip positioned at 0 GHz in all the measurement results, this is because the high frequency impedance matching is considered in our design of TWPDA, and then, when the PD bias voltage is supplied on all the parallel PDs, a constant direct current (DC) signal always exists. We ignore the DC factor in all our simulation results for the spectrum shape verification.

6.7 Summary

In summary of this chapter, we proposed a feasible design schema for high order FIR filter on silicon photonics platform. The FIR filter consists of grating coupler array, power splitters and several waveguide branches with different delay line units along with VOA and photodetector array. A 16 tap spectrum reconfigurable microwave FIR filter is demonstrated and the whole testing system and measurement results are discussed. The demonstrated filter only allows for positive branch coefficients, which theoretically limits the filtering performance. In order to achieve better filtering spectrum, it is necessary to implement both the positive and negative coefficients. The negative coefficients can be obtained by reversing the phase in the RF domain, or through adopting proper processing in both photonic and RF domain. With this improvement, the FIR filter can be deployed in practical signal processing system

Chapter 7 CONCLUSION AND FUTURE WORK

7.1 Achievements and Conclusion

In this thesis, we have discussed two main parts of our works. The first one is the general design and optimisation approaches of several critical passive components including grating coupler, delay line and power splitter, and the other is their system integration with other active components including VOA and photodetector to realize spectrum reconfigurable FIR filters.

In the first part of our work, we investigated the bandwidth mechanism of planar waveguide grating couplers on silicon photonics and the general bandwidth formula of planar waveguide grating couplers. Based on the bandwidth formula, we summarized the rules to optimize bandwidth of grating couplers. Besides this, the coupling efficiency optimisation process is also simplified by separating the parameter design by individual step to decrease the computation complexity. In addition, a 2-D grating coupler with double surface corrugation design is proposed to control the excitation wavelength for TE and TM mode at the same time, which can be used to achieve polarization insensitive or multi-channel coupling. We also propose a separate grating coupler design method to solve the low coupling efficiency problem of the silicon nitride waveguide based grating couplers. Then, for waveguide and delay line design, we discuss the general design rules for low loss delay line unit with accurate group delay using hybrid waveguide schema. 50 picoseconds low loss delay line on 300 nm SOI platforms is then experimentally demonstrated. The hybrid waveguide adopts wide multimode rib waveguide for straight section and semi-single mode waveguide for bend section. The straight rib waveguide achieve low propagation loss of about 0.1 dB/cm. For 50 ps delay unit, the loss performance is

0.7 dB/unit. For splitter study, we demonstrated the most compact MMI splitter in low loss performance with footprint of only 1.5×1.8 μm^2, which is about one order of magnitude smaller than previously reported MMI splitters. We presented the principle to determine the width of the multimode waveguide core which is usually ignored in previous design. Our designed splitter works polarization-independently and the excess losses for TE and TM modes at telecommunication wavelength are as low as 0.11 dB and 0.18 dB respectively. For the study of the spectrum reconfigurable FIR filters, we integrated the proposed grating coupler, delay line and power splitter with VOAs and photodetector array to achieve an integrated spectrum reconfigurable microwave photonic filter. We experimentally analyzed the behavior of the VOAs and photodetector array and demonstrated an integrated 16 tap FIR filter on silicon photonics platform, and theoretically discussed the filtering functionality and spectral reconfigurablility which is also verified by experimental measurement.

7.2 Future Work

Based on the studies described in this thesis, there could be many interesting extensions for the future work. We briefly discuss some of these directions in the following.

1. **Bandwidth investigation for apodized grating couplers and ultra-broadband high efficiency grating coupler design**

   In this thesis, we have derived the bandwidth formula for grating couplers with uniform pitch size. The derived formula cannot be directly applied to calculate the bandwidth of apodized grating couplers or the grating couplers with non-uniform period. The basic principles given in this thesis are still useful to analyze non-

uniform gratings which can be viewed as a great number of very short pieces of uniform gratings with different properties. In this case, the change of the grating property along the propagation direction can be expressed as the wavevector mismatch $\Delta\beta$ as a function of x. Following the same analysis given in Chapter 3, a more general formula can be obtained to cover the non-uniform cases. Another factor that can affect the bandwidth is the beam profile. In our derivation, Gaussian beam is adopted to model the incident beam from single mode fiber. Further study can be carried out to vary the beam patterns to increase the coupling bandwidth while maintaining high coupling efficiency.

2. **To achieve both positive and negative coefficients for spectrum tunable FIR filter design and building other higher levels of functionalities**

   For the FIR filter demonstrated in Chapter 6, all the branch coefficients only allow for positive values, which theoretically limit the performance of FIR filter. In order to achieve better filtering spectrum, it is necessary to implement both the positive and negative coefficients. The negative coefficients can be obtained by reversing the phase in the RF domain, or adopting proper processing in both photonic and RF domain. With this improvement, the FIR filter can be deployed in practical signal processing system. Moreover, based on the proposed photonic component design and integration practice in this thesis, it is achievable to build higher levels of functionalities such as photonic DAC/ADC.

APPENDIX A:

```
% For FIR filter design and experimental calibration
clear Omega;
clear all;
Omega = 0e12*5:20e6:0.0125e12*5; % angular frequency
%Omega=2*pi*sp(:,2)*1e9;
N = 16;         % number of taps
T1=ones(1,N)*55e-12;        % set the individual delays

T(1)=T1(1);
for i = 2:N
   T(i)= T1(i)+T(i-1);
end
Tm=T(N)/2;
Fc=0e9;        % Central frequency
%b1=(1+sin(2*pi*Fc.*(T-Tm)))/2;
b1=cos(2*pi*Fc.*(T-Tm));
ar = 0.54-0.46*cos(2*pi*(1:N)/(N-1));      % Hamming window
dF=2e9;         % filter bandwidth, HWHM
dF=dF*2*pi;
b=2*sin(dF.*(T-Tm))./(dF.*(T-Tm));       % sinc function
b(N/2)=2;
ar=ar.*(b1);
ar=ar.*(b);
X=Omega/2/pi/1e9;

HO = 0;
Lo=length(Omega);

for tn = 1:Lo
   HO(tn) =  sum(ar.*exp(-j*Omega(tn).*T));      % amplitude response
end
Theta=360/pi*atan(imag(HO)./real(HO));      % phase response
figure(1);
```

```
plot(X,10*log10(abs(HO))-max(10*log10(abs(HO))),'r');
hold on;
figure(2);
plot(X,Theta);
arnml=ar/(max(ar));
volt=1.69182-2.59041*arnml+5.09999*arnml.^2-4.707*arnml.^3+1.13247*arnml.^4
% through fitting the attenuation feature of VOA, we can obtain the equation to map the
attenuation to the required voltages supplied on VOAs
stem(T,ar) ;
```

PUBLICATIONS

Journal papers:

[1] **Zhe Xiao**, Feng Luan, Tsung-Yang Liow, Jing Zhang, and Ping Shum, "Design for broadband high-efficiency grating couplers," *Optics Letters*, 37, 530-532 (2012)

[2] **Zhe Xiao**, Tsung-Yang Liow，Jing Zhang, Silalahi, S.T.H., Ping Shum, and Feng Luan, "Mode control in planar waveguide grating couplers with double surface corrugation," *Photonics Technology Letters, IEEE,* vol.24, no.19, pp.1722-1725 (2012)

[3] **Zhe Xiao**, Tsung-Yang Liow, Jing Zhang, Ping Shum, and Feng Luan, "Bandwidth analysis of waveguide grating coupler," *Optics Express*, 21, 5688-5700 (2013)

[4] **Zhe Xiao**, Xianshu Luo, Peng Huei Lim, Patinharekandy Prabhathan, Samson T. H. Silalahi, Tsung-Yang Liow, Jing Zhang, and Feng Luan, "Ultra-compact low loss polarization insensitive silicon waveguide splitter," *Optics Express*, 21, 16331-16336 (2013)

[5] **Zhe Xiao**, Xianshu Luo, Tsung-Yang Liow, Peng Huei Lim, Patinharekandy Prabhathan, Jing Zhang, and Feng Luan, "Design and characterization of low loss 50 picoseconds delay line on SOI platform," *Optics Express*, 21, 21285-21292 (2013)

Conference papers:

[1] **Zhe Xiao**, Feng Luan and Jing Zhang, "Loss analysis of bent horizontal slot waveguides" in *International Conference on Nanophotonics*(*ICNP*), Shanghai, China, 2011

[2] **Zhe Xiao**, Feng Luan and Jing Zhang, "Light injection in horizontal slot waveguide using high-efficiency grating couplers," in *Asian Postgraduate Workshop on Nanoscience and Technology*, Hong Kong, China, 2011

[3] **Zhe Xiao**, Feng Luan, Jing Zhang, Tsung-Yang Liow, "Ultra-broadband high-efficiency grating couplers for light injection in horizontal slot waveguide," *Conference on Lasers and Electro-Optics Pacific Rim*, Sydney, Australia, 2011

[4] **Zhe Xiao**, Feng Luan, Tsung-Yang Liow, Jing Zhang, Shum Ping, "Vertical coupling for silicon nitride waveguides using silicon grating couplers and transitions," *IEEE Photonics Conference*(*IPC*) 2012, San Francisco, CA, USA.

[5] **Zhe Xiao**, Feng Luan, Xianshu Luo, Penghuei Lim, Samson T.H. Silalahi, Tsung-Yang Liow, Jing Zhang and Ping Shum "Highly compact ultra-low loss polarization insensitive 1-to-2 multimode interference splitter," *IEEE Photonics Conference*(*IPC*) 2012, San Francisco, CA, USA.

[6] **Zhe Xiao**, Feng Luan, Tsung-Yang Liow, Jing Zhang, Shum Ping, "Tolerant wideband high-efficiency grating coupler for TM mode excitation," *Photonics Global Conference* (*PGC*) 2012, Singapore

[7] **Zhe Xiao**, Xianshu Luo, Peng Huei Lim, Patinharekandy Prabhathan, Samson T.H. Silalahi, Tsung-Yang Liow, Jing Zhang and Feng Luan "Low loss delay line design and characterization on SOI platform," *Conference on Lasers and Electro-Optics Pacific Rim*, 2013

[8] Jing Zhang, Huijuan Zhang, Shiyi Chen, **Zhe Xiao**, Feng Luan, GQ Lo, "Mode converter between channel waveguide and slot waveguide," *Photonics Global Conference* (*PGC*), 2012, 1-4

REFERENCES

[1] "COMSOL Multiphysics." [Online]. Available: http://www.comsol.com/.

[2] "Lumerical FDTD Solutions." [Online]. Available: https://www.lumerical.com/tcad-products/fdtd/.

[3] "Lumerical Mode Solutions." [Online]. Available: https://www.lumerical.com/tcad-products/mode/.

[4] Z. Sheng, Z. Wang, C. Qiu, L. Li, A. Pang, A. Wu, X. Wang, S. Zou, and F. Gan, "A compact and low-loss MMI coupler fabricated with CMOS technology," *IEEE Photonics J.*, vol. 4, pp. 2272–2277, 2012.

[5] A. V. Rylyakov, C. L. Schow, B. G. Lee, W. M. J. Green, S. Assefa, F. E. Doany, M. Yang, J. Van Campenhout, C. V. Jahnes, J. A. Kash, and Y. A. Vlasov, "Silicon photonic switches hybrid-integrated with CMOS drivers," *IEEE J. Solid-State Circuits*, vol. 47, pp. 345–354, 2012.

[6] H. Park, M. N. Sysak, H. W. Chen, A. W. Fang, D. Liang, L. Liao, B. R. Koch, J. Bovington, Y. Tang, K. Wong, M. Jacob-Mitos, R. Jones, and J. E. Bowers, "Device and integration technology for silicon photonic transmitters," *IEEE J. Sel. Top. Quantum Electron.*, vol. 17, pp. 671–688, 2011.

[7] M. Hochberg and T. Baehr-Jones, "Towards fabless silicon photonics," *Nature Photonics*, vol. 4. pp. 492–494, 2010.

[8] P. K. Tien and R. Ulrich, "Theory of prism-film coupler and thin-film light guides," *Journal of the Optical Society of America*, vol. 60. p. 1325, 1970.

[9] R. Ulrich and R. Torge, "Measurement of thin film parameters with a prism coupler.," *Appl. Opt.*, vol. 12, pp. 2901–2908, 1973.

[10] M. Pu, L. Liu, H. Ou, K. Yvind, and J. M. Hvam, "Ultra-low-loss inverted taper coupler for silicon-on-insulator ridge waveguide," *Opt. Commun.*, vol. 283, pp. 3678–3682, 2010.

[11] M. Pu, L. Liu, H. Ou, K. Yvind, and J. M. Hvam, "Ultra-low-loss nano-taper coupler for silicon-on-insulator ridge waveguide," in *European Conference on Optical Communication, ECOC*, 2010, vol. 1–2.

[12] J. V. Galan, P. Sanchis, J. Blasco, and J. Marti, "Study of high efficiency grating couplers for silicon-based horizontal slot waveguides," *IEEE Photonics Technol. Lett.*, vol. 20, pp. 985–987, 2008.

[13] P. Cheben, P. J. Bock, J. H. Schmid, J. Lapointe, S. Janz, D.-X. Xu, A. Densmore, A. Del âge, B. Lamontagne, and T. J. Hall, "Refractive index engineering with subwavelength gratings for efficient microphotonic couplers and planar waveguide multiplexers.," *Opt. Lett.*, vol. 35, pp. 2526–2528, 2010.

[14] I. Day, I. Evans, A. Knights, F. Hopper, S. Roberts, J. Johnston, S. Day, J. Luff, H. Tsang, and M. Asghari, "Tapered silicon waveguides for low insertion loss highly-efficient high-speed electronic variable optical attenuators," *OFC 2003 Opt. Fiber Commun. Conf. 2003.*, 2003.

[15] J. K. Doylend and A. P. Knights, "Design and simulation of an integrated fiber-to-chip coupler for silicon-on-insulator waveguides," *IEEE J. Sel. Top. Quantum Electron.*, vol. 12, pp. 1363–1370, 2006.

[16] T. Shoji, T. Tsuchizawa, T. Watanabe, K. Yamada, and H. Morita, "Low loss mode size converter from 0.3 [micro sign]m square Si wire waveguides to singlemode fibres," *Electronics Letters*, vol. 38. p. 1669, 2002.

[17] G. Roelkens, P. Dumon, W. Bogaerts, D. van Thourhout, and R. Baets, "Efficient silicon-on-insulator fiber coupler fabricated using 248-nm-deep UV lithography," *IEEE Photonics Technol. Lett.*, vol. 17, pp. 2613–2615, 2005.

[18] A. Barkai, A. Liu, D. Kim, R. Cohen, N. Elek, H. H. Chang, B. H. Malik, R. Gabay, R. Jones, M. Paniccia, and N. Izhaky, "Double-stage taper for coupling between SOI waveguides and single-mode fiber," *J. Light. Technol.*, vol. 26, pp. 3860–3865, 2008.

[19] J. Cardenas, K. Luke, L. W. Luo, C. B. Poitras, P. a. Morton, and M. Lipson, "High Coupling Efficiency Etched Facet Tapers in Silicon," *Conf. Lasers Electro-Optics 2012*, p. JW4A.10, 2012.

[20] A. Mekis, S. Gloeckner, G. Masini, A. Narasimha, T. Pinguet, S. Sahni, and P. De Dobbelaere, "A grating-coupler-enabled CMOS photonics platform," *IEEE J. Sel. Top. Quantum Electron.*, vol. 17, pp. 597–608, 2011.

[21] L. Vivien, D. Pascal, S. Lardenois, D. Marris-Morini, E. Cassan, F. Grillot, S. Laval, J. M. Fédéli, and L. El Melhaoui, "Light injection in SOI microwaveguides using high-efficiency grating couplers," *J. Light. Technol.*, vol. 24, pp. 3810–3815, 2006.

[22] F. Van Laere, T. Claes, J. Schrauwen, S. Scheerlinck, W. Bogaerts, D. Taillaert, L. O'Faolain, D. Van Thourhout, and R. Baets, "Compact focusing grating couplers for silicon-on-insulator integrated circuits," *IEEE Photonics Technol. Lett.*, vol. 19, pp. 1919–1921, 2007.

[23] X. C. X. Chen, C. L. C. Li, and H. K. T. H. K. Tsang, "Fabrication-Tolerant Waveguide Chirped Grating Coupler for Coupling to a Perfectly Vertical Optical Fiber," *IEEE Photonics Technol. Lett.*, vol. 20, 2008.

[24] X. Xi, Z. Yu, X. Hai-Hua, Z. Liang, H. Ying-Tao, L. Zhi-Yong, L. Yun-Tao, Y. Yu-De, and Y. Jin-Zhong, "Wafer-Level Testable High-Speed Silicon Microring Modulator Integrated with Grating Couplers," *Chinese Physics Letters*, vol. 27. p. 094207, 2010.

[25] D. Vermeulen, S. Selvaraja, P. Verheyen, G. Lepage, W. Bogaerts, P. Absil, D. Van Thourhout, and G. Roelkens, "High-efficiency fiber-to-chip grating couplers realized using an advanced CMOS-compatible silicon-on-insulator platform.," *Opt. Express*, vol. 18, pp. 18278–18283, 2010.

[26] W. Bogaerts, S. K. Selvaraja, P. Dumon, J. Brouckaert, K. De Vos, D. Van Thourhout, and R. Baets, "Silicon-on-insulator spectral filters fabricated with CMOS technology," *IEEE J. Sel. Top. Quantum Electron.*, vol. 16, pp. 33–44, 2010.

[27] P. Dong, W. Qian, S. Liao, H. Liang, C.-C. Kung, N.-N. Feng, R. Shafiiha, J. Fong, D. Feng, A. V Krishnamoorthy, and M. Asghari, "Low loss shallow-ridge silicon waveguides.," *Opt. Express*, vol. 18, pp. 14474–14479, 2010.

[28] G. Li, J. Yao, H. Thacker, A. Mekis, X. Zheng, I. Shubin, Y. Luo, J. Lee, K. Raj, J. E. Cunningham, and A. V. Krishnamoorthy, "Ultralow-loss, high-density SOI optical waveguide routing for macrochip interconnects," *Optics Express*, vol. 20. p. 12035, 2012.

[29] J. Cardenas, C. B. Poitras, J. T. Robinson, K. Preston, L. Chen, and M. Lipson, "Low loss etchless silicon photonic waveguides.," *Opt. Express*, vol. 17, pp. 4752–4757, 2009.

[30] M. P. Nezhad, O. Bondarenko, M. Khajavikhan, A. Simic, and Y. Fainman, "Etch-free low loss silicon waveguides using hydrogen silsesquioxane oxidation masks," *Optics Express*, vol. 19. p. 18827, 2011.

[31] H. Lee, T. Chen, J. Li, O. Painter, and K. J. Vahala, "Ultra-low-loss optical delay line on a silicon chip," *Nature Communications*, vol. 3. p. 867, 2012.

[32] D. Taillaert, P. Bienstman, and R. Baets, “Compact efficient broadband grating coupler for silicon-on-insulator waveguides.,” *Opt. Lett.*, vol. 29, pp. 2749–2751, 2004.

[33] Q. Xu, V. R. Almeida, R. R. Panepucci, and M. Lipson, “Experimental demonstration of guiding and confining light in nanometer-size low-refractive-index material.,” *Opt. Lett.*, vol. 29, pp. 1626–1628, 2004.

[34] T. Baehr-Jones, M. Hochberg, C. Walker, and A. Scherer, “High-Q optical resonators in silicon-on-insulator-based slot waveguides,” *Appl. Phys. Lett.*, vol. 86, pp. 1–3, 2005.

[35] R. Sun, P. Dong, N. Feng, C. Hong, J. Michel, M. Lipson, and L. Kimerling, “Horizontal single and multiple slot waveguides: optical transmission at λ = 1550 nm,” *Optics Express*, vol. 15. p. 17967, 2007.

[36] C. Koos, P. Vorreau, T. Vallaitis, P. Dumon, W. Bogaerts, R. Baets, B. Esembeson, I. Biaggio, T. Michinobu, F. Diederich, W. Freude, and J. Leuthold, “All-optical high-speed signal processing with silicon – organic hybrid slot waveguides,” *Nat. Photonics*, vol. 3, pp. 1–4, 2009.

[37] R. Ding, T. Baehr-Jones, Y. Liu, R. Bojko, J. Witzens, S. Huang, J. Luo, S. Benight, P. Sullivan, J. M. Fedeli, M. Fournier, L. Dalton, A. Jen, and M. Hochberg, “A low V(pi)L modulator with GHz bandwidth based on an electro-optic polymer-clad silicon slot waveguide,” *IEEE Int. Conf. Gr. IV Photonics GFP*, vol. 18, no. 15, pp. 201–203, 2010.

[38] C. A. Barrios, K. B. Gylfason, B. Sánchez, A. Griol, H. Sohlström, M. Holgado, and R. Casquel, “Slot-waveguide biochemical sensor.,” *Opt. Lett.*, vol. 32, pp. 3080–3082, 2007.

[39] C. A. Barrios, “Optical slot-waveguide based biochemical sensors,” *Sensors (Switzerland)*, vol. 9. pp. 4751–4765, 2009.

[40] C. A. Barrios, “Ultrasensitive nanomechanical photonic sensor based on horizontal slot-waveguide resonator,” *IEEE Photonics Technol. Lett.*, vol. 18, pp. 2419–2421, 2006.

[41] S. H. Tao, Q. Fang, J. F. Song, M. B. Yu, G. Q. Lo, and D. L. Kwong, “Cascade wide-angle Y-junction 1 x 16 optical power splitter based on silicon wire waveguides on silicon-on-insulator.,” *Opt. Express*, vol. 16, pp. 21456–21461, 2008.

[42] K. K. Chung, H. P. Chan, and P. L. Chu, “A 1 × 4 polarization and wavelength independent optical power splitter based on a novel wide-angle low-loss Y-junction,” *Opt. Commun.*, vol. 267, pp. 367–372, 2006.

[43] A. Hosseini, H. Subbaraman, D. Kwong, Y. Zhang, and R. T. Chen, “Optimum access waveguide width for 1 x N multimode interference couplers on silicon nanomembrane.,” *Opt. Lett.*, vol. 35, pp. 2864–2866, 2010.

[44] D. J. Thomson, Y. Hu, G. T. Reed, and J. M. Fedeli, “Low loss MMI couplers for high performance MZI modulators,” *IEEE Photonics Technol. Lett.*, vol. 22, pp. 1485–1487, 2010.

[45] H. Guan, A. Novack, M. Streshinsky, R. Shi, Q. Fang, A. E.-J. Lim, G.-Q. Lo, T. Baehr-Jones, and M. Hochberg, “CMOS-compatible highly efficient polarization splitter and rotator based on a double-etched directional coupler,” *Opt. Express*, vol. 22, p. 2489, 2014.

[46] Y. Ding, L. Liu, C. Peucheret, and H. Ou, “Fabrication tolerant polarization splitter and rotator based on a tapered directional coupler,” *Optics Express*, vol. 20. p. 20021, 2012.

[47] D. Dai and J. E. Bowers, “Novel concept for ultracompact polarization splitter-rotator based on silicon nanowires.,” *Opt. Express*, vol. 19, pp. 10940–10949, 2011.
[48] D. Dai, Z. Wang, and J. E. Bowers, “Ultrashort broadband polarization beam splitter based on an asymmetrical directional coupler.,” *Opt. Lett.*, vol. 36, pp. 2590–2592, 2011.
[49] Y. F. Ma and D. W. Huang, “A compact slot waveguide directional coupler-based silicon-on-insulator polarization splitter,” in *2008 5th International Conference on Group IV Photonics, GFP*, 2008, pp. 297–298.
[50] D. Dai and J. E. Bowers, “Novel ultra-short and ultra-broadband polarization beam splitter based on a bent directional coupler,” *Optics Express*, vol. 19. p. 18614, 2011.
[51] Y. Fei, L. Zhang, T. Cao, Y. Cao, and S. Chen, “Ultracompact polarization splitter-rotator based on an asymmetric directional coupler.,” *Appl. Opt.*, vol. 51, pp. 8257–61, 2012.
[52] F. Xia, L. Sekaric, and Y. Vlasov, “Ultracompact optical buffers on a silicon chip,” *Nature Photonics*, vol. 1. pp. 65–71, 2007.
[53] S. Manipatruni, L. Chen, and M. Lipson, “Ultra high bandwidth WDM using silicon microring modulators.,” *Opt. Express*, vol. 18, pp. 16858–16867, 2010.
[54] A. Gondarenko, J. S. Levy, and M. Lipson, “High confinement micron-scale silicon nitride high Q ring resonator.,” *Opt. Express*, vol. 17, pp. 11366–11370, 2009.
[55] L. Zhang, Y. Li, J. Y. Yang, M. Song, R. G. Beausoleil, and A. E. Willner, “Silicon-based microring resonator modulators for intensity modulation,” *IEEE J. Sel. Top. Quantum Electron.*, vol. 16, pp. 149–158, 2010.
[56] S. Manipatruni, K. Preston, L. Chen, and M. Lipson, “Ultra-low voltage, ultra-small mode volume silicon microring modulator.,” *Opt. Express*, vol. 18, pp. 18235–18242, 2010.
[57] A. Nakhlestani and A. Hakimi, “Wideband microstrip ring resonator bandpass filter with embedded rings,” *Microelectronics J.*, vol. 44, pp. 462–467, 2013.
[58] S. Sun and L. Zhu, “Wideband microstrip ring resonator bandpass filter with asymmetrically-loaded stubs,” in *Proceedings of 2008 Asia Pacific Microwave Conference, APMC 2008*, 2008.
[59] N. A. Yebo, D. Taillaert, J. Roels, D. Lahem, M. Debliquy, D. Van Thourhout, and R. Baets, “Silicon-on-insulator (SOI) ring resonator-based integrated optical hydrogen sensor,” *IEEE Photonics Technol. Lett.*, vol. 21, pp. 960–962, 2009.
[60] N. A. Yebo, W. Bogaerts, Z. Hens, and R. Baets, “On-chip arrayed waveguide grating interrogated silicon-on-insulator microring resonator-based gas sensor,” *IEEE Photonics Technol. Lett.*, vol. 23, pp. 1505–1507, 2011.
[61] W. Bogaerts, P. De Heyn, T. Van Vaerenbergh, K. De Vos, S. Kumar Selvaraja, T. Claes, P. Dumon, P. Bienstman, D. Van Thourhout, and R. Baets, “Silicon microring resonators,” *Laser Photonics Rev.*, vol. 6, pp. 47–73, 2012.
[62] S. Darmawan, Y. M. Landobasa, P. Dumon, R. Baets, and M. K. Chin, “Nested-ring Mach-Zehnder interferometer in silicon-on-insulator,” *IEEE Photonics Technol. Lett.*, vol. 20, pp. 9–11, 2008.
[63] S. Akiyama, T. Kurahashi, T. Baba, N. Hatori, T. Usuki, and T. Yamamoto, “Slow-light silicon Mach-Zehnder modulator based-on cascaded ring resonators,” *Lasers Electro-Optics Quantum Electron. Laser Sci. Conf. (QELS), 2010 Conf.*, 2010.

[64] W. Bogaerts, P. Dumon, D. Van Thourhout, D. Taillaert, P. Jaenen, J. Wouters, S. Beckx, V. Wiaux, and R. G. Baets, "Compact wavelength-selective functions in silicon-on-insulator photonic wires," *IEEE J. Sel. Top. Quantum Electron.*, vol. 12, pp. 1394–1401, 2006.

[65] Q. Fang, T.-Y. Liow, J. F. Song, K. W. Ang, M. Bin Yu, G. Q. Lo, and D.-L. Kwong, "WDM multi-channel silicon photonic receiver with 320 Gbps data transmission capability.," *Opt. Express*, vol. 18, pp. 5106–5113, 2010.

[66] X. Chen, C. Li, C. K. Y. Fung, S. M. G. Lo, and H. K. Tsang, "Apodized waveguide grating couplers for efficient coupling to optical fibers," *IEEE Photonics Technol. Lett.*, vol. 22, pp. 1156–1158, 2010.

[67] M. Antelius, K. B. Gylfason, and H. Sohlström, "An apodized SOI waveguide-to-fiber surface grating coupler for single lithography silicon photonics.," *Opt. Express*, vol. 19, pp. 3592–3598, 2011.

[68] C. Li, H. Zhang, M. Yu, and G. Q. Lo, "CMOS-compatible high efficiency double-etched apodized waveguide grating coupler.," *Opt. Express*, vol. 21, pp. 7868–74, 2013.

[69] T. K. Gaylord and M. G. Moharam, "Analysis and applications of optical diffraction by gratings," *Proceedings of the IEEE*, vol. 73. pp. 894–937, 1985.

[70] G. Roelkens, D. Van Thourhout, and R. Baets, "High efficiency Silicon-on-Insulator grating coupler based on a poly-Silicon overlay.," *Opt. Express*, vol. 14, pp. 11622–11630, 2006.

[71] S. Miyanaga and T. Asakura, "Intensity profile of outgoing beams from uniform and linearly tapered grating couplers.," *Appl. Opt.*, vol. 20, pp. 688–695, 1981.

[72] F. Van Laere, G. Roelkens, M. Ayre, J. Schrauwen, D. Taillaert, D. Van Thourhout, T. F. Krauss, and R. Baets, "Compact and highly efficient grating couplers between optical fiber and nanophotonic waveguides," in *Journal of Lightwave Technology*, 2007, vol. 25, pp. 151–156.

[73] I. A. Avrutsky, A. S. Svakhin, V. A. Sychugov, and O. Parriaux, "High-efficiency single-order waveguide grating coupler.," *Opt. Lett.*, vol. 15, pp. 1446–1448, 1990.

[74] C. R. Doerr, L. Chen, Y.-K. Chen, and L. L. Buhl, "Wide Bandwidth Silicon Nitride Grating Coupler," *IEEE Photonics Technology Letters*, vol. 22. pp. 1461–1463, 2010.

[75] X. Chen, K. Xu, Z. Cheng, C. K. Y. Fung, and H. K. Tsang, "Wideband subwavelength gratings for coupling between silicon-on-insulator waveguides and optical fibers," *Optics Letters*, vol. 37. p. 3483, 2012.

[76] Z. Xiao, T.-Y. Liow, J. Zhang, P. Shum, and F. Luan, "Bandwidth analysis of waveguide grating coupler.," *Opt. Express*, vol. 21, no. 5, pp. 5688–700, 2013.

[77] Z. Xiao, F. Luan, T.-Y. Liow, J. Zhang, and P. Shum, "Design for broadband high-efficiency grating couplers," *Opt. Lett.*, vol. 37, no. 4, p. 530, 2012.

[78] T. Tamir and S. T. Peng, "Analysis and design of grating couplers," *Appl. Phys.*, vol. 14, pp. 235–254, 1977.

[79] a R. Zakharian, S. a Kuchinsky, X. Liu, and A. Kobyakov, "Grating-based Fiber-to-chip Coupling Efficiency for Small Mode Field Diameter Fibers," 2013, pp. 8–10.

[80] Z. Cheng and H. K. Tsang, "Experimental demonstration of polarization-insensitive air-cladding grating couplers for silicon-on-insulator waveguides.," *Opt. Lett.*, vol. 39, no. 7, pp. 2206–9, Apr. 2014.

[81] Z. Cheng, Z. Li, K. Xu, and H. K. Tsang, “Increase of the grating coupler bandwidth with a graphene overlay,” *Appl. Phys. Lett.*, vol. 104, no. 11, p. 111109, Mar. 2014.
[82] G. Roelkens, D. Van Thourhout, and R. Baets, “Silicon-on-insulator ultra-compact duplexer based on a diffractive grating structure.,” *Opt. Express*, vol. 15, pp. 10091–10096, 2007.
[83] D. Taillaert, H. Chong, P. I. Borel, L. H. Frandsen, R. M. De La Rue, and R. Baets, “A compact two-dimensional grating coupler used as a polarization splitter,” *IEEE Photonics Technol. Lett.*, vol. 15, pp. 1249–1251, 2003.
[84] R. Takei, K. Uchiho, and T. Mizumoto, “Polarization insensitive grating coupler for lightwave coupling between silicon nanophotonic waveguide and surface mounted photodetector,” *CLEO 2011 - Laser Sci. to Photonic Appl.*, pp. 1–2, 2011.
[85] M. Z. Alam, J. S. Aitchison, and M. Mojahedi, “Polarization-independent hybrid plasmonic coupler for a silicon on insulator platform,” *Optics Letters*, vol. 37. p. 3417, 2012.
[86] X. Chen and H. K. Tsang, “Polarization-independent grating couplers for silicon-on-insulator nanophotonic waveguides.,” *Opt. Lett.*, vol. 36, pp. 796–798, 2011.
[87] S. Shao and Y. Wang, “Highly compact polarization-independent grating coupler.,” *Opt. Lett.*, vol. 35, pp. 1834–1836, 2010.
[88] P. Markov, J. G. Valentine, and S. M. Weiss, “Fiber-to-chip coupler designed using an optical transformation,” *Optics Express*, vol. 20. p. 14705, 2012.
[89] Z. Xiao, T. Y. Liow, J. Zhang, S. T. H. Silalahi, P. Shum, and F. Luan, “Mode control in planar waveguide grating couplers with double surface corrugation,” *IEEE Photonics Technol. Lett.*, vol. 24, no. 19, pp. 1722–1725, 2012.
[90] S. M. Rytov, “Electromagnetic properties of a finely stratified medium,” *Sov. Phys. JETP*, vol. 2, pp. 466–475, 1956.
[91] P. Haguenauer, J. P. Berger, K. Rousselet-Perraut, P. Kern, F. Malbet, I. Schanen-Duport, and P. Benech, “Integrated Optics Theory and Technology,” *Appl. Opt.*, vol. 39, pp. 2130–9, 2000.
[92] J. C. Brazas and L. Li, “Analysis of input-grating couplers having finite lengths.,” *Appl. Opt.*, vol. 34, pp. 3786–3792, 1995.
[93] D. Taillaert, F. Van Laere, M. Ayre, W. Bogaerts, D. Van Thourhout, P. Bienstman, and R. Baets, “Grating Couplers for Coupling between Optical Fibers and Nanophotonic Waveguides,” *Japanese Journal of Applied Physics*, vol. 45. pp. 6071–6077, 2006.
[94] S. T. Peng, T. Tamir, and H. L. Bertoni, “Theory of Periodic Dielect Waveguides,” *IEEE Trans. Microw. Theory Tech.*, vol. 23, 1975.
[95] V. R. Almeida, Q. Xu, C. A. Barrios, and M. Lipson, “Guiding and confining light in void nanostructure.,” *Opt. Lett.*, vol. 29, pp. 1209–1211, 2004.
[96] A. Alphones, “Double grating coupler on a grounded dielectric slab waveguide,” *Opt. Commun.*, vol. 92, pp. 35–39, 1992.
[97] J. C. Brazas, L. Li, and A. L. McKeon, “High-efficiency input coupling into optical waveguides using gratings with double-surface corrugation.,” *Appl. Opt.*, vol. 34, pp. 604–609, 1995.
[98] G. Maire, L. Vivien, G. Sattler, A. Kazmierczak, B. Sanchez, K. B. Gylfason, A. Griol, D. Marris-Morini, E. Cassan, D. Giannone, H. Sohlström, and D. Hill, “High efficiency silicon nitride surface grating couplers.,” *Opt. Express*, vol. 16, pp. 328–333, 2008.

[99] V. Bhatt and S. Chandra, “Silicon nitride films deposited by RF sputtering for microstructure fabrication in MEMS,” *J. Electron. Mater.*, vol. 38, pp. 1979–1989, 2009.
[100] Y. Zuta, I. Goykhman, B. Desiatov, and U. Levy, “On-chip switching of a silicon nitride micro-ring resonator based on digital microfluidics platform.,” *Opt. Express*, vol. 18, pp. 24762–24769, 2010.
[101] M. K. Emsley, O. Dosunmu, and M. S. Unlu, “Silicon substrates with buried distributed Bragg reflectors for resonant cavity-enhanced optoelectronics,” *IEEE J. Sel. Top. Quantum Electron.*, vol. 8, pp. 948–955, 2002.
[102] G. Roelkens, D. Vermeulen, D. Van Thourhout, R. Baets, S. Brision, P. Lyan, P. Gautier, and J. M. Fédéli, “High efficiency diffractive grating couplers for interfacing a single mode optical fiber with a nanophotonic silicon-on-insulator waveguide circuit,” *Appl. Phys. Lett.*, vol. 92, 2008.
[103] T. Tekin, H. Schröder, L. Zimmermann, P. Dumon, and W. Bogaerts, “Fibre-Array Optical Interconnection for Silicon Photonics,” vol. 5, no. September, pp. 93–94, 2008.
[104] R. Kumar, K. Huybrechts, L. Liu, T. Spuessens, G. Roelkens, E.-J. Geluk, T. de Vries, P. Regreny, D. Van Thourhout, R. Baets, and G. Morthier, “An ultra-small, low-power all-optical flip-flop memory on a silicon chip,” *Opt. Fiber Commun. (OFC), collocated Natl. Fiber Opt. Eng. Conf. 2010 Conf.*, 2010.
[105] K. Voigt, L. Zimmermann, G. Winzer, T. Mitze, J. Bruns, K. Petermann, and C. Schubert, “SOI Delay Interferometer with Tuned Polarization Dependent Wavelength Shift for 40 Gbit/s DPSK Demodulation,” *2007 4th IEEE Int. Conf. Gr. IV Photonics*, 2007.
[106] Y. Okawachi, M. Foster, J. Sharping, A. Gaeta, Q. Xu, and M. Lipson, “All-optical slow-light on a photonic chip.,” *Opt. Express*, vol. 14, pp. 2317–2322, 2006.
[107] M. Povinelli, S. Johnson, and J. Joannopoulos, “Slow-light, band-edge waveguides for tunable time delays.,” *Opt. Express*, vol. 13, pp. 7145–7159, 2005.
[108] F. Morichetti, A. Melloni, C. Ferrari, and M. Martinelli, “Error-free continuously-tunable delay at 10 Gbit/s in a reconfigurable on-chip delay-line.,” *Opt. Express*, vol. 16, pp. 8395–8405, 2008.
[109] J. Cardenas, M. A. Foster, N. Sherwood-Droz, C. B. Poitras, H. L. R. Lira, B. Zhang, A. L. Gaeta, J. B. Khurgin, P. Morton, and M. Lipson, “Wide-bandwidth continuously tunable optical delay line using silicon microring resonators.,” *Opt. Express*, vol. 18, pp. 26525–26534, 2010.
[110] S. Spector, M. W. Geis, D. Lennon, R. C. Williamson, and T. M. Lyszczarz, “Hybrid multi-mode/single-mode waveguides for low loss,” in *Optical Amplifiers and Their Applications/Integrated Photonics Research*, 2004, p. IThE5.
[111] W. Bogaerts and S. K. Selvaraja, “Compact single-mode silicon hybrid rib/strip waveguide with adiabatic bends,” *IEEE Photonics J.*, vol. 3, pp. 422–432, 2011.
[112] X. Yi, F. Wei, Y. Wang, C. Lu, and W. De Zhong, “Group delay measurement of WDM components using photonic microwave technique,” *Microw. Opt. Technol. Lett.*, vol. 35, no. 5, pp. 346–348, Dec. 2002.
[113] Y. Zhang, S. Yang, A. E.-J. Lim, G.-Q. Lo, C. Galland, T. Baehr-Jones, and M. Hochberg, “A compact and low loss Y-junction for submicron silicon waveguide.,” *Opt. Express*, vol. 21, pp. 1310–6, 2013.

[114] H. Yamada, T. Chu, S. Ishida, and Y. Arakawa, "Optical directional coupler based on Si-wire waveguides," *IEEE Photonics Technol. Lett.*, vol. 17, pp. 585–587, 2005.
[115] P. P. Sahu, "Compact multimode interference coupler with tapered waveguide geometry," *Opt. Commun.*, vol. 277, pp. 295–301, 2007.
[116] E. C. M. Pennings, R. van Roijen, M. J. N. van Stralen, P. J. de Waard, R. G. M. P. Koumans, and B. H. Verbeek, "Reflection properties of multimode interference devices," *IEEE Photonics Technol. Lett.*, vol. 6, pp. 715–718, 1994.
[117] L. B. Soldano and E. C. M. Pennings, "Optical multi-mode interference devices based on self-imaging: principles and applications," *J. Light. Technol.*, vol. 13, pp. 615–627, 1995.
[118] D. Dai and S. He, "Optimization of ultracompact polarization-insensitive multimode interference couplers based on Si nanowire waveguides," *IEEE Photonics Technol. Lett.*, vol. 18, pp. 2017–2019, 2006.
[119] K. S. Chiang and Q. Liu, "Formulae for the design of polarization-insensitive multimode interference couplers," *IEEE Photonics Technol. Lett.*, vol. 23, pp. 1277–1279, 2011.
[120] G. Electronics and K. Iga, "Resolution of self-images in planar optical waveguides," vol. 68, no. 5, pp. 583–592, 1978.
[121] J. Lin, "Theoretical investigation of polarization-insensitive multimode interference splitters on silicon-on-insulator," *IEEE Photonics Technol. Lett.*, vol. 20, pp. 1234–1236, 2008.
[122] "IMEC Helios project." [Online]. Available: http://www.helios-project.eu/Partners/IMEC.
[123] I. C. Hunter, L. Billonet, B. Jarry, and P. Guillon, "Microwave filters-applications and technology," *IEEE Trans. Microw. Theory Tech.*, vol. 50, 2002.
[124] J. Capmany, B. Ortega, and D. Pastor, "A tutorial on microwave photonic filters," *J. Light. Technol.*, vol. 24, pp. 201–229, 2006.
[125] J. Capmany and D. Novak, "Microwave photonics combines two worlds," *Nature Photonics*, vol. 1. pp. 319–330, 2007.
[126] D. Novak and D. Guckenberger, "Microwave photonics," *IEEE MTT-S International Microwave Symposium Digest*, p. 1, 2006.
[127] J. Capmany, J. Mora, D. Pastor, and B. Ortega, "High-quality online-reconfigurable microwave photonic transversal filter with positive and negative coefficients," *IEEE Photonics Technol. Lett.*, vol. 17, pp. 2730–2732, 2005.
[128] Y. M. Chang, H. Chung, and J. H. Lee, "High Q microwave filter using incoherent, continuous-wave supercontinuum and dispersion-profiled fiber," *IEEE Photonics Technol. Lett.*, vol. 19, pp. 2042–2044, 2007.
[129] T. X. H. Huang, X. Y. X. Yi, and R. A. Minasian, "A high-order FIR microwave photonic filter," *2009 Int. Top. Meet. Microw. Photonics*, 2009.
[130] J. Sancho, J. Bourderionnet, J. Lloret, S. Combrié, I. Gasulla, S. Xavier, S. Sales, P. Colman, G. Lehoucq, D. Dolfi, J. Capmany, and A. De Rossi, "Integrable microwave filter based on a photonic crystal delay line," *Nature Communications*, vol. 3. p. 1075, 2012.
[131] H. W. Chen, A. W. Fang, J. D. Peters, Z. Wang, J. Bovington, D. Liang, and J. E. Bowers, "Integrated microwave photonic filter on a hybrid silicon platform," *IEEE Trans. Microw. Theory Tech.*, vol. 58, pp. 3213–3219, 2010.

[132] J. Dong, L. Liu, D. Gao, Y. Yu, A. Zheng, T. Yang, and X. Zhang, “Compact notch microwave photonic filters using on-chip integrated microring resonators,” *IEEE Photonics J.*, vol. 5, 2013.
[133] L. R. Chen, J. Li, M. Spasojevic, and R. Adams, “Nanowires and sidewall Bragg gratings in silicon as enabling technologies for microwave photonic filters.,” *Opt. Express*, vol. 21, pp. 19624–33, 2013.
[134] D. Marpaung and B. J. Eggleton, “Nonlinear integrated microwave photonics,” in *2013 IEEE International Topical Meeting on Microwave Photonics, MWP 2013*, 2013, pp. 84–87.
[135] A. J. Jerri, “Shannon sampling theorem - ITS various extensions and applications: a tutorial review,” *Proceedings of the IEEE*, vol. 65. pp. 1565–1596, 1977.
[136] X. Luo, J. Song, X. Tu, Q. Fang, L. Jia, Y. Huang, T.-Y. Liow, M. Yu, and G.-Q. Lo, “Silicon-based traveling-wave photodetector array (Si-TWPDA) with parallel optical feeding,” *Opt. Express*, vol. 22, no. 17, p. 20020, 2014.